Bioinspired Manufacturing: Photoinduced Self-Replication of Metal Nanoparticles in Solution and on Surfaces

by

Connor N. McGlothin

A dissertation submitted in partial fulfillment
of the requirements for the degree of
Doctor of Philosophy
(Chemical Engineering)
in the University of Michigan
2023

Doctoral Committee:

Professor Nicholas A. Kotov, Chair
Professor Julie S. Biteen
Professor Joerg Lahann
Professor Suljo Linic

Connor N. McGlothin

cmcgloth@umich.edu

ORCID iD: 0000-0002-3201-1586

Dedication

To my family and especially my grandfather, Nicholas Lesko, who without I would not be where I am today. May you rest in peace.

Acknowledgements

I would like to first thank my advisor, Professor Nicholas A. Kotov for taking me into his lab group, even though I knew nothing about nanomaterials, when my previous advisor left the university. Your endless support, compassion, and enthusiasm for everything made the good times seem great and the bad times seem good. It was a privilege working for someone who really cares about his students. I could not imagine having a different advisor.

I would also like to thank my dissertation committee, Professor Suljo Linic, Professor Joerg Lahann, Professor Julie Biteen for their time, but especially for their intellectual advice on my work. I am fortunate to have such a wide range of experts in various fields. Your questions at the critical points of my PhD made it what it is today.

I want to thank all the Kotov lab members, both past and present. Kody, Jessica, Elizabeth Ahmet, Sumeyra, Drew, Misché, Doug, Harrison, Alain, Jun Bumchul, SangHyun, Prashant, Michal, Wenbing, Yuan, Chung-Man, and many more. This group of people is one of the main reasons I looked forward to coming into lab the past 5 years, even at night with the night owls, you know who you are. I will never forget how much free food meant as well to this group. A special thanks to Elizabeth, Doug, and Harrison. Transitioning into this lab was at a crazy time, but you all made those early years some of the best.

It would not be right without thanking all the great friends that I made outside of lab in Ann Arbor: Sean, Zach, Alex, Jacques, Patrick, Danielle, Rachael, Emily, Misché, Harrison, Anna, Jordyn, Marshall, Tobias, and Katey. From Depot St. to Bill's, you have all made these past 5

years just incredible with your support and comradery. Also, living on Broadway will always be some of the best years of my life and I cherish those memories every day. I can't wait to see where our lives outside of graduate school take us. Additionally, I would like to thank Tyler, Joel, April, and Shelby who have been there seen undergrad for me, I am glad we have remained friends throughout these countless years. I can't list everyone, so to all my other friends out there, you know who you are, and you know how much I appreciate our chats and trips.

As many know I am an avid dog lover, so I would be crazy if I did not also thank all the four-legged furry friends that I had the pleasure to see and take care of: Leo, Frankie, Fitz, Relo, Phoebe, Rose, Bella, Dash, Colt, and Nala.

Most importantly, I want to thank my family for always being there for me. I would not be where I am today without you. Your push to have all of us kids get the highest education we could has made us the best we could be. Your encouragement and love helped me get through any obstacles that I faced throughout this program. I am truly grateful for your love and support.

Last, but not least, I want to give my greatest thanks to my best friend and other half, Zixuan, whose love, support, wisdom, and stubbornness got me through these last 5 years regardless of whatever was thrown at us. Words cannot fully express how grateful I am for you. I am excited for where life will take us and the adventures we will have.

Table of Contents

List of Figures

List of Appendices

Abstract

Self-replication and self-assembly are two processes essential for biological systems. Their ex-vivo reproduction continuously fuels fundamental scientific discoveries and can be essential for sustainable manufacturing. It currently remains unknown whether one can successfully couple these processes for engineered biomimetic systems, especially for robust inorganic components of technological significance. Here we seek to explore into the field of self-replication in search for an inorganic biomimetic system not seen to this date.

The first scope of this thesis was to find an inorganic colloidal system with preliminary characteristics of self-replication, using silver nanoparticles as the initial material. As a self-replicating inorganic particle system has never been realized before, there is minimal previous work base off of. As a result, a high-throughput screening method consisting of three steps was developed to comb through a high density of systems in **Chapter 3**. After over 100 systems, one condition passed the screening steps to be examined more in depth. This screening method will be useful for the discovery of future inorganic self-replicating materials outside of silver.

Silver nanoparticles synthesized from a solution of 0.1 mM silver nitrate and 3 mM citrate at a critical pH of 10.3 were found to simultaneously self-replicate and self-assemble in a process driven by light in **Chapter 4**. Careful selection of illumination, environmental, and media conditions resulted in the growth of the nanoparticles catalyzed by the previously formed ones. Ex-situ characterization methods were used to evaluate the nanoparticle concentration over time, where a sigmoidal curve indicative of autocatalysis and self-replication was confirmed. A series

of highly advanced electron microscopy techniques were used to probe in real time the nucleation and self-replication of the silver nanoparticles. It was discovered that the interface of the parent particle created favorable conditions for silver nuclei to form resulting in a chain-like assembly of self-replicated particles. This fundamental understanding of the formation of the nanoparticles was used to develop a computational model describing the kinetics to help support the experimental kinetic trends.

The second scope of this thesis was to expand this bioinspired system to various applications in **Chapter 5**. Realization of coupled self-assembly and self-replication in the vicinity of a substrate resulted in complex neuron-like networks of nanoparticles that allow their utilization for the preparation of conductive coatings for various applications. Furthermore, introducing the self-replicating particles to a highly corrugated surface, i.e. spikey hedgehog particles, the gap between the tips of the spikes can be bridged via radial replication of the silver nanoparticles away from the spike. These suspended nanoparticle bridges on highly corrugated surfaces could have numerous applications in microfluidics, photonic, and sensing.

Chirality was another pathway explored as the combination of the plasmonic effect coupled with chirality opens a wide range of applications in sensing, catalysis, and photonics. Illuminating a substrate submerged in a solution of silver precursor and citrate with circularly polarized light created complex chiral silver helicoids on the surface. These helicoids could be tuned on-the-fly to print chiral patterns on any substrate with chiroptical activity extending the entire visible spectrum. The knowledge obtained from this system was applied to the self-replicating system. In the end, it was found that introducing a second metallic salt, copper nitrate, can induce chirality at self-replicating conditions. Overall, this thesis establishes a foothold into inorganic self-replicating materials that have not been experimentally seen before.

Chapter 1 Introduction

1.1 Summary

This chapter entails the background and motivation for developing an inorganic self-replicating system. In **Section 1.1**, a general outline of what self-replication is and how it can be applied to both organic and inorganic systems will be discussed. The motivation behind developing this system for inorganic materials will be discussed here as well. As the material used throughout this thesis will be inorganic plasmonic nanoparticles, a brief background of on plasmonic particles and how they are commonly synthesized will be described in **Section 1.2**. Further details on chirality in plasmonic nanoparticles will be explored in this section. Finally, **Section 1.3** will provide an outline of the rest of the research goals in this thesis.

1.2 Self-Replication

Self-replication is a unique property found throughout all of nature. It is a key defining characteristic of living things, but it also has the capability of being present in inorganic systems as well. This section will provide background on self-replication as it is found in nature and synthetically (**Section 1.2.1**), as well as its potential in inorganic materials (**Section 1.2.2**).

1.2.1 Overview

Self-replication is one of the key processes that all living things exhibit to grow, survive, and evolve.[1–4] It is the ability of a system to make identical copies of itself along with the transfer

of information to the next generation. Self-replication is a subset of autocatalysis and so it is important to understand what makes a system autocatalytic. Autocatalysis occurs when a product catalyzes its own formation leading to an exponential growth in product formation. To illustrate this, the most simplistic example would be:

$$A + B \xrightarrow{C} C \tag{1.1}$$

Here, reactants A and B react to form C, whereby C acts as a catalyst to speed up the rate of reaction leading to a sigmoidal (or S-shaped) curve in concentration over time (**Figure 1.1**).

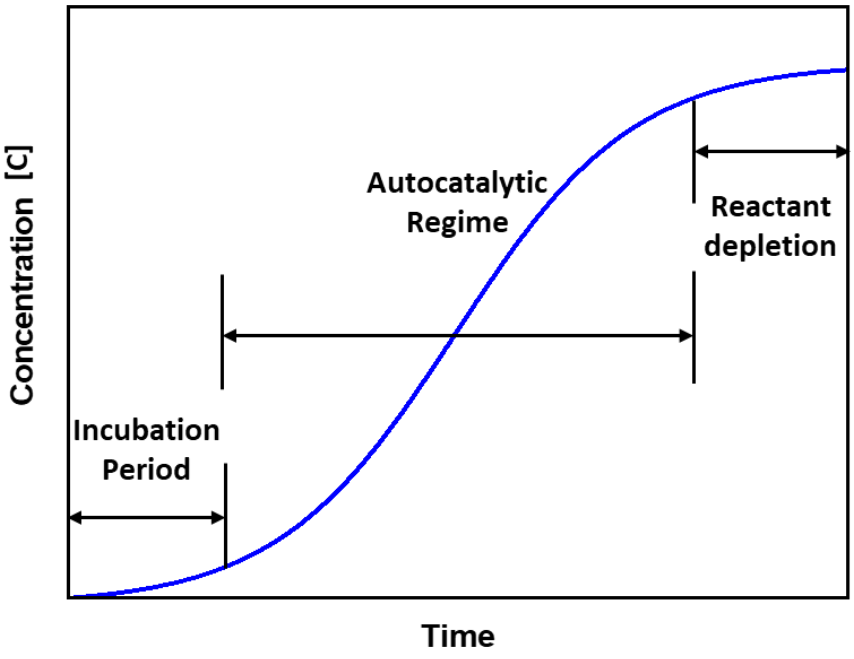

Figure 1.1. Characteristic sigmoidal curve of exponential growth in an autocatalytic system where product C catalyzes its own formation.

The sigmoidal curve is comprised of an initial lag period where the reaction is slow due to minimal concentration of catalyst C. The next phase consists of an exponential increase in the reaction rate due to an ever-increasing concentration of the catalyst. The final phase is the depletion of the reactants leading to no more production of C. One of the most classical and simplistic

examples of autocatalysis is the reaction of potassium permanganate ($KMnO_4$) with oxalic acid ($H_2C_2O_4$) seen here:[5,6]

$$2MnO_4^- + 5H_2C_2O_4 + 6H^+ \xrightarrow{Mn^{2+}} 2Mn^{2+} + 10CO_2 + 8H_2O \quad (1.2)$$

The manganese ion (Mn^{2+}) that is produced catalyzes the reaction to produce more of itself leading to exponential decomposition of $KMnO_4$. Although this reaction is autocatalytic, it is not self-replicating because there is no transfer of information. Information-storing species is a very broad topic and can come in many different forms depending on how it is defined exactly. This will be described more in detail in **Section 1.2.2**. With that, it can be noted that all self-replicating systems are autocatalytic, but not all autocatalytic systems are self-replicating.

Self-replication can be found in nature from the molecular all the way up the cellular scale. On the cellular level, self-replication is still complex and poorly understood, and therefore has directed research towards more minimalistic synthetic systems.[1,2,7,8] The most widely known and studied self-replicator found in cells is deoxyribonucleic acid (DNA), which is what many minimal replicating systems stems from. The most commonly studied organic minimal self-replicating systems are based on nucleic acids[9–11], peptides[12–15], and vesicle/protocells[3,4]. These systems typically follow either templated replication[4,9–14] or division[3] formats that are characteristic of organic systems.

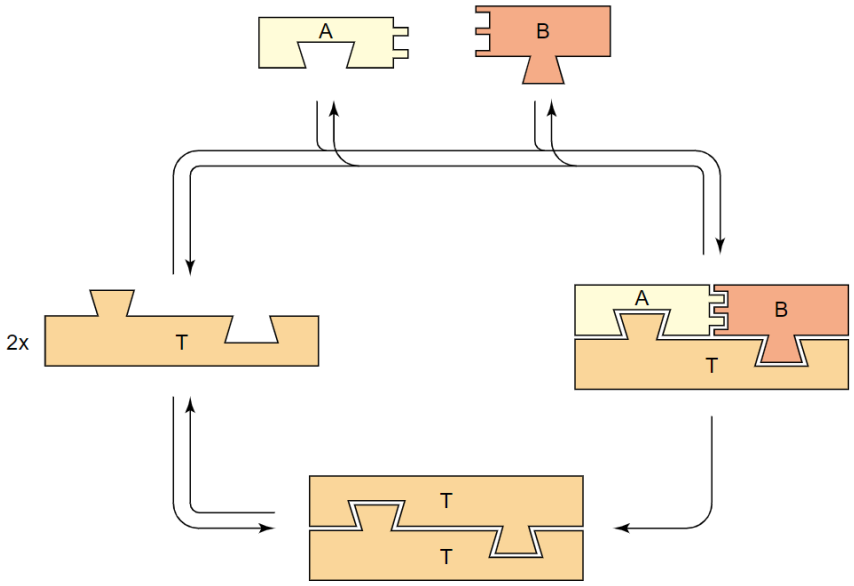

Figure 1.2. Example of templated replication for a synthetic minimal system. The template (T) binds to its two building blocks A and B. An irreversible reaction occurs between A and B to produce a copy of T. The two templates then dissociate where both begin another round of self-replication. Figure adapted from Ref.[2]

The most common method of replication in synthetic systems is based on template-directed interactions between molecules. These molecules, or building blocks, follow a two-step mechanism (**Figure 1.2**).[2] First, the template (T) binds to its building blocks (A and B) in a particular orientation to allow specific interactions between the building blocks to create a copy of T. The second step consists of dissociation of the two templates where they both become available for further replication. As more templates are formed, the rate of self-replication increases exponentially until all building blocks are consumed. The first synthetic system of self-replicators was developed by von Kiedrowski in 1986 with the template replication of a hexadeoxynucleotide from short DNA strands.[9] In this work, it was found that the kinetics follow a more parabolic trend rather than the ideal exponential trend. In fact, many templated self-replicating systems follow more parabolic trends.[1,12,13,16,17] The difference between the two trends can be explained from their reaction order where a sigmoidal curve, or exponential growth, correlates to a reaction order of 1,

and a parabolic curve correlates to a reaction order of ½. Example growth equations can be seen here:[1,16,17]

$$[A] = [A]_0 e^{rt} \tag{1.3}$$

$$[A] = ([A]_0^{1/2} + \frac{rt}{2})^2 \tag{1.4}$$

Here, t is time, [A] is the concentration of a replicator at time t, $[A]_0$ is the initial concentration of the replicator, and r is the Malthusian parameter which is the maximum exponential growth rate. **Equation 1.3** portrays exponential growth while **Equation 1.4** depicts parabolic growth. This deviation from exponential growth is caused by either product inhibition[12,13], which is seen a lot in templated replication, or competing reactions and damage/decay of the replicators[16], which his seen in many biological systems.

While the fundamental knowledge obtained from these organic systems is scientifically valuable, there is limited application beyond understanding the origin of life. To expand upon this field, it is promising to explore the self-replicating behavior of inorganic systems. This will be further explained in the next section.

1.2.2 Inorganic Replication

Inorganic systems would have numerous advantages over biological systems as they would be more robust, tunable, and simpler.[18,19] However, there have been few studies involving inorganic self-replicating systems.[20] The first ever inorganic self-replicating system theorized was that of clay minerals by Cairns-Smith in 1966.[21] In this theoretical work, he proposed that during the crystallization growth of clay minerals, certain lattice imperfections replicate as part of the process in a self-selecting manner and propagate from there. Experimental work supposedly

proving this theory was performed in 1981 by Weiss.[22] In this work, he stated that layered silicates undergo spontaneous self-multiplication, or replication during growth. Although this was published, later review on this work found that there is a lack of key experimental procedures to reproduce the data as well as other issues.[23,24] As a result, exploration into inorganic self-replicating systems went dormant for decades.

In recent years, research into inorganic materials for self-replication began to emerge again as technology became more advanced. Inorganic nanoparticles (NPs) stand out as a practical candidate due to their structural simplicity and environmental robustness. The ability to dynamically control the interaction of nanoparticles via external stimuli leads to the possibility of using them in a self-replicating system.[25] Self-replication comes in many forms, but the two most promising methods for inorganic systems are templated replication, which has been described in **Section 1.2.1**, and autocatalytic heterogeneous nucleation.[20]

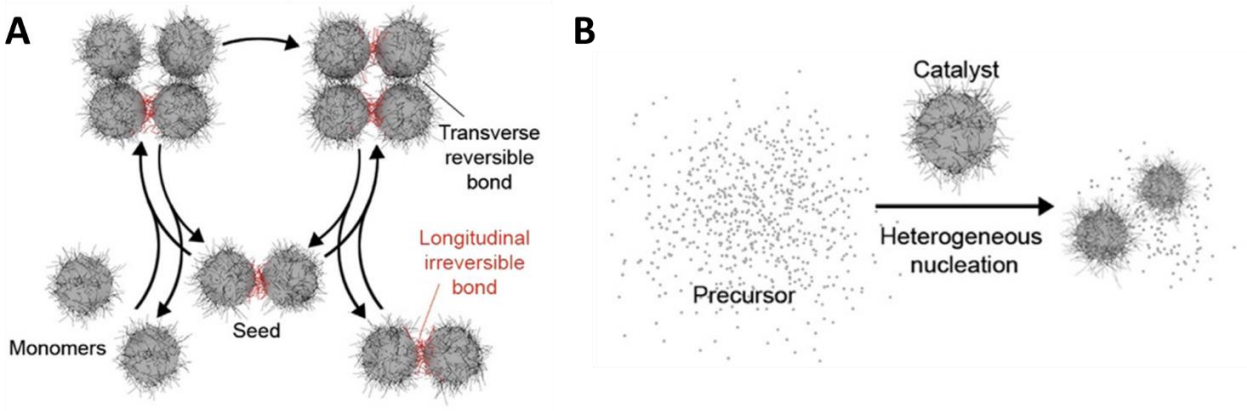

Figure 1.3. Schematics of two different types of colloidal self-replication. (A) templated replication: Irreversible bonding of particles templated by a dimer followed by disassembly into a copied dimer and **(B)** autocatalytic heterogeneous nucleation: particle catalyzes the formation of another particle at its interface from precursor in the solution. Figure adapted from Ref.[20]

For inorganic systems, templated replication consists of a template that bonds to multiple particles, induces an irreversible bond between the reactants to create a copy of itself, and then

disassembles for further replication (**Figure 1.3A**). The highly directional interaction between the template and reactants leads to minimal error between the original and copy. Templated replication is typically studied with the replication of colloidal clusters (i.e. dimers) from individual particles (monomers). However, this system is difficult to study experimentally, so current efforts have focused primarily on computational modeling. For example, Olvera de la Cruz et al. developed a computational model for self-replicating dimers of azobenzene coated gold nanoparticles.[26] They discovered that applying UV light to the system causes the particles to aggregate where the dimer templates can interact with individual particles and thus create more dimers in a self-replicating manner. The process can also be accelerated by applying a cyclic UV light input due to the reversibility of the particle aggregation. They further expanded upon their work by exploring the effects of asymmetric interactions between particles.[27] Their study showed that only dimers with small torsional angles between the monomers would have the capability of self-replication. The Brenner group also explored a similar system in which an octahedron particle cluster is self-replicated with the help of a dimer as a catalyst.[28] In their computational experiments, monomers from the surroundings are attached between the octahedron and dimer and formed into a six-member cluster that is then rearranged into a new octahedron. They expanded upon their work by exploring mutations during the self-replication process of square clusters.[29] The results indicated that over time, five particle chains and six particle hexagons begin to form in small percentages, and that mutation survival is dependent on the concentration of monomers near the mutated cluster. Even though these models give us substantial insight into template replication of inorganic colloidal system, there is not enough experimental data to support them.

Templated replication only replicates clusters from previously synthesized ‘seed’ particles, whereas autocatalytic heterogeneous nucleation leads to self-replication of individual particles

from precursor in the solution (**Figure 1.3B**). This type of self-replication is defined as a form of non-classical nucleation that combines autocatalytic reduction of precursor with heterogeneous nucleation at the interface of a 'parent' particle. This newly formed particle can produce its own 'daughter' particle and continue this cyclic chain of events, resulting in the characteristic sigmoidal curve of concentration over time indicative of replication. As particles are continually nucleating off previous 'parent' particles, this form of non-classical nucleation could also lead to uniquely complex geometries and hierarchical assemblies[30–32], which is not seen in classical inorganic particle nucleation[33]. Self-replication via heterogeneous nucleation to our knowledge has not been realized for inorganic nanoparticles and therefore leaves a lot of potential for exploration. As a result, the work in this thesis will focus on this inorganic form of self-replication.

NP nucleation at interfaces has been studied on single and multi-component surfaces before but leads to coalescence or attachment of the particle to the parent material leading to growth instead of replication.[34–37] To realize this form of self-replication, nucleation must occur at the interface with no direct connection between particles to allow the formation of an independent 'daughter' NP. Additionally, for this system to be considered self-replicating, there must be an information transfer of some sort with the 'daughter' particle. Replication information is a very broad term and is used loosely in literature.[38,39] It can be anywhere from the sequence of constituents to the physiochemical properties of the structures. Here we will describe the replication information as the geometrical shape and size of the particles after they are fully grown.[38] To realize this form of self-replication, plasmonic nanoparticles were used in this thesis. The next section will detail what plasmonic nanoparticles are and how they can be useful for this system.

1.3 Plasmonic Nanoparticles

Even before plasmonic nanoparticles were scientifically discovered, their uses date all the way back to 4th century ancient Rome in stained glass and the creation of the Lycurgus Cup, which contained traces of silver and gold nanoparticles dispersed in the glass. Plasmonic nanoparticles are metallic particles that have highly unique optical properties depending on their composition, size, and shape. The section will provide background on common plasmonic nanoparticle synthesis and kinetics (**Section 1.3.1**) as well as how chirality can arise in plasmonic systems (**Section 1.3.2**).

1.3.1 Synthesis Pathways and Kinetics

Plasmonic nanoparticles are metallic particles that strongly absorb and scatter light typically in the ultraviolet (UV) to the near-infrared (IR) regions of the electromagnetic spectrum depending on their size and shape. Their unique optical properties arise from a phenomenon known as a localized surface plasmon resonance (LSPR) when illuminated with a specific wavelength of light. LSPR is a collective oscillation of the conduction electrons of metallic nanoparticles when their size is smaller or comparable to the wavelength of the excitation light (**Figure 1.4**). There are a wide range of metallic nanoparticles (Ag, Au, Cu, Al, Mg, and Pt) that are plasmonic, but the two most common are silver (Ag) and gold (Au).[40] Dispersed aqueous silver nanoparticles below 100 nm have an observable yellow color due to strong absorption in the violet/blue region (400 nm – 500 nm), whereas spherical gold nanoparticle below 100 nm are red due to strong absorption in the green/ yellow region (500 nm – 600 nm).

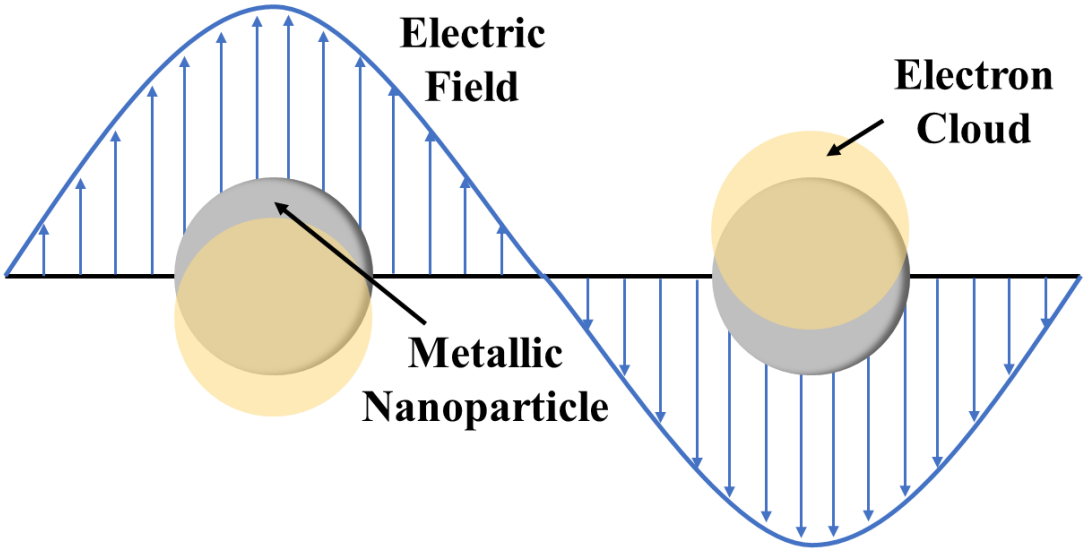

Figure 1.4. Schematic of LSPR on a metallic nanoparticle

When synthesizing plasmonic nanoparticles, a reducing agent and a stabilizer are required. A reducing agent is a reactant that donates an electron to an oxidizing agent. For example, in the case of silver nanoparticle synthesis, a reducing agent would donate an electron to a silver ion (Ag^{+}) to reduce it to a silver atom (Ag^{0}) where the colloidal Ag^{0} bind into a cluster until they reach a critical radius at which the silver nanoparticle becomes favorable and stable.[41] The most common reducing agents seen in literature are sodium borohydride ($NaBH_4$)[42–44], a strong reducing agent, sodium citrate dihydrate (citrate)[45–47], a weak reducing agent.

A stabilizer is a ligand that helps stabilize and maintain the shape the NPs as they begin to nucleate and grow. A stabilizer is required as the NPs would aggregate and precipitate out of solution, due to attractive forces, instead of remaining dispersed in solution. An example of a system without a stabilizer is the silver mirror reaction, which forms silver nanoparticles of various sizes on a substrate to form a reflective surface.[48,49] Without any electrical input to induce this coating, this is also known as electroless plating, which will be discussed further in **Chapter 2**. There are two types of stabilizers for nanoparticles: electrostatic and steric. Electrostatic stabilizers

typically consist of ionic surfactants that create an electrical double layer (EDL) around the particles. When two particle's EDL overlap, there are repulsive forces that overcome the van der Waals attractive forces that allows the particles to not aggregate and remain dispersed in solution. The most common electrostatic stabilizers seen for silver and gold nanoparticle synthesis are citrate[45–47], $NaBH_4$[42–44], and cetyltrimethylammonium bromide (CTAB)[50,51].

Steric stabilizers are nonionic or polymer surfactants adsorbed on the surface of the colloidal particle. These stabilizers physically prevent two particles from getting too close to allow attractive forces to induce aggregate due to the high density of adsorption. The most common steric stabilizers are polyvinylpyrrolidone (PVP) and polyvinyl alcohol (PVA) for nanoparticle synthesis.[51]

The most common method for synthesis of silver nanoparticles is the Turkevich method. The Turkevich method was initially developed for gold nanoparticles but has been shown to be just as effective for silver as well. Here, an aqueous solution of precursor, tetrachloroauric acid ($HAuCl_4$) for gold nanoparticles and silver nitrate ($AgNO_3$) for silver nanoparticles, is brought to a boil under constant stirring. An aqueous solution of citrate is then added dropwise and the ensuing solution if left to stir until a red or yellow color is observed for gold and silver, respectively. Here citrate is acting as both the reducing agent and the stabilizer to lead to spherical nanoparticle formation. Numerous other methods of synthesis have been developed using chemical reduction methods and even light to create more unique shapes of particles, such as rods[52,53], cubes[54], prisms[52,55], etc.

The mechanism for nanoparticle synthesis is commonly explained using classical nucleation theory for colloidal systems. When it comes to nucleation and growth of nanoparticles,

there are two mechanisms that are most prevalent: LaMer Burst nucleation coupled with Ostwald Ripening and the Finke-Watzky continuous nucleation and autocatalytic growth mechanism.

LaMer burst nucleation was first theorized in 1950, where nucleation and growth were thought to be two separate stages in colloidal synthesis.[33,41,56] Nucleation consists of two steps (**Figure 1.5**): (I) the concentration of reduced metallic atoms rapidly increases until it reaches a critical concentration, (II) this supersaturated solution undergoes 'burst-nucleation' whereby nuclei form at an effectively infinite rate until the concentration of precursor falls below this critical concentration. In the growth step, stage III, the particles then undergo growth by diffusion of precursor to the surface of the nuclei. This mechanism can be coupled with Ostwald ripening where the smaller particles, due to their high surface energy, will redissolve and allow the larger particles to grow more.[41,57]

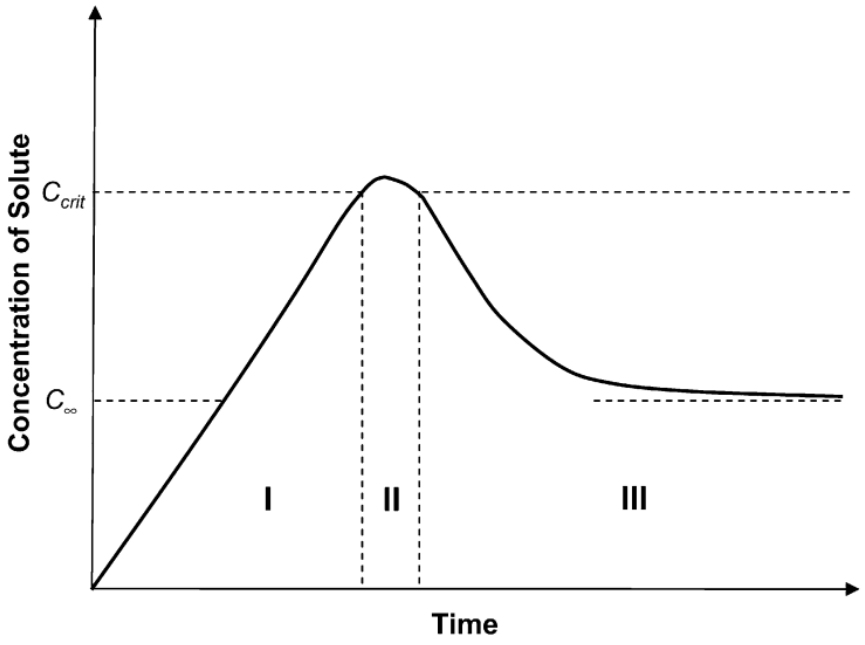

Figure 1.5. LaMer burst nucleation of solute concentration over time. Stage I entails the increase in solute concentration up to the critical supersaturated concentration, at which stage II begins where nucleation occurs at an effective infinite rate. Once the solute concentration reaches below are certain threshold, nucleation stops and growth of the particles occurs (stage III).

The Finke-Watzky mechanism was developed in 1997 to support the synthesis of nanoparticle systems that could not be explained using LaMer burst nucleation.[58] Instead of having nucleation and growth as two separate entities, the Fink-Watzky mechanism proposes that both nucleation and growth occur simultaneously. The mechanism is broken down into two simultaneous steps: slow continuous nucleation and fast autocatalytic NP growth. The equations can be seen here:

$$A \rightarrow B \tag{1.5}$$

$$A + B \rightarrow 2B \tag{1.6}$$

Here, A is the precursor and B is the growing nanoparticle. **Equation 1.5** describes the continuous nucleation, while **Equation 1.6** describes the reduction of precursor on the surface of the nanoparticle leading to growth, which is autocatalytic since B is catalyzing the reaction. This mechanism has been shown to be a good fit for certain chemical reduction methods of gold and silver nanoparticle.[59,60]

Classical nucleation can describe very simplistic nanoparticle systems, but what happens when the particles start to become more complex in their shape or self-assemble as they nucleate? This is where we start to dive into mechanisms that deviate from the ideal conditions, leading into the area of nonclassical nucleation. Nonclassical nucleation is a growing field as it can be used to help describe the mechanism behind particles of shapes other than spherical as well as multicomponent nanoparticles.[30] I can also be used to explain the mechanism behind systems where self-assembly or agglomeration occurs. In this dissertation, self-replication of inorganic nanoparticles from their precursor in solution is explored. This form of self-replication, which entails autocatalytic heterogeneous nucleation and self-assembly, falls under this area of

nonclassical nucleation. As a result, it is important to find a mechanism outside of classical theory that can support this work.

1.3.2 Chirality in Plasmonic Nanoparticles

The term chiral comes from the Greek word ‘cheir’, which means ‘handedness’.[61] Chiral objects are those that cannot be superimposed on their mirror images. The two mirror objects are termed enantiomers, which are commonly referred to as either left- or right-handed. Chirality has been explored extensively in organic chemistry and is very well understood.[61,62] In the field of inorganic nanostructures, chirality is still evolving and as such there is still a lot of work to be done to fully understand their properties, especially their chiroptical characteristics.

For plasmonic nanoparticles, the combination of the plasmonic effect coupled with chirality opens a wide range of applications in sensing, catalysis, and photonics.[63–66] Chirality in plasmonic nanoparticles can arise from either the asymmetric geometry of the individual particles or assembly of particles, or it can come from chiral ligands used to stabilize the particles. In our lab, we have developed numerous chiral materials from single particle gold nanoparticles[67] to complex assemblies like chiral ribbons[68,69]. The work that stands out for this dissertation is the use of circularly polarized light (CPL) to transfer chirality directly from photon to matter. Depending on the handedness of the CPL, the different enantiomers were able to be produced. In this thesis, we look to explore if chirality can be coupled with self-replication to further expand the uses of the system in **Chapter 5**.

1.4 Research Goals

The work proposed here seeks to create a novel abiotic colloidal self-replicating system that has never been reported to date. The main goals are to realize a simplistic inorganic self-replicating nanoparticle system, as well as expanding upon that knowledge to create more complex self-replicating systems through self-assembly on surfaces and chiral asymmetry.

Chapter 2: Research Design and Methods

This chapter presents an overview of all experimental and characterization techniques used to obtain results in this dissertation. The first section details all the synthesis techniques used with a focus on the self-replication of the silver nanoparticles, as well as their use on surfaces and in chiral structures. The second half details all the characterization techniques, both ex-situ and in-situ, for evaluating all synthesis techniques. This information serves to provide a detailed guide to reproduce this work as well as expand it further.

Chapter 3: The Search for an Inorganic Self-Replicating System

This chapter contains all the work done to find an inorganic system that shows self-replicating characteristics. A high-throughput screening method is developed to efficiently analyze over 100 inorganic systems. The screening method consists of three steps, which one only system passed all three to be chosen as the prime candidate for future exploration. As not every system can be incorporated into this dissertation, prime examples of systems that did not pass each step are described and detailed why it was not further tested in latter steps.

Chapter 4: Coupled Self-Replication and Self-Assembly of Inorganic Nanoparticles

In this chapter, the most promising self-replicating inorganic system from **Chapter 3** is further tested to evaluate if it is indeed self-replicating and how. Numerous ex-situ characterization techniques are used to evaluate the kinetics, structure, and assembly of the nanoparticles. Further in-situ techniques are used to view in real time the nucleation and growth of these particles to visually confirm the presence of self-replication. Lastly, a kinetic model is developed to help computationally support the experimental trends in concentration as well as size over time.

Chapter 5: Exploration into Bioinspired Manufacturing Applications

This chapter details all the work done in finding suitable applications for the self-replicating AgNPs. The applications are broken down into two categories: replication on surfaces and chiral materials. Self-replicating AgNPs are grown on functionalized flat and corrugated surfaces to create unique assemblies that can further be expanded with electroless deposition. Our work on growing chiral silver helicoids on substrates is detailed here and how we can use these results to potentially create chiral self-replicating NPs both in solution.

Chapter 6: Conclusions and Future Recommended Works

This chapter summarizes all the key findings from the results in the previous chapters and how they have helped expand the field of self-replication to never before seen territory. Based on these results, I suggest future potential pathways for this line of work. As this is the first time to our knowledge that this form of self-replication has been proven for inorganic systems, there are a large variety of routes both from different materials as well as applications.

1.5 References

1. G. Clixby, L. Twyman, Self-Replicating Systems. *Org Biomol Chem*. **14**, 4170–4184 (2016).

2. N. Paul, G. F. Joyce, Minimal Self-Replicating Systems. *Curr Opin Chem Biol*. **8**, 634–639 (2004).

3. J. W. Taylor, S. A. Eghtesadi, L. J. Points, T. Liu, L. Cronin, Autonomous Model Protocell Division Driven by Molecular Replication. *Nat Commun*. **8**, (2017).

4. P. van Nies, I. Westerlaken, D. Blanken, M. Salas, M. Mencía, C. Danelon, Self-Replication of DNA by its Encoded Proteins in Liposome-Based Synthetic Cells. *Nat Commun*. **9**, 1–12 (2018).

5. H. F. Launer, The Kinetics of the Reaction between Potassium Permanganate and Oxalic Acid. I. *J Am Chem Soc*. **54**, 2597–2610 (1932).

6. H. F. Launer, D. M. Yost, The Kinetics of the Reaction between Potassium Permanganate and Oxalic Acid. II. *J Am Chem Soc*. **56**, 2571–2577 (1934).

7. J. W. Sadownik, E. Mattia, P. Nowak, S. Otto, Diversification of Self-Replicating Molecules. *Nat Chem*. **8**, 264–269 (2016).

8. A. Robertson, A. J. Sinclair, D. Philp, Minimal Self-Replicating Systems. *Chem Soc Rev*. **29**, 141–152 (2000).

9. G. von Kiedrowski, A Self-Replicating Hexadeoxynucleotide. *Angewandte Chemie International Edition in English*. **25**, 932–935 (1986).

10. N. Paul, G. F. Joyce, A Self-Replicating Ligase Ribozyme. *Proc Natl Acad Sci U S A*. **99**, 12733–12740 (2002).

11. C. Olea, D. P. Horning, G. F. Joyce, Ligand-Dependent Exponential Amplification of a Self-Replicating L-RNA Enzyme. *J Am Chem Soc*. **134**, 8050–8053 (2012).

12. D. H. Lee, J. R. Granja, J. A. Martinez, K. Severin, M. R. Ghadiri, A Self-Replicating Peptide. *Nature*. **382**, 525–528 (1996).

13. X. Li, J. Chmielewski, Peptide Self-Replication Enhanced by a Proline Kink. *J Am Chem Soc*. **125**, 11820–11821 (2003).

14. K. Ikeda, M. Nakano, Self-Reproduction of Nanoparticles Through Synergistic Self-Assembly. *Langmuir*. **31**, 17–21 (2015).

15. B. Liu, C. G. Pappas, J. Ottelé, G. Schaeffer, C. Jurissek, P. F. Pieters, M. Altay, I. Marić, M. C. A. Stuart, S. Otto, Spontaneous Emergence of Self-Replicating Molecules Containing Nucleobases and Amino Acids. *J Am Chem Soc*. **142**, 4184–4192 (2020).

16. P. Adamski, M. Eleveld, A. Sood, Á. Kun, A. Szilágyi, T. Czárán, E. Szathmáry, S. Otto, From Self-Replication to Replicator Systems en Route to de Novo Life. *Nat Rev Chem*. **4**, 386–403 (2020).

17. G. von Kiedrowski, *Minimal Replicator Theory I: Parabolic Versus Exponential Growth. In: Dugas, H., Schmidtchen, F.P. (eds) Bioorganic Chemistry Frontiers, vol 3* (1993).

18. N. A. Kotov, Inorganic Nanoparticles as Protein Mimics. *Science* **330**, 188–189 (2010).

19. S. Li, J. Liu, N. S. Ramesar, H. Heinz, L. Xu, C. Xu, N. A. Kotov, Single- and Multi-Component Chiral Supraparticles as Modular Enantioselective Catalysts. *Nat Commun*. **10**, 1–10 (2019).

20. M. Grzelczak, Colloidal Systems Chemistry. Replication, Reproduction and Selection at Nanoscale. *J Colloid Interface Sci*. **537**, 269–279 (2019).

21. A. G. Cairns-Smith, The Origin of Life and the Nature of the Primitive Gene. *J. Theoret. Biol*. **10**, 53–88 (1965).

22. A. Weiss, Replication and Evolution in Inorganic Systems. *Angewandte Chemie International Edition in English*. **20**, 850–860 (1981).

23. G. Arrhenius, A. G. Cairns-Smith, H. Hartman, S. L. Miller, L. E. Orgel, Remarks on the Review Article "Replication and Evolution in Inorganic Systems." *Angewandte Chemie International Edition in English*. **98**, 654 (1986).

24. J. T. Kloprogge, H. Hartman, Clays and the Origin of Life: The Experiments. *Life*. **12**, (2022).

25. M. Grzelczak, L. M. Liz-Marzán, R. Klajn, Stimuli-Responsive Self-Assembly of Nanoparticles. *Chem Soc Rev*. **48**, 1342–1361 (2019).

26. R. Zhang, D. A. Walker, B. A. Grzybowski, M. Olvera de la Cruz, Accelerated Self-Replication under Non-Equilibrium, Periodic Energy Delivery. *Angewandte Chemie*. **126**, 177–181 (2014).

27. R. Zhang, J. M. Dempster, M. Olvera De La Cruz, Self-Replication in Colloids with Asymmetric Interactions. *Soft Matter*. **10**, 1315–1319 (2014).

28. Z. Zeravcic, M. P. Brenner, Self-Replicating Colloidal Clusters. *Proc Natl Acad Sci U S A*. **111**, 1748–1753 (2014).

29. H. Tanaka, Z. Zeravcic, M. P. Brenner, Mutation at Expanding Front of Self-Replicating Colloidal Clusters. *Phys Rev Lett*. **117**, 1–6 (2016).

30. J. Lee, J. Yang, S. G. Kwon, T. Hyeon, Nonclassical nucleation and growth of inorganic nanoparticles. *Nat Rev Mater*. **1**,1–16 (2016).

31. R. Tang, B. Jin, B. Jin, Z. Liu, Recent Experimental Explorations of Non-Classical Nucleation. *CrystEngComm*. **22**, 4057–4073 (2020).

32. K. J. Wu, E. C. M. Tse, C. Shang, Z. Guo, Nucleation and Growth in Solution Synthesis of Nanostructures – From Fundamentals to Advanced Applications. *Prog Mater Sci*. **123**, 100821 (2022).

33. V. K. Lamer, R. H. Dinegar, Theory, Production and Mechanism of Formation of Monodispersed Hydrosols. *J Am Chem Soc*. **72**, 4847–4854 (1950).

34. S. G. Kwon, G. Krylova, P. J. Phillips, R. F. Klie, S. Chattopadhyay, T. Shibata, E. E. Bunel, Y. Liu, V. B. Prakapenka, B. Lee, E. v Shevchenko, Heterogeneous Nucleation and Shape Transformation of Multicomponent Metallic Nanostructures. *Nat Mater*. **14**, 215–223 (2015).

35. X. Zhong, R. Xie, Y. Zhang, T. Basché, W. Knoll, High-Quality Violet- to Red-Emitting ZnSe/CdSe Core/Shell Nanocrystals. *Chemistry of Materials*. **17**, 4038–4042 (2005).

36. G. Zhu, M. L. Sushko, J. S. Loring, B. A. Legg, M. Song, J. A. Soltis, X. Huang, K. M. Rosso, J. J. de Yoreo, Self-Similar Mesocrystals Form via Interface-Driven Nucleation and Assembly. *Nature*. **590**, 416–422 (2021).

37. Y. Cheng, J. Tao, G. Zhu, J. A. Soltis, B. A. Legg, E. Nakouzi, J. J. de Yoreo, M. L. Sushko, J. Liu, Near Surface Nucleation and Particle Mediated Growth of Colloidal Au Nanocrystals. *Nanoscale*. **10**, 11907–11912 (2018).

38. R. Schulman, B. Yurke, E. Winfree, Robust Self-Replication of Combinatorial Information via Crystal Growth and Scission. *Proc Natl Acad Sci U S A*. **109**, 6405–6410 (2012).

39. I. A. Chen, P. Walde, From Self-Assembled Vesicles to Protocells. *Cold Spring Harbor Perspectives in Biology* **2**, (2010).

40. A. N. Koya, X. Zhu, N. Ohannesian, A. A. Yanik, A. Alabastri, R. P. Zaccaria, R. Krahne, W.-C. Shih, D. Garoli, Nanoporous Metals: From Plasmonic Properties to Applications in Enhanced Spectroscopy and Photocatalysis. *ACS Nano.* **15**, (2021).

41. N. T. K. Thanh, N. Maclean, S. Mahiddine, Mechanisms of Nucleation and Growth of Nanoparticles in Solution. *Chem Rev*. **114**, 7610–7630 (2014).

42. K. Mavani, M. Shah, Synthesis of Silver Nanoparticles by using Sodium Borohydride as a Reducing Agent. *International Journal of Engineering Research & Technology* **2**, 1-5 (2013).

43. S. Solomon, M. Bahadori, A. v Jeyarajasingam, S. A. Rutkowsky, C. Boritz, L. Mulfinger, Synthesis and Study of Silver Nanoparticles. *Journal of Chemical Education* **84**, (2007).

44. J. K. Lee, D. Samanta, H. G. Nam, R. N. Zare, Spontaneous Formation of Gold Nanostructures in Aqueous Microdroplets. *Nature Communications* **9**, 1–9 (2018).

45. J. Turkevich, P. C. Stevenson, J. Hillier, A Study of the Nucleation and Growth Processes in the Synthesis of Colloidal Gold. *Discuss Faraday Soc*. **11**, 55–75 (1951).

46. J. Kimling, M. Maier, B. Okenve, V. Kotaidis, H. Ballot, A. Plech, Turkevich Method for Gold Nanoparticle Synthesis Revisited. *Journal of Physical Chemistry B*. **110**, 15700–15707 (2006).

47. G. Frens, Controlled Nucleation for the Regulation of the Particle Size in Monodisperse Gold Suspensions. *Nature Physical Science* **241**, 20–22 (1973).

48. B. Tollens, Ueber ammon-alkalische Silberlösung als Reagens auf Aldehyd. *Berichte der deutschen chemischen Gesellschaft*. **15**, 1635–1639 (1882).

49. S. Schaefers, L. Rast, A. Stanishevsky, Electroless Silver Plating on Spin-Coated Silver Nanoparticle Seed Layers. *Mater Lett*. **60**, 706–709 (2006).

50. J. I. Hussain, S. Kumar, A. A. Hashmi, Z. Khan, Silver Nanoparticles: Preparation, Characterization, and Kinetics. *Adv Mater Lett*. **2**, 188–194 (2011).

51. S. Das, K. Bandyopadhyay, M. M. Ghosh, Effect of Stabilizer Concentration on the Size of Silver Nanoparticles Synthesized Through Chemical Route. *Inorg Chem Commun*. **123**, (2021).

52. K. G. Stamplecoskie, J. C. Scaiano, Light Emitting Diode Irradiation can Control the Morphology and Optical Properties of Silver Nanoparticles. *J Am Chem Soc*. **132**, 1825–1827 (2010).

53. C. R. Rekha, V. U. Nayar, K. G. Gopchandran, Synthesis of Highly Stable Silver Nanorods and Their Application as SERS Substrates. *Journal of Science: Advanced Materials and Devices*. **3**, 196–205 (2018).

54. S. Zhou, J. Li, K. D. Gilroy, J. Tao, C. Zhu, X. Yang, X. Sun, Y. Xia, Facile Synthesis of Silver Nanocubes with Sharp Corners and Edges in an Aqueous Solution. *ACS Nano*. **10**, 9861–9870 (2016).

55. X. Dong, X. Ji, J. Jing, M. Li, J. Li, W. Yang, Synthesis of Triangular Silver Nanoprisms by Stepwise Reduction of Sodium Borohydride and Trisodium Citrate. *The Journal of Physical Chemistry C* **114**, 2070-2074 (2010).

56. T. Sugimoto, Underlying Mechanisms in Size Control of Uniform Nanoparticles. *J Colloid Interface Sci*. **309**, 106–118 (2007).

57. W. Ostwald, Über die vermeintliche Isomerie des roten und gelben Quecksilberoxyds und die Oberflächenspannung fester Körper. *Zeitschrift für Physikalische Chemie.* **34**, 495–503 (1900).

58. M. A. Watzky, R. G. Finke, Transition Metal Nanocluster Formation Kinetic and Mechanistic Studies. A New Mechanism When Hydrogen is the Reductant: Slow,

Continuous Nucleation and Fast Autocatalytic Surface Growth. *J Am Chem Soc*. **119**, 10382–10400 (1997).

59. M. A. Watzky, R. G. Finke, Gold Nanoparticle Formation Kinetics and Mechanism: A Critical Analysis of the "redox Crystallization" Mechanism. *ACS Omega*. **3**, 1555–1563 (2018).

60. A. Kytsya, L. Bazylyak, Y. Hrynda, A. Horechyy, Y. Medvedevdkikh, The Kinetic Rate Law for the Autocatalytic Growth of Citrate-Stabilized Silver Nanoparticles. *Int J Chem Kinet*. **47**, 351–360 (2015).

61. L. A. Nguyen, H. He, C. Pham-Huy, Chiral Drugs: An Overview. *Int J Biomed Sci*. **2**, 85 (2006).

62. R. Janoschek, Theories on the Origin of Biomolecular Homochirality. *Chirality*, 18–33 (1991).

63. A. Kuzyk, R. Schreiber, Z. Fan, G. Pardatscher, E. M. Roller, A. Högele, F. C. Simmel, A. O. Govorov, T. Liedl, DNA-Based Self-Assembly of Chiral Plasmonic Nanostructures with Tailored Optical Response. *Nature* **483**, 311–314 (2012).

64. J. Cai, W. Zhang, L. Xu, C. Hao, W. Ma, M. Sun, X. Wu, X. Qin, F. M. Colombari, A. F. de Moura, J. Xu, M. C. Silva, E. B. Carneiro-Neto, W. R. Gomes, R. A. L. Vallée, E. C. Pereira, X. Liu, C. Xu, R. Klajn, N. A. Kotov, H. Kuang, Polarization-Sensitive Optoionic Membranes from Chiral Plasmonic Nanoparticles. *Nat Nanotechnol*. **17**, 408–416 (2022).

65. Z. Wang, F. Cheng, T. Winsor, Y. Liu, Optical Chiral Metamaterials: a Review of the Fundamentals, Fabrication Methods and Applications. *Nanotechnology*. **27**, 412001 (2016).

66. K. Sawai, R. Tatumi, T. Nakahodo, H. Fujihara, Asymmetric Suzuki–Miyaura Coupling Reactions Catalyzed by Chiral Palladium Nanoparticles at Room Temperature. *Angewandte Chemie*. **120**, 7023–7025 (2008).

67. J. Y. Kim, J. Yeom, G. Zhao, H. Calcaterra, J. Munn, P. Zhang, N. Kotov, Assembly of Gold Nanoparticles into Chiral Superstructures Driven by Circularly Polarized Light. *J Am Chem Soc*. **141**, 11739–11744 (2019).

68. S. Srivastava, A. Santos, K. Critchley, K. S. Kim, P. Podsiadlo, K. Sun, J. Lee, C. Xu, G. D. Lilly, S. C. Glotzer, N. A. Kotov, Light-controlled self-assembly of semiconductor nanoparticles into twisted ribbons. *Science*. **327**, 1355–1359 (2010).

69. J. Yeom, B. Yeom, H. Chan, K. W. Smith, S. Dominguez-Medina, J. H. Bahng, G. Zhao, W. S. Chang, S. J. Chang, A. Chuvilin, D. Melnikau, A. L. Rogach, P. Zhang, S. Link, P. Král, N. A. Kotov, Chiral templating of self-assembling nanostructures by circularly polarized light. *Nat Mater*. **14**, 66–72 (2015).

Chapter 2 Research Design and Methods

2.1 Summary

This chapter details all the synthesis and characterisation methods used to accomplish the work for this dissertation. **Section 2** details all techniques used to synthesis nanoparticles for self-replication, surface functionalization, and chiral materials. **Section 3** provides thorough descriptions and theories of the numerous characterization techniques. This chapter is intended to provide insight needed to reproduce all results in this dissertation. It also serves as a template for incoming graduate students to incorporate these methods into their own experimental designs.

2.2 Synthesis Techniques

The following subsections details the synthesis techniques for various materials in this dissertation.

2.2.1 Light Assisted Synthesis of Silver Nanoparticles

The most common form of silver nanoparticle synthesis is chemical reduction via the Turkevich method where citrate is used as both the reducing agent and stabilizer.[1] Light has been used previously to synthesize silver nanoparticles (AgNPs) of shapes such as spheres, rods, and prisms, as well as induce unique self-assemblies of 'seed' particles.[2–5] This is due to their unique plasmonic optical characteristics and their autocatalytic growth, which can be tuned to grow in specific directions. In this dissertation, we seek to use light to drive autocatalytic heterogeneous nucleation coupled with self-assembly to create a novel inorganic self-replicating system.

For **Chapters 3**, AgNPs were synthesized through a photoinduced reaction with an 8 W 365 nm ultraviolet (UV) portable lamp (Analytik Jena). Multiple systems consisting of aqueous silver nitrate ($AgNO_3$) with different reducing agents and stabilizers were tested, where the set of systems can be seen in **Chapter 3.** Varying concentrations of $AgNO_3$ were used as the AgNP precursor for all systems. Varying reducing agents and stabilizers were added to the solution in a variety of concentrations. The solutions are placed in an ice bath and dark environment to maintain a constant temperature of 3-5^{o}C throughout the synthesis while eliminating any thermodynamic effects caused by heating from the light source and to eliminate ambient light effects, respectively. During the reaction, the solution is illuminated with the UV lamp for varying time lengths while being constantly agitated with a stir bar. Aliquots of the solution were taken at various time points during the synthesis and characterized immediately under ultraviolet-visible (UV-Vis) spectroscopy to ensure AgNPs are forming.

For most experiments in **Chapter 4**, 3 mM citrate and 0.1 mM $AgNO_3$ were mixed in a 50 mL volume of water. 0.1 M sodium hydroxide (NaOH) was added dropwise to the solution while stirring until the solution reached a pH of 10.3. The concentration of the silver precursor was chosen so that the final concentration of plasmonic AgNPs does not saturate the UV-Vis spectrometer throughout the entire synthesis. The solution was placed in an ice bath and dark environment to maintain a constant temperature of 3-5^{o}C throughout the synthesis while eliminating any thermodynamic effects caused by heating from the light source and to eliminate ambient light effects, respectively. During the reaction, the solution is illuminated with the UV lamp for up to 3 hours while constantly agitated with a stir bar. For experiments with the 8 W lamp, light intensity at the solution was 1.3 mW/cm^2. For the higher intensity light experiments, a 100 W 365 nm high intensity portable UV lamp (Analytik Jena) was used and the distance between

the solution and light was adjusted for the other two light intensities used in this chapter (8 and 17.2 mW/cm^2).

2.2.2 Layer-by-Layer Polymer Functionalization of Substrates

In **Chapter 4**, to help prove that the system is self-replicating, the AgNP assemblies needed to be captured while they were interacting. Traditional transmission electron microscopy (TEM) techniques, such as drop-casting the solution on a TEM grid and allowing it to dry, do not work for this goal as the AgNPs will aggregate during the drying process. So, one would not know if the AgNPs are assembling or if they are just aggregating while drying. Therefore, we needed a new technique that can capture the AgNP assemblies in real time on a TEM grid while avoiding drying effects.

To capture AgNP assemblies as they are self-replicating during the synthesis, TEM grids were functionalized with a layer-by-layer (LbL) of the polycation poly(diallyldimethylammonium chloride) (PDDA) and polyanion poly(sodium styrene sulfonate) (PSS).[6,7] LbL utilizes the alternating adsorption of oppositely charged polymers via electrostatic attraction to create nanometer scale thin films on substrates (**Figure 2.1**). These LbL films will adsorb nanoparticles of opposite charge depending on which polymer is the final layer.[8] For AgNPs stabilized by citrate, which are negatively charged, a final layer of PDDA will lead to adsorption of the particles while avoiding additional heterogeneous nucleation on the film due to the positive charge of silver ions in solution. Therefore, any particles and assemblies captured on the LbL film will be those that have formed in solution.

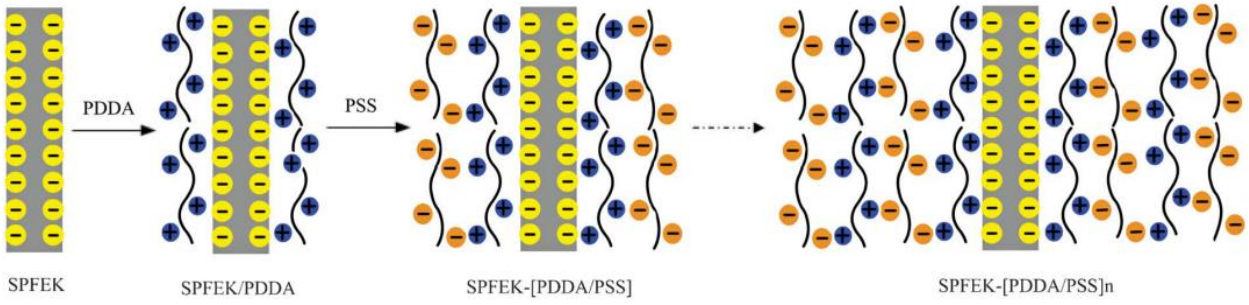

Figure 2.1. Schematics of LbL functionalization of a substrate. In this case sulfonated poly(fluorenyl ether ketone) (SPFEK), with PDDA and PSS. Figure adapted from Ref.[7]

In **Chapters 4 and 5**, LbL deposition was performed first with PDDA, where the TEM grid was submerged in a 1 wt% aqueous solution of PDDA for 10 minutes. The TEM grid was removed and washed 3 times with water to remove any residual PDDA solution. The grid is air dried and then submerged in a 1 wt% aqueous solution of PSS for 10 minutes. The grid was again washed 3 times with water and allowed to air dry. This process was repeated to create 3 bilayers to ensure a uniform coating. One more layer of PDDA was applied to leave the surface positively charged to attract the negatively charged AgNPs. The functionalized TEM grid was dipped in the reaction solution at the inflection point of the synthesis (60 min), where there should be the maximum rate of self-replication and the most AgNP assemblies, and immediately removed to prevent any additional nucleation on the grid. The TEM grid was the washed with water 3 times to remove any residual reaction solution and leave only the moment-in-time capture of the assemblies. The grid was air dried, and the assemblies were then imaged in under TEM.

2.2.3 Growth of Self-Replicating Networks on Substrates

Self-replication, which is a form of non-classical nucleation, could lead to complex organization of hierarchical assemblies.[9,10] Allowing AgNPs to propagate across a surface as they self-replicate can lead to thin films of complex networks.

In **Chapter 5**, AgNPs were grown on various substrates using a functionalized surface. LbL deposition of PDDA and PSS were performed on silicon monoxide (SiO) TEM grids (Ted Pella) and glass coverslips (Thermo Fisher Scientific) following the method described in **Section 2.2.2**. The substrates are washed with water to remove any excess polymer and dried at room temperature. The substrates are then supported on the surface of the solution at the inflection point of the self-replicating synthesis (60 min) to allow only growth on the submerged side and to prevent any attenuation effects that might occur if the substrate was completely submerged. The substrate is then removed from the surface of the solution after 30 min when formation of new NPs significantly decreases. The substrate is washed with water and allowed to air dry before being characterized.

Self-replicating AgNPs were also grown on hedgehog particles (HPs) made of iron oxide (Fe_2O_3) cores and zinc oxide (ZnO) spikes. These hedgehog particles were synthesized and provided by Dr. Elizabeth Wilson from our lab. [11] AgNPs were grown on the ZnO/Fe_2O_3 HPs by dispersing them in the self-replicating solution at the 60 min mark of the synthesis and stirred for 30 min while still under illumination with UV light. Additionally, HPs were dried on an indium tin oxide (ITO) coated coverslip. The substrate is supported on the surface of the solution at the 60 min mark to allow only growth on the submerged side and to prevent any attenuation effects that might occur if the substrate was completely submerged. After 30 min, the substrate is then removed from the surface of the solution, washed with water, and allowed to air dry before being characterized.

2.2.4 Electroless Metal Deposition

In **Chapter 5**, self-replicating networks on the substrates from **Section 2.3.3** were grown further using electroless metal deposition. Electroless deposition was first developed by Bernhard

Tollens, when he discovered the Tollen's reagent, $Ag(NH_3)_2OH$.[12] As this reagent has a short shell life, it is synthesized by first mixing an aqueous solution of silver nitrate with sodium hydroxide, which forms silver(I) oxide (**Equation 2.1**). Aqueous ammonia is then added to the solution to dissolve the silver(I) oxide to form the Tollen's reagent (**Equation 2.2**).

$$2AgNO_3 + 2NaOH \rightarrow Ag_2O(s) + 2NaNO_3 + H_2O \quad (2.1)$$

$$Ag_2O(s) + 4NH_3 + 2NaOH + H_2O \rightarrow 2[Ag(NH_3)_2]OH + 2NaOH \quad (2.2)$$

The Tollen's reagent can then be mixed with glucose, where the reagent oxidizes the glucose and is reduced to elemental silver and ammonia (**Equation 2.3**). This elemental silver will deposit onto the surface of the container it is in to create a reflective surface. This process has been used to make silver mirrors and is a silver mirror reaction.

$$2[Ag(NH_3)_2]^+ + C_6H_{12}O_6 + H_2O \rightarrow 2Ag(s) + 4NH_3 + C_6H_{12}O_7 + 2H^+ \quad (2.3)$$

The Tollen's reagent leads to silver deposition on the surface of the entire container it is in, but for our experiments, we desire silver deposition only on metals currently on the surface. As a result, we utilized a modified version of the reagent.

The deposition solution is based off a Tollen's reagent, which consists of two solutions.[13] The first solution consists of 20mM $AgNO_3$, 8.8 mL isopropanol, 1.2 mL acetic acid, and 40 mL 25% ammonia solution. The second solution consist of 0.5 mL hydrazine and 49.5 mL isopropanol. 7.5 mL of each solution is added to 15 mL of water while stirring to create the Tollen's reagent. Due to the short shelf life of the reagent, it must be prepared fresh each day it is used. The desired substrate is submerged in the deposition solution for 5 to 40 min depending on the desired amount of silver to be deposited. The substrate is then removed from the solution, washed 3 times in water, and allowed to air dry before any characterization.

2.2.5 Circularly Polarized Light Chiral Nanoparticle Synthesis

In **Chapter 5**, circularly polarized light (CPL) was used to synthesize chiral silver nanoparticles both in solution and on surfaces, as well as chiral Ag/Cu alloyed nanoparticles. CPL is a polarized electromagnetic wave whose electromagnetic field is rotating at a constant rate perpendicular to the direction of propagation. This can be visually portrayed as a helix when traveling through space. CPL can also be rotated clockwise or counter-clockwise, leading to oppositely rotating CPL, which they are commonly referred to as right and left CPL (R-CPL and L-CPL, respectively). Lasers are typically used for CPL, where the incident light is first passed through a linear polarizer, which allows only one state of linear polarized light to pass through while the rest is either absorbed or reflected. The two most common linear polarization states are p-polarized, which has an electric field parallel to the plane of incidence, and s-polarized, whose electric field is perpendicular to the plane of incidence. The linear polarized light is then passed through a quarter-wave plate that is at a 45^0 angle to the linear polarized light. The quarter-wave plate has both a fast and slow axis, which have a phase difference of 90^0. This phase difference when at a 45^0 angle to the incident linearly polarized light leads to equal polarization of both axes and results in the output of CPL (**Figure 2.2**).[14] Rotating the quarter-wave plate 90^0 will lead to the opposite CPL handedness.

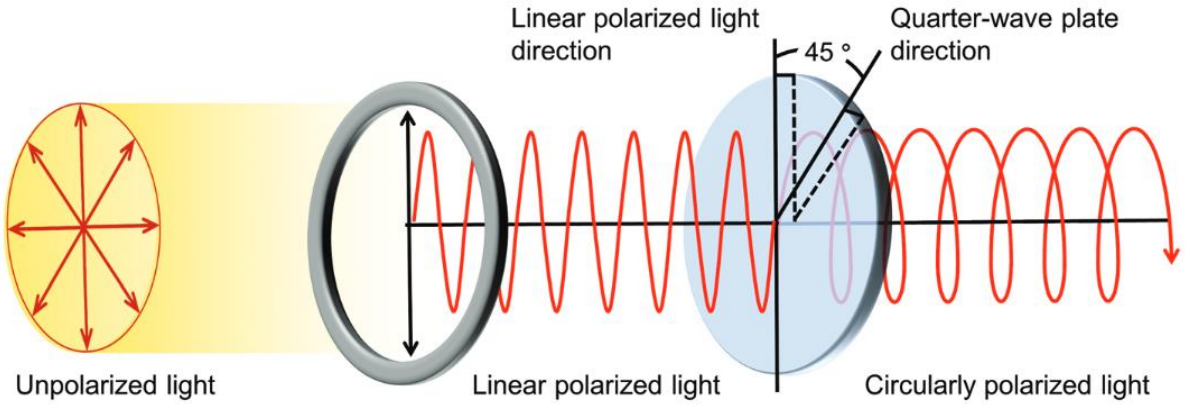

Figure 2.2. Schematics of converting unpolarized light to linearly polarized light and finally to CPL. Figure adapted from Ref.[14]

A diode-pumped continuous wave laser (CrystaLaser) at a wavelength of 405 nm was used for the synthesis of both chiral Ag and Ag/Cu nanoparticles. The laser is passed through a linear polarizer and quarter-wave plate at 45° to produce CPL. The quarter-wave plate is rotated 90° relative to the previous angle to change the handedness of light. The CPL is also passed through a concave and convex lens to broaden the beam to a diameter of 1 cm to illuminate the entire solution. Aqueous 3 mM citrate solutions with varying concentrations of $AgNO_3$ and copper nitrate ($Cu(NO_3)_2$) are placed beneath the laser in a thin 5 mL vial to allow full illumination of the solution. Solutions are left under illumination for varying times up to 18 hrs depending on which system is being tested.

To synthesize silver helicoids on surfaces, the desired substrate (either glass, ITO/glass, polydimethylsiloxane (PDMS), or silicon) was submerged in a solution of silver precursor (AgNO3, 2.5 mM) and citrate (12.5 mM), while the height from substrate to surface of the solution was fixed at 3 cm. Three diode-pumped continuous wave lasers (CrystaLaser) at three different wavelengths, 405, 532, and 660 nm, were used for the synthesis the chiral silver helicoids on surfaces. The laser emissions were broadened into spots with a diameter of 1-2 cm using a

combination of Plano-concave and -convex lenses. The lasers were modulated with a linear polarizer and a quarter-wave plate to emit either left- or right-circularly polarized light (L-CPL and R-CPL, respectively). The lasers were directed perpendicular to the substrate with varying power density for different times up to 30 minutes depending on purpose of experiments. The patterned substrates were washed three times with water before optical or imaging analysis.

2.3 Material Characterization Techniques

In the following subsections, all characterization techniques used in each subsequent chapter is detailed.

2.3.1 Ultraviolet-Visible Spectroscopy

UV-Vis spectroscopy is used to obtain the extinction spectra of materials in solution by measuring the amount of light that is transmitted through the solution. In a UV-Vis spectrophotometer, the amount of light transmitted through the sample, is measured to obtain the extinction spectrum, which encompasses absorption and scattering. The calculation of the extinction, or absorbance, at each wavelength can be seen here:

$$A = log_{10}\left(\frac{I_0}{I}\right) \tag{2.4}$$

Here, A is the absorbance, or extinction, I_0 is the intensity of the incident light at a specific wavelength, and I is the intensity of the transmitted light at the same wavelength.

The materials used in this thesis are plasmonic nanoparticles. Plasmonic nanoparticles strongly absorb and scattering light typically in the UV to the near-infrared (IR) regions of the electromagnetic spectrum depending on their size and shape. For example, spherical gold nanoparticles in aqueous solution have an observable red color due to strong absorption and scattering in the green/yellow region (500 nm - 600 nm). Whereas spherical silver nanoparticles

in aqueous solution have an observable yellow color due to absorption and scatting in the violet/blue region (400 – 500 nm). As mentioned in **Chapter 2**, this is because conduction electrons in these metallic nanoparticles, when excited with the correct wavelength of light, undergo a collective oscillation leading to unusually strong absorption. This collective oscillation is known as a localized surface plasmon resonance (LSPR). As a result, the optical activity of the nanoparticles can be directly measured using UV-Vis spectroscopy.

Not only can UV-Vis spectroscopy be used to evaluate optical activity changes over time, but it can also be used as a rough estimate for the concentration of NPs in solution.[15] This is achieved using the Beer-Lambert Law shown here:

$$A = \varepsilon c \ell \tag{2.5}$$

Here, ε is the extinction coefficient of the material, c is the concentration of the material, and ℓ is the path length of the cell. For all experiments in this thesis, the path length is 1 cm. Once the absorption is measured, you can use this formula to directly calculate the concentration of the sample. Calculating concentration of plasmonic nanoparticles from absorbance is reliable when the nanoparticles are monodisperse and not changing in size and shape. For the systems in **Chapters 3** and **4**, we are evaluating the plasmonic peak of our silver nanoparticles as they nucleate and grow. So throughout the synthesis, the nanoparticles are growing in size and therefore the average nanoparticle size is increasing over time. As a result, for our systems, using Beer-Lambert Law for calculating nanoparticle concentration can only be used as a rough initial estimate without knowledge of the average size at every stage of the synthesis. This issue arises from the extinction coefficient (ε) which is a function of nanoparticle size,making the correlation not entirely linear.[15]

For the work in **Chapters 3** and **4**, the extinction spectra of silver nanoparticles were measured using an Agilent 8453 UV-Vis spectrometer at various times through the synthesis. 530μL aliquots of sample were taken from the solution at varying time points (e.g., every 10, 15, or 30 min) and deposited into a micro spectrophotometer cell (Starna Cells) for analysis. The plasmonic peak of the AgNPs measured from 400 to 420 nm during the synthesis, with a Gaussian distribution roughly between 325 nm and 500 nm, was further used for the analysis.

2.3.2 Nanoparticle Tacking Analysis

Nanoparticle tracking analysis (NTA) is a technique used to analyze particles down to the nanometer scale. It uses a combination of the light scattering and Brownian motion of the nanoparticles to obtain size distribution and concentration. A laser beam is used to shine through a microfluidic channel of a diluted nanoparticle solution, where the beam is scattered by the particles into a charged-coupled device (CCD) digital camera. This allows a visualization of the nanoparticles under Brownian motion over multiple frames. The NTA software takes the motion of all nanoparticles, and using the Stokes Einstein equation (**Equation 2.6**), calculates the hydrodynamic diameter distribution.

$$D = \frac{k_B T}{3\pi\eta d} \tag{2.6}$$

Where D is the diffusion constant, k_B is Boltzmann's constant, T is the temperature, η is viscosity, and d is the diameter of the particle. Once the diffusion constant is calculated from the Brownian motion of the particle, the diameter of each individual nanoparticle can be found. The software also tracks all nanoparticles that flow through the viewing window for a fixed time to provide a total concentration as well. This technique can be used for nanoparticles all the way down to 10 nm depending on the refractive index of the particles and the wavelength of light

used.[16] Such examples of particles that can be seen down to 10 nm are silver and gold nanoparticles.

In **Chapter 4**, the concentration of nanoparticles was measured using a Malvern Nanosight NS300 and NTA. For NTA, a 405 nm laser module was used to track the number of silver nanoparticles as this module allows for the lowest size detection. The 405 nm laser is within the absorbance range of the AgNPs and as a result, will lead to some new AgNP nucleation when viewing the solution under the laser module. To counteract the unintended nucleation, 0.1 mM sodium chloride (NaCl) was mixed in the aliquot of sample to prevent further formation of AgNPs during analysis. Any unreacted Ag ions in the solution also reacted with NaCl and precipitated as silver chloride (AgCl).[17] The solution was centrifuged at 2,500 rpm for 10 minutes in an Eppendorf 5417R to separate out the larger AgCl particles from the sample. UV-Vis spectroscopy was used to ensure that the AgNPs remained stable in the solution with NaCl. It was discovered that the spectra do not change, which indicates that the AgNPs remained stable in the solution with NaCl. NTA was ran 5 times to get an accurate concentration and error.

2.3.3 Dark-Field Microscopy

Dark-field microscopy is a technique used in optical microscopy. A dark-field condenser lens is used on an optical microscope, which directs light away from the objective lens. As light passes through the sample, any light scattered will be captured by the objective lens, while the light that directly transmitted through the sample will not (**Figure 2.3**).[19] Typically, an oil-immersion objective lens with a numerical aperature (NA) greater than 1 must be used along with an objective lens that has a NA less than 1 to increase the scattered light that can be captured by the objective lens. This results in an image with a dark background and bright particles that provides better contrast between the background and sample, and therefore better signal-to-noise.

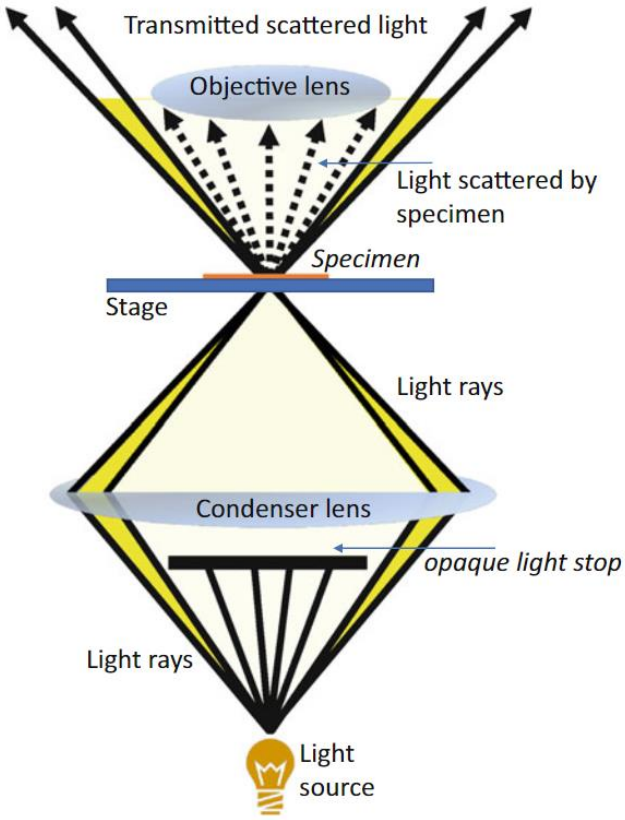

Figure 2.3. Schematic of dark-field microscopy. A condenser lens allows no light to directly be transmitted to the objective lens. The only light that reaches the objective lens is that which is scattered by the sample. Figure adapted from Ref.[19]

In **Chapter 4**, dark-field microscopy was performed using an Olympus IX81 inverted microscope equipped with an Olympus U-DCW dark-field oil-immersion objective (NA 1.2-1.4). The scattered light was captured through a 60x dry objective (NA 0.9, Olympus) and imaged through an EMCCD camera (Andor IXon Ultra). The solution was imaged between a glass slide and a cover slip with cover slip spacers to allow a small gap to fill up with the unreacted self-replicating solution. The solution was sealed using bee wax to ensure no evaporation leading to false Brownian motion and unwanted flow under imaging. The 8W 365nm UV light was illuminated on the sample during the imaging to allow synthesis of the AgNPs while imaging.

2.3.4 Transmission Electron Microscopy

TEM uses an accelerated beam of electrons to observe materials down to the atomic scale. The electrons are transmitted through the material, where an image is formed as the electrons interact with the sample via elastic and inelastic scattering. To obtain resolutions down to the atomic scale, the sample must be extremely thin, between 5 nm and 500 nm, as too thick leads to lower resolution.[18] These atomic resolutions are also possible due to the small de Broglie wavelength of electrons, as compared to that of light microscopy. TEM is typically operated in vacuum at voltages between 40 and 300 keV by using high speed electromagnetic coils to produce the accelerated electron beam. The beam passes through a series of condenser lenses that focus the beam down to the desired size before it passes through the sample. The transmitted beam is then focused by an objective lens, as well as intermediate and projector lenses for magnification, before being captured either on a phosphor screen or a CCD camera.

In **Chapter 3 – 5**, TEM imaging was performed on a Thermo Fisher Talos F200X G2 scanning transmission electron microscope (S/TEM) with a 200 kV accelerating voltage. Typical TEM samples were prepared by drop casting 4μL of solution on a 400-mesh copper grid with an ultrathin carbon film on lacey carbon support film (Ted Pella) after centrifuging the solution at 12,500 rpm for 30 minutes to remove unreacted Ag ions and residual citrate and washed with ultrapure water. The TEM sample was allowed to air dry over night before being imaged.

2.3.5 Cryogenic Transmission Electron Microscopy

Cryogenic transmission electron microscopy (Cryo-TEM) is an advanced technique used in electron microscopy for samples that are not stable outside of solution or deteriorate under the electron beam, such as biological specimens.[20] In Cryo-TEM, the sample is brought to cryogenic temperatures to preserve the structure in vitreous ice and maintain stability when brought under

vacuum in the microscope. Vitreous ice in an amorphous form of ice that has improved resolution as compared to crystalline ice when viewed under an electron microscope. Samples are prepared by dropping a small volume of aqueous solution onto a typical TEM grid followed by blotting to create a uniform thickness. The grid is immediately plunged into liquid ethane to vitrify the solution and then plunged into liquid nitrogen to obtain cryogenic temperatures. The sample is maintained at cryogenic temperatures throughout the entire imaging under the electron microscope to avoid heating of the sample. Not only is Cryo-TEM useful for biological specimens, but it is useful for colloidal systems to capture how particles interact in solution by arresting them in a 3D environment instead of on a 2D surface.[21] It also avoids any drying effects commonly seen when drying samples on TEM grids.

In **Chapter 4**, Cryo-TEM was performed on a Thermo Fisher Talos F200X G2 scanning transmission electron microscope (S/TEM) with a 200 kV accelerating voltage. An aliquot of the reaction solution was taken at the inflection point (60 min) of the synthesis where the most self-replication is occurring. The solution was immediately drop-casted on a TEM grid and blotted using filter paper to create a thin enough liquid layer for viewing under TEM. The grid was then instantly vitrified by submerging it in liquid ethane followed by submerging the grid in liquid nitrogen. The frozen TEM grid was setup in a Gatan Elsa cryo-transfer holder that is specialized for cryo-TEM and imaged.

2.3.6 In-Situ Liquid Transmission Electron Microscopy

Liquid-phase transmission electron microscopy (Liquid TEM) is another advanced technique used in electron microscopy for viewing samples in their native liquid environments. This technique is extremely useful for observing the nucleation and growth of nanoparticles in solution.[22] Additionally, specialty liquid chips can be purchased that allow in situ analysis of

temperature-controlled[23] and electrochemical systems[24]. As electron microscopy is performed under vacuum, the solution must be encased in a cell that can both maintain integrity under vacuum and be thin enough to allow transmission of the electron beam. The most typical liquid cell consists of two silicon chips with narrow silicon nitride (SiN) windows that are each 30 to 50 nm thick. The windows are separated by spacers that are 100 nm to 2 μm thick to allow a certain volume of liquid to be enclosed depending on the size of the material (**Figure 2.4**). When the liquid cell is placed in a TEM, the vacuum causes the cell windows to bow outward due to the pressure difference, which increases the thickness of the solution, up to 1 μm at the center of the window, that the electron beam must travel through, leading to lower resolution.[25] To combat this, most liquid TEM samples are viewed near the edges and corners of the windows were bowing is minimal.

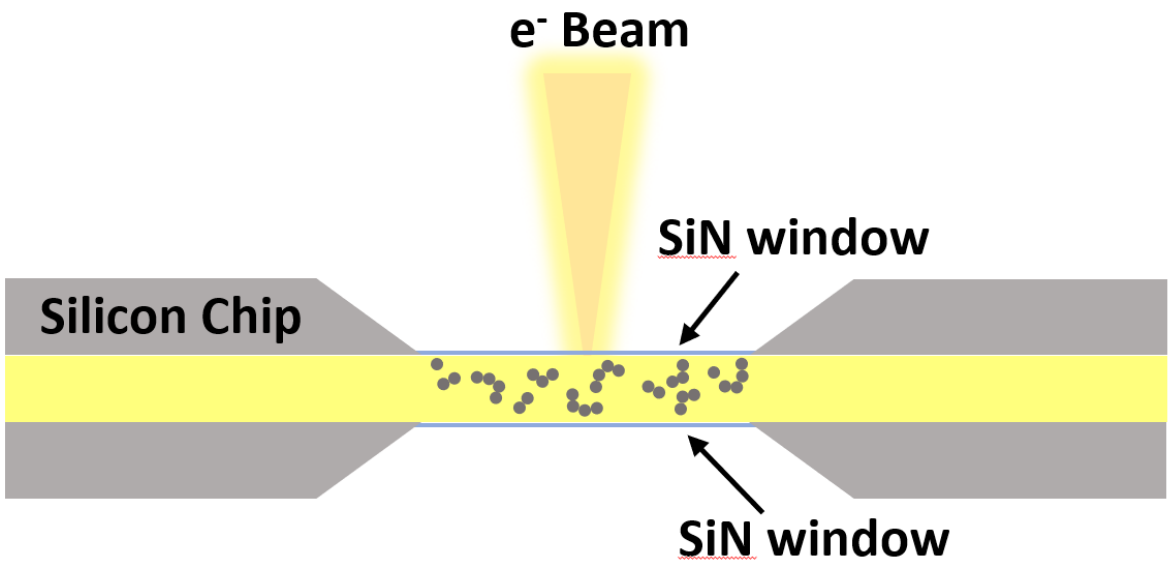

Figure 2.4. Setup of a typical SiN window liquid TEM cell for viewing the nucleation and growth of NPs.

The solution contained within the cell is so small that Brownian motion is minimal and many particles with attach to the windows, leading to most Liquid TEM being imaged on the

windows When viewing the growth of materials, one can record at either the top or bottom window. Viewing at the top window has lower resolution due to beam broadening as the beam must pass through the rest of the solution before imaging, which the bottom window does not. For example, gold nanoparticles in a 1 μm thick solution would be expected to have a resolution of roughly 9.8 nm at the top window versus 3 nm resolution at the bottom window.[26]

In **Chapter 4,** Liquid TEM was performed on a Thermo Fisher Talos F200X G2 scanning transmission electron microscope (S/TEM) with a 200 kV accelerating voltage. A viewing cell (Hummingbird Scientific) consisting of two silicon chips with transparent silicon nitride windows separated by a 100 nm spacer were used. The viewing cell chips were plasma cleaned to create a hydrophilic surface for better flow and dispersion of the solution in the holder. A liquid cell TEM holder (Hummingbird Scientific) was assembled with the silicon chips and placed in a pumping station (Hummingbird Scientific) to ensure that the holder maintains its integrity under vacuum before being placed in the TEM. The self-replicating solution was pumped through the holder, and the liquid cell holder was placed in the TEM equipment and aligned to view the sample. Electron dose rate is kept at or below 130 e^-/Ås to allow for self-replication without other species forming. To view the nuclei forming at the interface of parent NPs, the electron dose rate was increased above 200 e^-/Ås to destabilize the nuclei to view them.

2.3.7 Scanning Electron Microscopy

Scanning electron microscopy (SEM) is a technique that uses a focused beam of electrons to scan the surface of a sample to obtain images from the nanometer to micrometer scale. SEM typically uses an accelerating voltage ranging from 0.2 to 40 keV produced from electromagnetic coils. The electron beam passes through tuneable apertures and lenses to focus the beam where it

then scans over the surface in a raster scan pattern. As the beam scans, the interaction between the electrons and the sample produces secondary electrons and backscattered electrons.

Secondary electrons originate from inelastic interactions between the electron beam and the surface atoms of the samples. Their low penetration depth and low kinetic energy help provide high quality topographic images.[27] Backscattered electrons on the other hand result from high energy elastic collisions of the electrons with the atoms. Backscattered electrons penetration depth is much larger than secondary electrons that results in lower resolution, but higher sensitivity to the atomic number. As a result, the brightness of the image is directly proportional to the atomic number of the sample, which can provide valuable insight into the composition.[27]

In **Chapters 4 and 5**, Scanning electron microscopy (SEM) images were taken using a Thermo Fisher Helios 650 Nanolab at 3 kV accelerating voltage and 0.1 nA beam current. Samples were in most cases were prepared on silicon wafer substrates by either drop casting a solution and letting it dry or growing the sample directly on the substrate. The substrates were attached to a metallic pin stub with conductive carbon tape for viewing in the SEM.

2.3.8 Energy Dispersive X-Ray Spectroscopy

Energy dispersive X-ray spectroscopy (EDS) is a technique commonly used with SEM, TEM, or scanning transmission electron microscopy (STEM). EDS uses X-rays that are produced when the electron beam interacts with the sample. The incident electron causes an inner shell electron to jump to a higher energy level leaving behind a hole in the inner shell. An electron at a higher level fills in the hole, which emits an X-ray characteristic to that specific jump.[28] These X-rays have energies that are specific to the element that they were emitted from and are combined to create a spectrum that is useful to determine the exact atomic percent composition of the sample area being scanned. When using EDS, it is important not to use a substrate or TEM grid that

contains the elements of your sample as this can lead to skewed results in the composition. Additionally, EDS can be used to create an elemental mapping of sample area to provide a detailed visual distribution of elements as well. This is very useful for obtaining compositions of individual particles and changes across non-uniform materials.

In **Chapter 5**, EDS measurements taken using a a Thermo Fisher Talos F200X G2 scanning transmission electron microscope (S/TEM) with a 200 kV accelerating voltage. Sample areas were scanned until the EDS spectrum showed little to no change between scans. EDS mapping of elements on the imaged area were performed over multiple scans to ensure that the composition is correct and nicely saturated.

2.3.9 Dynamic Light Scattering

Dynamic light scattering (DLS) is a technique used to find size distribution and zeta potential for colloidal solutions. In DLS, a laser is directed through a solution containing suspended particles that scatter the light in all directions before it is collected by a photomultiplier and projected to create a speckle pattern. As the particles move due to Brownian motion, the pattern changes over time. The intensity changes are analyzed by the software with an autocorrelator to produce a size distribution. As DLS is a bulk analysis, if the sample is monodispersed, then you can obtain sizes down to 0.3 nm. If the sample is polydisperse, then the size is less accurate as larger particles have higher scattering and therefore DLS is biased towards these larger particles.[29] It should be noted that the size distribution is the hydrodynamic diameter instead of the actual diameter of the particle. Hydrodynamic diameter is essentially the diameter of the particle and any surfactants attached to the surface. This is due to the fact that as particles diffuse through the solution, there is additional drag due to the surfactants as well. As a result, the hydrodynamic diameter is typically larger than the actual size of the particle itself.

Zeta potential is another measurement that is very useful for colloidal solutions. The zeta potential is the electrical potential (typically mV) at the slipping plane of the electrical double layer (EDL). The EDL consists of a first layer of ions of a certain charge that are adsorbed to the surface of the particle. This first layer is commonly referred to as the Stern layer. A second layer is formed from ions that are attracted by coulomb forces to the surface charge. This second layer is loosely attached to the particle but moves with the particle as it diffuses. The end of this second layer is referred to as the slipping plane and this plane is where the zeta potential is measured. To measure zeta potential, an alternating potential is applied to the cell where the laser is shot through the solution to measure the bulk oscillation of the particle's movements. Although it does not provide the exact charge of the particle surface, it is primarily used as a measurement for how stable the particle are in solution. The larger the absolute value of the zeta-potential, the more stable the dispersion is.[30]

In **Chapter 4**, DLS was performed using a Malvern Zetasizer Nano ZSP. For size distribution, a disposable plastic cuvette is filled with 1 mL the colloidal solution and placed in the machine. Measurements are run for a minimum of 10 times until the software determine the results to be stable. For zeta potential, a specialized folded capillary zeta cuvette (Malvern) is used which has metal contacts for applying a potential. Like size distribution, a minimum of 10 measurements are performed until the software determines the results to be stable.

2.3.10 Four-Point Probe

A four-point probe is commonly used to measure the sheet resistance (Ω/□) of thin films. The probe accomplishes this by providing a current through two outer probes and reading the voltage across two inner probes. The probes are always spaced equally apart in a linear pattern for

easy comparison between samples and reproducibility. The current and voltage can be used to calculate the sheet resistance with **Equation 2.7**.

$$R_S = \frac{\pi}{\ln(2)} \frac{\Delta V}{I} = 4.53236 \frac{\Delta V}{I} \tag{2.7}$$

Here, R_S is the sheet resistance in Ω/□, V is voltage, and I is current. As the units of sheet resistance contains a dimensionless square (□), any thin film can be compared with sheet resistance regardless of the size of the film.[31] If the thickness of the film is known, then the resistivity of the film can be calculated from the sheet resistance.

In **Chapter 5**, a four-point probe (Signatone SP4) powered by a source meter (Keithley Model 2470) was used to measure the sheet resistance of our self-replicating silver nanoparticles grown on a surface after electroless metal deposition is performed. A current of 1 mA was applied and the voltage was measured. The sheet resistance was calculated using **Equation 2.7**.

2.3.11 Circular Dichroism Spectroscopy

Circular dichroism (CD) spectroscopy is technique used to characterize the chiroptical properties of chiral materials. CD spectroscopy measures the difference in absorption between left- and right-handed circularly polarized light (L-CPL and R-CPL, respectively). Any optically active chiral material will absorb either L-CPL or R-CPL more depending on their own handedness due to differing indices of refraction for both polarized CPL. This differing refractive index leads to L-CPL and R-CPL passing through the sample at different speeds causing optical rotation, or circular birefringence. CD measurements are commonly measured in ellipticity (θ) and has the units, millidegrees (mdeg), which is related to the difference in absorbance of CPL by **Equation 2.8**.

$$\theta(mdeg) = 32980 \Delta Abs \tag{2.8}$$

Another characteristic of chiral materials that can be derived from CD spectroscopy is the anisotropy (g) factor. The g-factor is a dimensionless unit used to compare the chiroptical activity between different materials regardless of the concentration. It can be calculated using **Equation 2.9**:

$$g - factor = \frac{\theta(mdeg)}{32980 \times Abs} \tag{2.9}$$

In **Chapter 5**, CD spectroscopy was performed for all colloidal system using a Jasco J-815 CD spectrometer with a detector range from 200-800 nm. The CD spectra were measured with the scanning parameters: high sensitivity, 100 nm/min scanning speed, 1 nm data pitch, 5 nm bandwidth, and 1 s digital integration time. For the silver chiral helical metasurfaces, either a Jasco J-815 or J-1700 CD sprectometer equipped with one PMT detector in the 200-800 nm range and two InGaAs near infrared (NIR) detectors for the 800-1600 nm and 1600-2500 nm range. The CD spectra were measured with the scanning parameters: 500 nm/min scanning speed, 1 nm data pitch, 5 nm bandwidth, and 0.25 s digital integration time.

2.4 References

1. J. Turkevich, P. C. Stevenson, J. Hillier, A Study of the Nucleation and Growth Processes in the Synthesis of Colloidal Gold. *Discuss Faraday Soc*. **11**, 55–75 (1951).

2. M. Grzelczak, L. M. Liz-Marzán, The relevance of light in the formation of colloidal metal nanoparticles. *Chem Soc Rev*. **43**, 2089–2097 (2014).

3. K. G. Stamplecoskie, J. C. Scaiano, Light Emitting Diode Irradiation can Control the Morphology and Optical Properties of Silver Nanoparticles. *J Am Chem Soc*. **132**, 1825–1827 (2010).

4. R. Sato-Berŕu, R. Redón, A. Vázquez-Olmos, J. M. Saniger, Silver nanoparticles synthesized by direct photoreduction of metal salts. Application in surface-enhanced Raman spectroscopy. *Journal of Raman Spectroscopy*. **40**, 376–380 (2009).

5. T. Bian, Z. Chu, R. Klajn, The Many Ways to Assemble Nanoparticles Using Light. *Advanced Materials*. **32**, 1–17 (2019).

6. J. Xi, Z. Wu, X. Teng, Y. Zhao, L. Chen, X. Qiu, Self-assembled polyelectrolyte multilayer modified Nafion membrane with suppressed vanadium ion crossover for vanadium redox flow batteries. *J Mater Chem*. **18**, 1232–1238 (2008).

7. Y. Wang, S. Wang, M. Xiao, D. Han, M. A. Hickner, Y. Meng, Layer-by-layer self-assembly of PDDA/PSS-SPFEK composite membrane with low vanadium permeability for vanadium redox flow battery. *RSC Adv*. **3**, 15467–15474 (2013).

8. J. Y. Kim, M. G. Han, M. bin Lien, S. Magonov, Y. Zhu, H. George, T. B. Norris, N. A. Kotov, Dipole-like electrostatic asymmetry of gold nanorods. *Sci Adv*. **4**, (2018).

9. J. Lee, J. Yang, S. G. Kwon, T. Hyeon, Nonclassical nucleation and growth of inorganic nanoparticles. *Nat Rev Mater*. **1**, 1–16 (2016).

10. R. Tang, B. Jin, B. Jin, Z. Liu, Recent Experimental Explorations of Non-Classical Nucleation. *CrystEngComm*. **22**, 4057–4073 (2020).

11. E. A. K. Wilson, Design and Application of Surface Corrugated Microparticles for Photocatalysis in Nonpolar Media. Thesis (2022). doi:10.7302/6159.

12. B. Tollens, Ueber ammon-alkalische Silberlösung als Reagens auf Aldehyd. *Berichte der deutschen chemischen Gesellschaft*. **15**, 1635–1639 (1882).

13. S. Schaefers, L. Rast, A. Stanishevsky, Electroless Silver Plating on Spin-Coated Silver Nanoparticle Seed Layers. *Mater Lett*. **60**, 706–709 (2006).

14. Y. Sang, J. Han, T. Zhao, P. Duan, M. Liu, Y. Sang, M. Liu, T. Zhao, P. Duan, J. Han, Circularly Polarized Luminescence in Nanoassemblies: Generation, Amplification, and Application. *Advanced Materials*. **32**, 1900110 (2020).

15. D. Paramelle, A. Sadovoy, S. Gorelik, P. Free, J. Hobley, D. G. Fernig, A rapid method to estimate the concentration of citrate capped silver nanoparticles from UV-visible light spectra. *Analyst*. **139**, 4855–4861 (2014).

16. R. Luque, M. Ojeda, A. Garcia, C. Lastres, R. Campos, A. Pineda, A. A. Romero, A. Yepez, Evaluation of biomass-derived stabilising agents for colloidal silver nanoparticles via nanoparticle tracking analysis (NTA). *RSC Adv*. **3**, 7119–7123 (2013).

17. A. Ingle, M. Rai, A. Gade, M. Bawaskar, Fusarium solani: A novel biological agent for the extracellular synthesis of silver nanoparticles. *Journal of Nanoparticle Research*. **11**, 2079–2085 (2009).

18. L. Reimer, *Transmission Electron Microscopy: Physics of Image Formation and Microanalysis*. (Springer, 2013).

19. R. M. Zucker, W. K. Boyes, Combination of Dark-Field and Confocal Microscopy for the Optical Detection of Silver and Titanium Nanoparticles in Mammalian Cells. *Methods in Molecular Biology*. **2118**, 395–414 (2020).

20. M. J. Costello, Cryo-Electron Microscopy of Biological Samples. *Ultrastructural Pathology* **30**, 361–371 (2009).

21. P. L. Stewart, Cryo-electron microscopy and cryo-electron tomography of nanoparticles. *Wiley Interdiscip Rev Nanomed Nanobiotechnol*. **9**, e1417 (2017).

22. J. J. de Yoreo, In-situ liquid phase TEM observations of nucleation and growth processes. *Progress in Crystal Growth and Characterization of Materials*. **62**, 69–88 (2016).

23. H. L. Xin, H. Zheng, In Situ Observation of Oscillatory Growth of Bismuth Nanoparticles. *Nano Letters* **12**, 1470-1474 (2012).

24. V. Subramanian, D. C. Martin, In Situ Observations of Nanofibril Nucleation and Growth during the Electrochemical Polymerization of Poly(3,4-ethylenedioxythiophene) Using Liquid-Phase Transmission Electron Microscopy. *Nano Lett*. **21**, 9077–9084 (2021).

25. M. E. Holtz, Y. Yu, J. Gao, H. D. Abruña, D. A. Muller, In Situ Electron Energy-Loss Spectroscopy in Liquids. *Microscopy and Microanalysis*. **19**, 1027–1035 (2013).

26. N. de Jonge, L. Houben, R. E. Dunin-Borkowski, F. M. Ross, Resolution and aberration correction in liquid cell transmission electron microscopy. *Nature Reviews Materials* **4**, 61–78 (2018).

27. W. Zhou, Z. L. Wang, Scanning microscopy for nanotechnology: Techniques and applications. *Scanning Microscopy for Nanotechnology: Techniques and Applications*, 1–522 (2007).

28. D. Shindo, T. Oikawa, "Energy dispersive X-ray spectroscopy" in *Analytical Electron Microscopy for Materials Science* vol. 51 81–102 (Springer, Tokyo, 2002).

29. D. R. Wilson, J. J. Green, "Nanoparticle Tracking Analysis for Determination of Hydrodynamic Diameter, Concentration, and Zeta-Potential of Polyplex Nanoparticles" in *Biomedical Nanotechnology* 31–46 (Humana Press Inc., 2017).

30. G. Midekessa, K. Godakumara, J. Ord, J. Viil, F. Lättekivi, K. Dissanayake, S. Kopanchuk, A. Rinken, A. Andronowska, S. Bhattacharjee, T. Rinken, A. Fazeli, Zeta Potential of Extracellular Vesicles: Toward Understanding the Attributes that Determine Colloidal Stability. *ACS Omega*. **5**, 16701–16710 (2020).

31. A. M. Lord, J. E. Evans, C. J. Barnett, J. K. Kim, Y. S. Choi, D. W. Lee, I. Miccoli, F. Edler, H. Pfnür, P. Pfnür, C. Tegenkamp, The 100th anniversary of the four-point probe technique: the role of probe geometries in isotropic and anisotropic systems. *Journal of Physics: Condensed Matter*. **27**, 223201 (2015).

Chapter 3 Finding A Self-Replicating System

3.1 Introduction

Self-replication is one of the key processes for the survival of all living things.[1,2] It has been extensively explored for minimalistic organic systems[3,4], but little work has been done to expand the field of self-replication into inorganic materials outside of theoretical modeling.[5] Inorganic systems would have numerous advantages over biological systems as they would be more robust, tunable, and simpler.[6,7]

In this chapter, we will explore various systems in the search for an inorganic nanoparticle system that shows self-replicating capabilities. As self-replicating kinetics to our knowledge have never been observed for inorganic nanoparticles, there is little to no literature to base this work from. As a result, a series of systematic screening steps were developed and utilized to comb through a large array of different systems. In the end, we were able to find one out of over a hundred combinations of chemicals that eventually showed self-replicating capabilities.

This chapter details all the research done into finding this inorganic system that exhibits self-replicating capabilities as it is important for future researchers who might delve into this topic to know what did and did not work. The primary objectives of this chapter are to: (1) develop a systematic series of steps for rapidly evaluating if a system shows potential self-replicating capabilities (**Section 3.3**), (2) find the candidate that will be evaluated more in-depth to determine if and how they self-replicate (**Section 3.4**). The most promising candidate will be detailed in **Section 3.5**.

3.2 Methods

3.2.1 Light Assisted Synthesis of Silver Nanoparticles

Silver nanoparticles (AgNPs) were synthesized through a photoinduced reaction with an 8 W 365 nm ultraviolet (UV) portable lamp (Analytik Jena). Varying concentrations of silver nitrate ($AgNO_3$) were used as the AgNP precursor for all systems. Varying reducing agents and stabilizers were added to the solution in a variety of concentrations. The solution was placed in an ice bath and dark environment to maintain a constant temperature of 3-5°C throughout the synthesis while eliminating any thermodynamic effects caused by heating from the light source and to eliminate ambient light effects, respectively. During the reaction, the solution is illuminated with the UV lamp for up to 9 hours while constantly agitated with a stir bar. Aliquots of the solution were taken at various time points during the synthesis and characterised immediately under ultraviolet-visible (UV-Vis) spectroscopy to ensure AgNPs are forming. For experiments with the 8 W lamp, light intensity at the solution was 1.3 mW/cm^2.

3.2.2 Measurements of Nanoparticle Concentration Over Time

For preliminary screening, an Agilent 8453 UV-Vis spectrometer was used to analyse the extinction spectrum of the AgNP solutions at various times through the synthesis. 530µL aliquots of sample were taken from the solution at varying time points (e.g., every 10, 15, or 30 min) and deposited into a micro spectrophotometer cell (Starna Cells) for analysis. The plasmonic peak of the AgNPs was measured, which ranges from 400 to 430 nm depending on the size of particles that each system makes.

3.2.3 TEM Imaging of Silver Nanoparticles

Transmission electron microscopy (TEM) imaging was performed on a Thermo Fisher Talos F200X G2 scanning transmission electron microscope (S/TEM) with a 200 kV accelerating voltage. TEM samples were prepared by drop casting 4μL of solution on a 400 mesh copper grid with an ultrathin carbon film on lacey carbon cupport film (Ted Pella, Cat.# 01824) after centrifuging the solution at 12,500 rpm for 30 minutes to remove residual chemicals and washed with ultrapure water. The TEM sample was allowed to air dry over night before being imaged.

3.3 Systems to Explore for Self-Replication

As a self-replicating system for inorganic nanoparticles that has never been seen to this date, there are no previous findings to work from for developing this system. As a result, finding the system will require exploration into numerous systems, but thoroughly analyzing every system for self-replicating capabilities would require years of studies and thus would not be feasible timewise. To solve this, a series of high-throughput screening steps were developed to explore these systems in a more systematic and efficient way.

To start, a few constants were required to reduce the number of variables being changed. The inorganic nanoparticles tested were AgNPs and the precursor for this system was silver nitrate ($AgNO_3$). The energy source for the nucleation and growth of these particles is UV light, and more specifically 365 nm light. Light as the energy source was chosen to take advantage of the unique plasmonic characteristics of AgNPs. An aqueous solution of $AgNO_3$ alone under UV light leads to no NP formation, so a reducing agent and stabilizer are required for the formation of the NPs. As mentioned in **Chapter 1**, a reducing agent is a reactant that donates an electron to an oxidizing agent. In this case, it is a chemical species that reduces silver ions (Ag^+) to silver atoms (Ag^0) to nucleate and grow the AgNPs. A stabilizer is a chemical that helps stabilize and maintain the shape

the AgNPs as they begin to nucleate and grow. A stabilizer is required as the AgNPs would aggregate and precipitate out of solution instead of remaining dispersed in solution. Only electrostatic stabilizers were tested here as large polymeric steric stabilizers, such as polyvinylpyrrolidone (PVP) and polyvinyl alcohol (PVA), would adsorb too strongly to the surface of the silver nanoparticles and prevent any chance of nucleation near the interface of another particle. Therefore, the variables that will be altered in this chapter are reducing agent, stabilizer, and the concentration/ratios of each.

With these variables defined, the literature was combed through to find any reducing agents and stabilizers that might be active for plasmonic nanoparticle synthesis only when under light illumination. The set of possible systems tested are seen in **Figure 3.1**. Sodium citrate dihydrate (citrate) was chosen as it is one of the most common reducing agent and stabilizer used for plasmonic nanoparticle synthesis.[8,9] Cetyl trimethylammonium bromide (CTAB) was tested as a stabilizer for the same reason as citrate. [10–12]

Various amino acids have been extensively used in a variety of nanoparticle syntheses either as a reducing agent or stabilizer.[13–16] They are popular due to their "green" nature and usefulness in biological systems.[14,15] Of the 10 amino acids tested, L-cysteine, and L-tryptophan are among the most commonly used for synthesis of plasmonic nanoparticles, such as silver and gold. [12,13,17,18] We would expect these two amino acids to have the most promise when synthesizing under light.

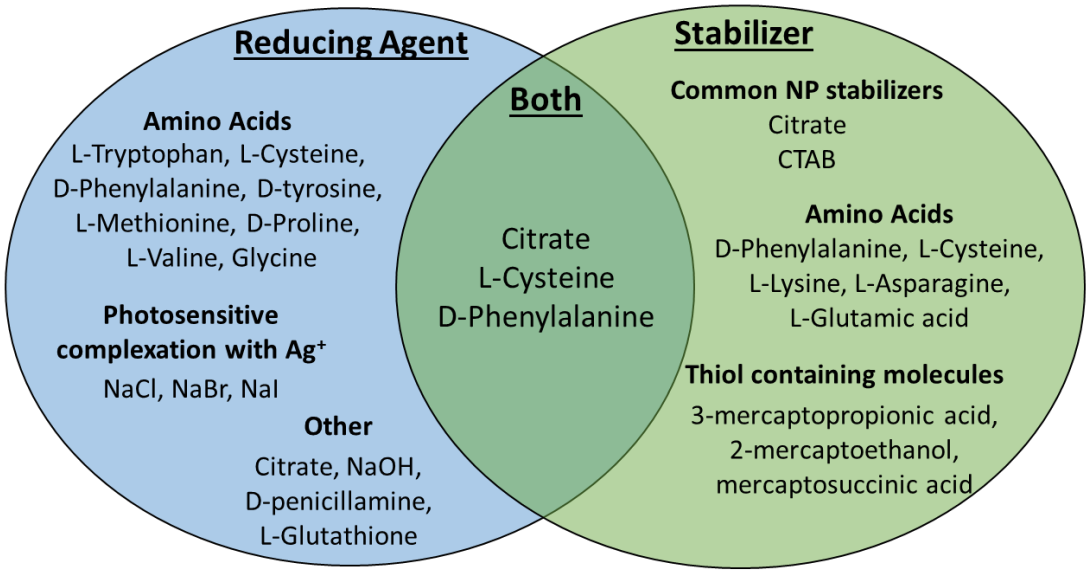

Figure 3.1. Venn diagram of combinations of reducing agents and stabilizers for testing for self-replication. All combinations consist of at least one reducing agent and one stabilizer. Species in the overlapping section have been used as both reducing agent and stabilizer in one system.

Various halides that form photosensitive complexes with silver ions were also tested as it is expected for them to have unique interactions when under UV light. Halides have been known to play a role in shape-selective synthesis of AgNPs as they will bind to specific sites leading to directed growth.[19,20] The three halides tested were sodium chloride (NaCl), sodium bromide (NaBr), and sodium iodide (NaI). A set of thiol containing molecules were also analyzed as stabilizers because thiols are known to bind strongly to silver, which will help stabilize the AgNPs.[21,22]

3.4 Screening Steps

From this set of systems, it can be seen that there are over one hundred systems to be analyzed. To screen through these systems, three chronological steps used are:

1) No precipitate or AgNP formation in the absence of light for 24 hours

2) UV-Vis spectroscopy for fast screening of systems in search for a rudimentary sigmoidal, or S-shape, curve in concentration over time.
3) Analyze NP size and shape of potential self-replicating systems using TEM

Showing results of every system is infeasible, so key examples of systems that failed at each step will be highlighted to help support the reasoning behind the design of this high-throughput screening.

3.4.1 Visual Observation

As one of our constant variables is light for the energy source, we wanted to ensure that each system does not lead to NP nucleation without light. The first step is the most simplistic one but helps to narrow done the set of systems significantly and efficiently. When mixing the solution, we want to visually observe a clear solution that remains clear a period up to 24 hours. So, if any precipitation or color change is observed, then that indicates that there is formation of undesired products or NP formation without light.

Examples can be seen in **Figure 3.2**, where the left most solution is desired as it has remained clear over the course of 24 hours (**Figure 3.2A**). This solution consists of 1 mM $AgNO_3$ with 3mM citrate as both the stabilizer and the reducing agent. The middle solution clearly has yellowish precipitation at the bottom of the vial (**Figure 3.2B**). This solution is comprised of 1 mM $AgNO_3$ with 2 mM L-tryptophan as the reducing agent and 0.5 mM L-cysteine as the stabilizer. The right most solution has a brownish color indicating that $AgNO_3$ is chemically reacting with the reducing agent (**Figure 3.2C**). This solution consisted of 1 mM $AgNO_3$ with 0.1 mM D-tyrosine and 0.1 mM CTAB as the reducing agent and stabilizer, respectively.

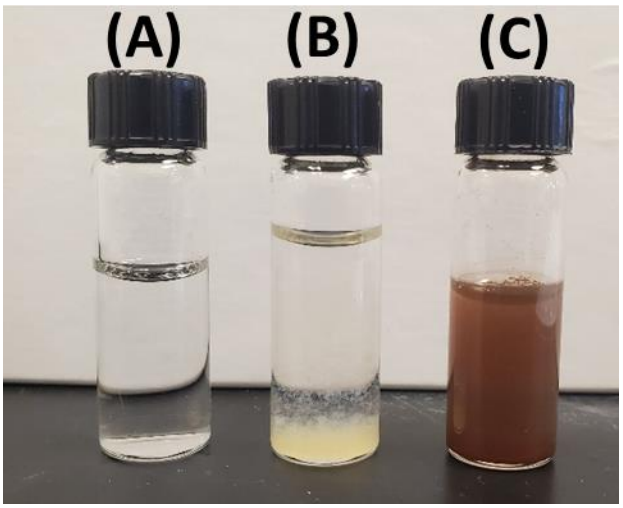

Figure 3.2. Examples of systems when left in the dark for 24 hours that passed the visual observation step (A), and failed due to precipitation (B) and chemical reduction of silver (C). (A) Consists of 1 mM $AgNO_3$ and 3 mM citrate. **(B)** Contains 1 mM $AgNO_3$, 2 mM L-tryptophan, and 0.5 mM L-cysteine. **(C)** Comprises of 1 mM $AgNO_3$, 0.1 mM L-Tyrosine, and 0.1 mM CTAB.

3.4.2 UV-Vis Spectroscopy

Any systems that remained clear over the course of 24 hours was then analyzed using UV-Vis spectroscopy. The plasmonic peak of silver nanoparticles can be found across most of the visible spectrum depending on the size and shape of the NPs. For example, spherical AgNPs can be found in the range of 400 nm to 420 nm when their size is below 20 nm in diameter. Based off Beer-Lambert's Law, the intensity of the plasmonic peak can be directly correlated to the concentration of AgNPs. So, UV-Vis spectroscopy can be used to quickly obtain a rough estimate of the concentration of AgNPs at any point during the synthesis. As this is a more simplistic system than that seen in the organic self-replicating systems, it is expected that this form of self-replication will lead to exponential growth as there are no inhibitors to affect the nucleation, which is seen for synthetic systems in **Chapter 1, Section 1.2.1**. Therefore, the second step is to look for an S-shape curve in concentration over time, which is characteristic for exponential growth.

For the S-shape curve, we expect to see an induction period of initial slow formation of new nanoparticles as they must homogeneously nucleate from the precursor in the solution. The next stage will be an exponential increase in rate of nucleation as the nanoparticles begin to self-catalyze their own formation. The final stage will be a reduction in nucleation as the precursor concentration is depleted. As particles would be expected to continue to grow over the course of the reaction, we would expect to see slights shifts in the wavelength at max intensity. As a result, when evaluating the kinetic curve, max intensity was plotted instead of the intensity at a fixed wavelength. We will explore next a system that did not lead to a sigmoidal growth curve but had some unique properties when altering the ratio of the constituents.

Concentration differences alone can alter the kinetics of silver nanoparticle synthesis. This can be seen for the system consisting of L-tryptophan as the reducing agent and CTAB as the stabilizer. $AgNO_3$ was maintained at a concentration of 0.5 mM for these experiments. UV-Vis measurements were taken every 3 min for a total of 30 min to get an overall trend. At a ratio of 1:1 $AgNO_3$ to L-trpytophan/CTAB, the extinction spectra have a peak around 400 nm, which is indicative of small spherical AgNPs, but there is an additional peak at 475 nm meaning that there are larger NPs present as well (**Figure 3.3A**). Plotting the intensity of the plasmonic peak at max wavelength, one can see that the intensity follows a linear trend (**Figure 3.3B**).

If we alter the ratio to 2:1 $AgNO_3$ to L-trpytophan/CTAB, we find that the kinetics of the synthesis completely change. The UV-Vis spectra for this ratio can be seen in **Figure 3.3C**, where the main plasmonic peak can be observed around 400 nm and an additional peak can be observed around 500 nm. This indicates that this solution also contains different sizes of AgNPs and is not monodisperse. At this ratio, the trend follows a logarithmic growth, where the intensity of the plasmonic peak rapidly increases for the first 5 min and then promptly declines over the rest of the

synthesis (**Figure 3.3D**). As a result, both systems do not give us the characteristic S-shape curve that we are looking for, but it provides valuable information on how the ratio of each component alone can significantly impact the kinetics to create completely different trends.

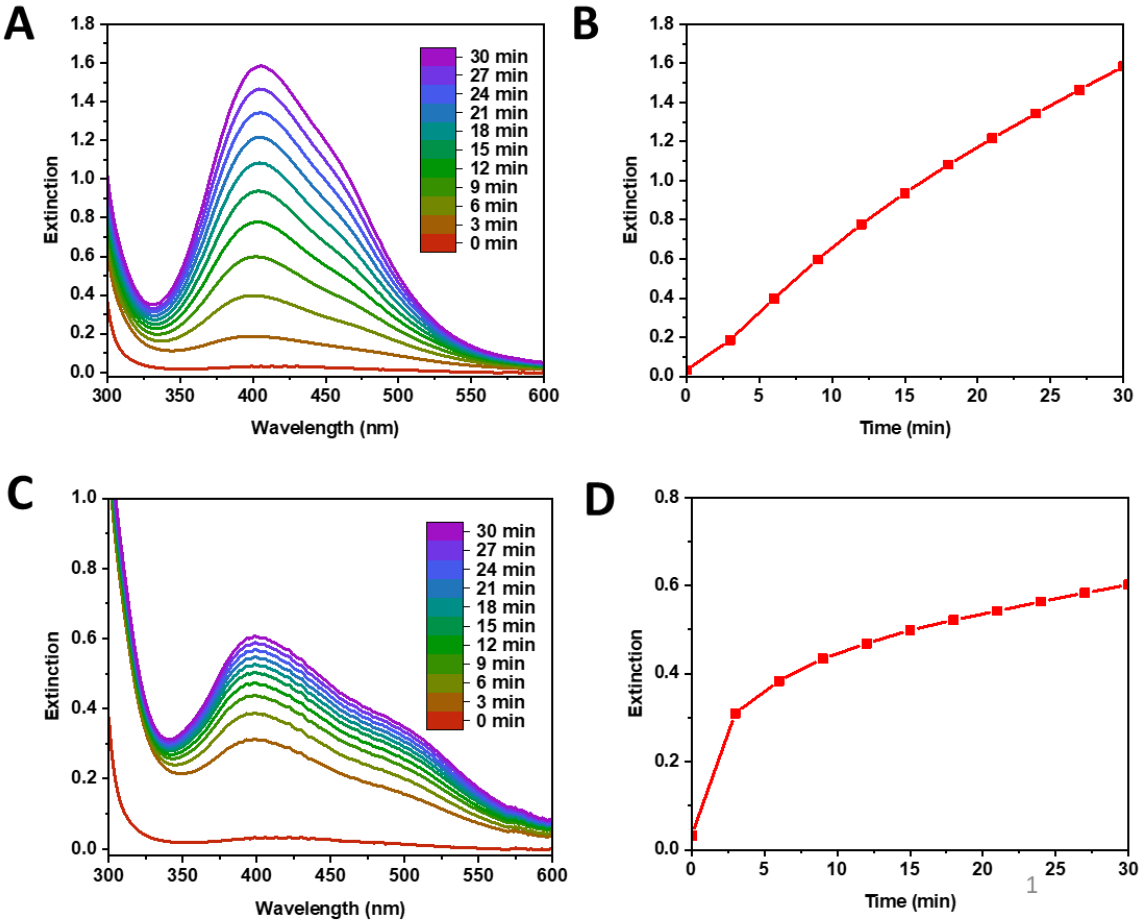

Figure 3.3. Extinction Spectra for 0.5 mM $AgNO_3$ with L-tryptophan and CTAB as reducing agent and stabilizer, respectively. (A) Extinction spectrum at 3 min intervals up to 30 min for 2:1 molar ratio $AgNO_3$ to L-Tryptophan/CTAB. **(B)** Plot of extinction intensity at max wavelength for 2:1 molar ratio. **(C)** Extinction spectrum at 3 min intervals up to 30 min for 1:1 molar ratio $AgNO_3$ to L-Tryptophan/CTAB. **(D)** Plot of extinction intensity at max wavelength for 1:1 molar ratio.

3.4.3 TEM Size and Shape Analysis

Any systems that showed s-shaped curves in concentration over time were then analyzed under TEM to view how the size and shape of the nanoparticles change through the course of the synthesis, since either factor can also impact both the intensity and wavelength of the plasmonic

peak. The molar extinction coefficient (ε) in Beer-Lambert's Law is a function of nanoparticle size, making the correlation between extinction and concentration nonlinear when particle size is changing. As a result, a sigmoidal curve in extinction intensity does not necessarily mean there will be a similar curve in actual concentration. To see the effect over time on the theoretical concentration, Beer-Lambert's Law was utilized to calculate the concentration to determine if it does indeed maintain its sigmoidal growth curve. The molar extinction coefficients were calculated for various sizes of spherical silver nanoparticles to convert absorbance to nanoparticle concentration (**Figure 3.4**).[23] We will detail next two systems that showed potential and eventually lead to the discovery of the most promising system.

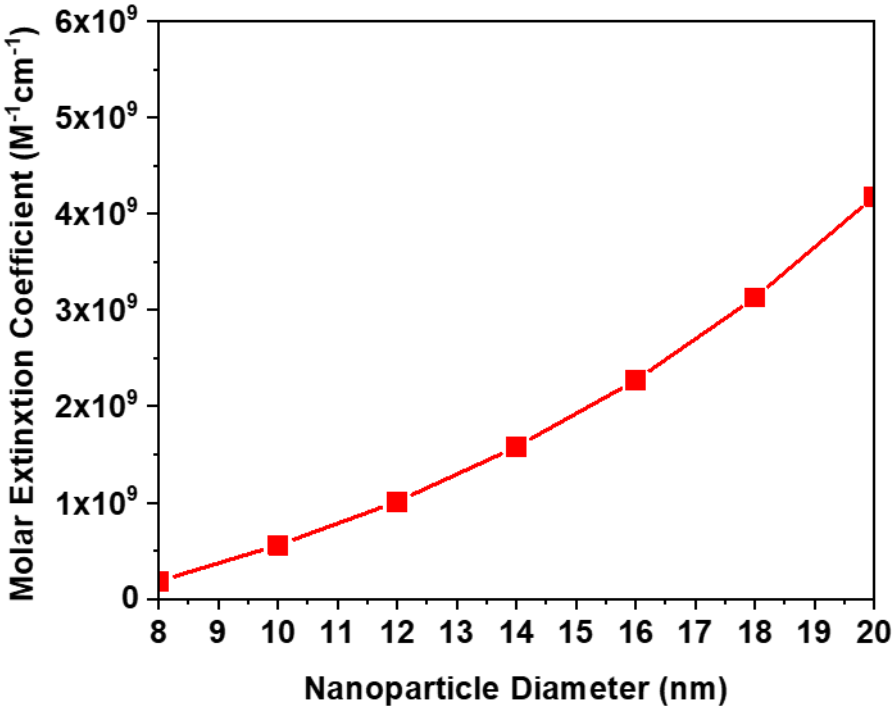

Figure 3.4. Molar extinction coefficient, ε, as a function of spherical silver nanoparticle size from 8 nm to 20 nm in diameter. Calculated from Ref.[23]

One system that should good initial results consisted of using L-cysteine as both the reducing agent and stabilizer. The solution consisted of 1 mM $AgNO_3$ and 1 mM L-cysteine and was illuminated up to 120 min. The UV-Vis spectra at varying time intervals up to 120 min can be

seen in **Figure 3.5A**, where the main plasmonic peak of the AgNPs can be found around 410 nm. Plotting the plasmonic peak intensity over time (**Figure 3.5B**), there is a small incubation period for the first 10 min where the concentration increases slowly, followed by a brief exponential increase in rate up to 20 min. After 20 min, the exponential growth tapers off into a more linear trend up to 90 min where we then see a slight decrease in rate to 120 min. As a result, we do not see that exponential increase in the rate of nucleation that we would hope for in an s-shape curve. But it does follow a more parabolic growth, which has been seen in synthetic templated self-replicating system. [24,25] The AgNPs were characterized under TEM at 120 min, and it was found that 3-7 nm AgNPs form, but they assemble into fibers (**Figure 3.5C, D**). It was concluded that the binding of the L-cysteine to the AgNPs was too strong and lead to precipitation of the fibers when not agitated but showed the potential for using the same chemical as both reducing agent and stabilizer.

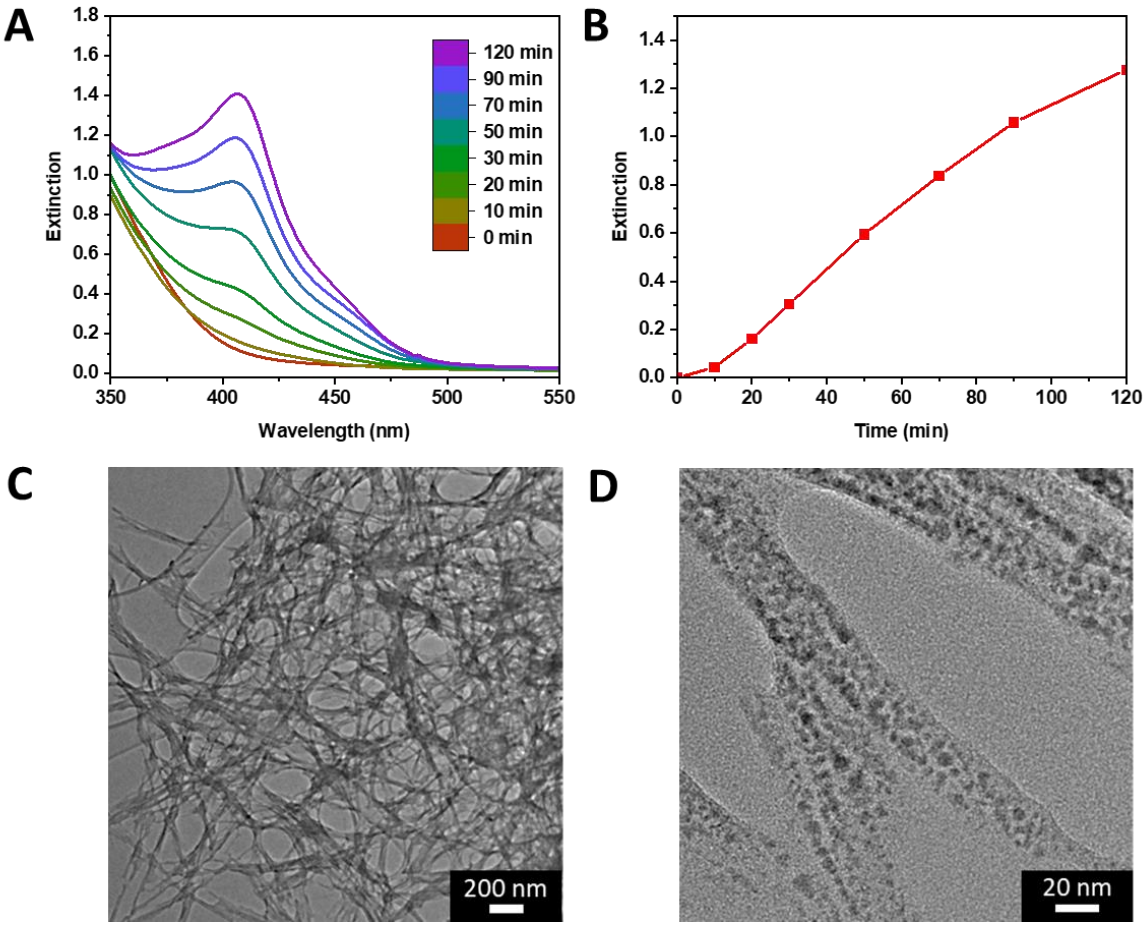

Figure 3.5. Silver nanoparticle synthesis from 1 mM $AgNO_3$ and 1 mM L-Cysteine as the reducing agent/stabilizer. (A) Extinction spectrum at varying time intervals up to 120 min. **(B)** Plot of extinction intensity at max wavelength from **A**. **(C)** TEM image of fiber-like assemblies of the AgNPs. **(D)** TEM image of one fiber assembly consisting of 3-7 nm AgNPs.

The next system that showed promise and eventually lead to the system with self-replicating capabilities consisted of citrate as both the reducing agent and stabilizer. The aqueous solution contained 1 mM $AgNO_3$ and 3 mM citrate. Aliquots of the solution were taken at 60 min intervals up to 540 min (**Figure 3.6A**), where the max wavelength for the plasmonic peak is observed around 420 nm. Plotting the intensity of the plasmonic peak (**Figure 3.6B**), the overall general trend follows a linear growth, but if the synthesis is observed more closely for the first 140 min (**Figure 3.6B, inset**), another kinetic trend is observed. There is a significant incubation period for the first 60 min followed by an exponential increase in rate of nucleation to 140 min. Although

it for the most part follows a linear trend, this is still a promising first step as can hopefully be fine-tuned to have exponential growth throughout the entire synthesis. Additionally, as discussed in the beginning of this section, the theoretical concentration could be different than that of the extinction intensity trend due to average NP size changes over the course of the synthesis.

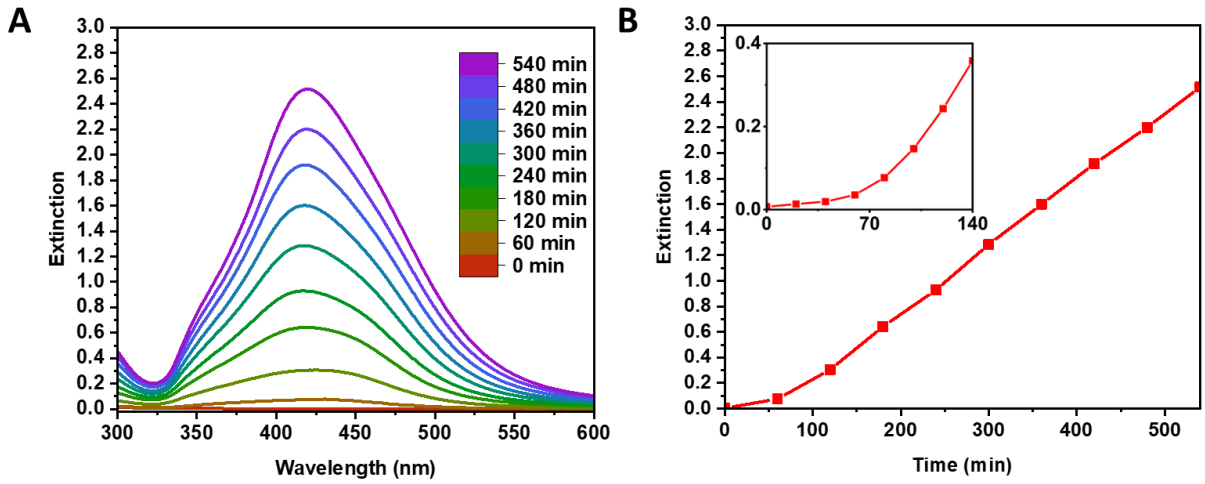

Figure 3.6. Silver nanoparticle synthesis from 1 mM $AgNO_3$ and 3 mM citrate as the reducing agent/stabilizer. (A) Extinction spectrum at 60 min time intervals up to 120 min. **(B)** Plot of extinction intensity at max wavelength from **A**. **(B, inset)** Plot of extinction intensity at max wavelength for the first 140 min taken every 20 min.

To test if there is any self-replication occurring in this system, we wanted to calculate a rough estimate of the actual AgNP concentration using the Beer-Lambert Law. With the extinction coefficients from **Figure 3.6**, all we need is the average diameter of the AgNPs throughout the synthesis. TEM images were taken at various time intervals (**Figure 3.7A-F**) and the diameter of over 200 AgNPs were measured. The plot of the diameter over time can be seen in **Figure 3.7G**, where the average diameter rapidly increases to 12.9 nm in the first 60 min and then continues to steadily increase in diameter for the rest of the synthesis up to 33.8 nm at 480 min. Converting extinction intensity to AgNP concentration using Beer-Lambert's Law (**Figure 3.7H**), we can see that the Theoretical AgNP concentration does not follow the same trend as the extinction intensity. The concentration follows a more logarithmic growth where the concentration is increasing rapidly

over the first 120 min and then begins to slow down and stop increasing altogether at 240 min and onwards. This indicates that the synthesis follows a burst nucleation instead of self-replication. Burst nucleation occurs when NPs rapidly nucleate at the same time when the solution becomes supersaturated and then nucleation significantly slows down and growth of the already formed NPs occurs.[26] This explains why the extinction intensity shows an initial incubation period where small AgNPs are nucleating, and the linear trend after that is the growth of the AgNPs as they get bigger in size. This increase in size leads to a larger extinction coefficient and thus a correlated increase in intensity. Although this system did not show self-replication characteristics in the end, it was further tuned and expanded upon to see if we could prevent supersaturation, and therefore burst nucleation. This will be further explored in **Section 3.5**.

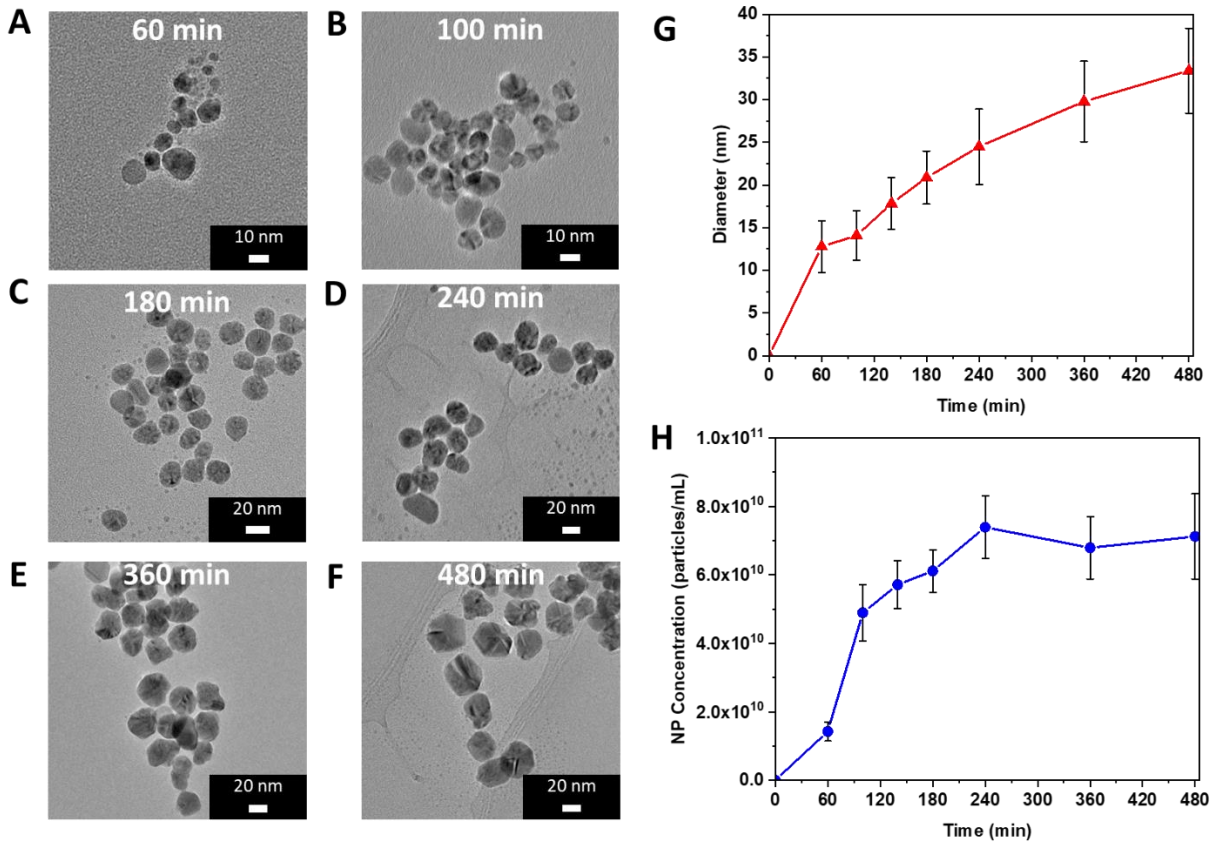

Figure 3.7. Analyzing particle changes over time. Sample TEM images of silver nanoparticles at synthesis times **(A)** 60 min, **(B)** 100 min, **(C)** 180 min, **(D)** 240 min, **(E)** 360 min, and **(F)** 480 min for 1 mM $AgNO_3$ and 3 mM citrate as the reducing agent/stabilizer. **(G)** Plot of average silver nanoparticle diameter in nm at each time point. Averages were taken from over 200 AgNP diameters **(H)** Plot of theoretical AgNP concentration calculated from Beer-Lambert's Law.

3.5 Most Promising System

To prevent supersaturation, the logical method was to decrease the concentration of $AgNO_3$ significantly. The systems here therefore consisted of 0.1 mM $AgNO_3$ and 3 mM citrate. The extinction spectra were measured every 30 min for 180 min, where the plasmonic peak maintained a max wavelength around 405 nm (**Figure 3.8A**). The extinction intensity at max wavelength (**Figure 3.8D, black**) of the plasmonic peak can be seen to still have that incubation period for the first 60 min, similar to that observed for the 1 mM $AgNO_3$ experiment mentioned previously. Due

to the lower concentration of precursor, the rate of nucleation is significantly slower as well. To enhance the growth rate, the pH of the solution was adjusted with NaOH as it is known that pH can impact the nucleation and growth of NPs. NaOH is used here as both a pH adjuster and an additional reducing agent. The pH of the solution with no NaOH added was 8.3. When increasing the pH to 9.5, the extinction spectra follow the same trend as that of pH 8.3, but at a faster rate (**Figure 3.8B**). The rate of nucleation increased, and the incubation period shortened to 30 min before the extinction intensity trend became linear (**Figure 3.8D, blue**).

A final adjustment to a pH of 10.3 showed results that were completely unexpected. What we found was that the extinction spectra show a large shift in max wavelength over the course of the synthesis from 420 nm to 400 nm at the end (**Figure 3.8C**). Examining the intensity at max wavelength over time, the incubation period remains for the first 30 min as that of pH 9.5, but exponentially increases after that until it levels out at 150 min with an intensity of roughly 1.5, where all the precursor has been consumed (**Figure 3.8D, red**). This final system gave us the S-shape curve in intensity over time that we desired, indicating that this system has the potential for self-replication. TEM images of the AgNPs as well as other characterization technique were performed on this system and will be further explored in **Chapter 4**.

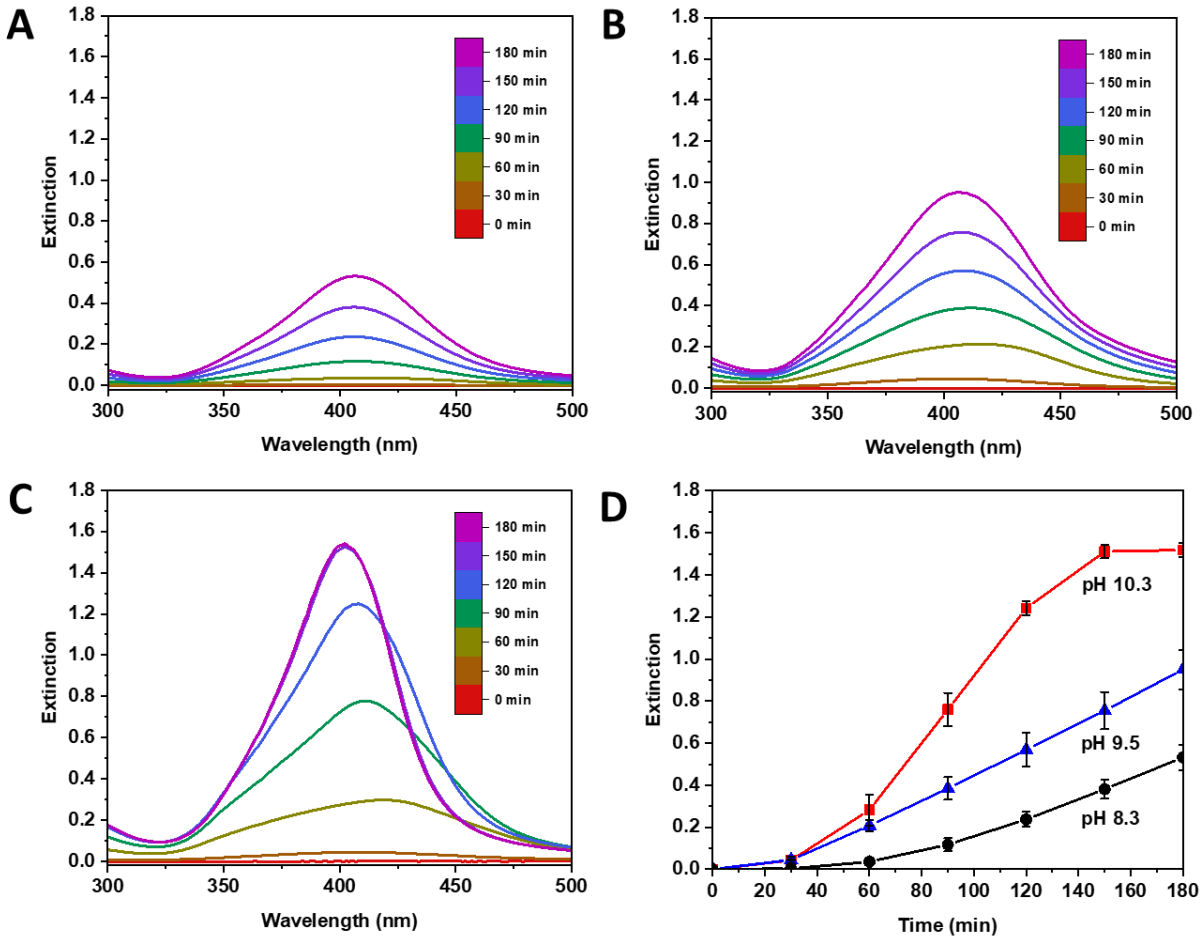

Figure 3.8. Silver nanoparticle synthesis from 0.1 mM $AgNO_3$ and 3 mM citrate with varying pH. (A) Extinction spectrum with no NaOH added (pH 8.3) at 30 min time intervals up to 180 min. **(B)** Extinction spectrum with pH adjusted to 9.5 at 30 min time intervals up to 180 min. **(C)** Extinction spectrum with pH adjusted to 10.3 at 30 min time intervals up to 180 min. **(D)** Plots of extinction intensity at max wavelength over time for pH 8.3 (black), 9.5 (blue), and 10.3 (red).

3.6 Conclusions

Over one hundred AgNP systems were evaluated for self-replicating capabilities. These systems were analyzed using a chronological series of three steps to efficiently comb through all sets. The steps consisted of visual observation of precipitation or color change, followed by analyzing AgNP concentration over time using UV-Vis spectroscopy, and finally using TEM to evaluate the change in size and shape of the AgNPs over time. Various example systems that did not pass each step were detailed to show the effectiveness of the screening steps. Through all three

steps, only one system showed initial indications of self-replication. This system consisted of citrate as both a reducing agent and stabilizer, along with an adjustment of pH to 10.3. The pH was found to be a critical factor in self-replication as kinetics trends below a pH of 10.3 showed incubation periods, but slower and linear trends in concentrations over time. Further work was performed on this system in the next chapter.

3.7 References

1. G. Clixby, L. Twyman, Self-Replicating Systems. *Org Biomol Chem*. **14**, 4170–4184 (2016).

2. P. van Nies, I. Westerlaken, D. Blanken, M. Salas, M. Mencía, C. Danelon, Self-Replication of DNA by its Encoded Proteins in Liposome-Based Synthetic Cells. *Nat Commun*. **9**, 1–12 (2018).

3. A. Robertson, A. J. Sinclair, D. Philp, Minimal Self-Replicating Systems. *Chem Soc Rev*. **29**, 141–152 (2000).

4. N. Paul, G. F. Joyce, Minimal Self-Replicating Systems. *Curr Opin Chem Biol*. **8**, 634–639 (2004).

5. M. Grzelczak, Colloidal Systems Chemistry. Replication, Reproduction and Selection at Nanoscale. *J Colloid Interface Sci*. **537**, 269–279 (2019).

6. N. A. Kotov, Inorganic Nanoparticles as Protein Mimics. *Science.* **330**, 188–189 (2010).

7. S. Li, J. Liu, N. S. Ramesar, H. Heinz, L. Xu, C. Xu, N. A. Kotov, Single- and Multi-Component Chiral Supraparticles as Modular Enantioselective Catalysts. *Nat Commun*. **10**, 1–10 (2019).

8. J. Turkevich, P. C. Stevenson, J. Hillier, A Study of the Nucleation and Growth Processes in the Synthesis of Colloidal Gold. *Discuss Faraday Soc*. **11**, 55–75 (1951).

9. J. Kimling, M. Maier, B. Okenve, V. Kotaidis, H. Ballot, A. Plech, Turkevich Method for Gold Nanoparticle Synthesis Revisited. *J of Phys Chem B*. **110**, 15700–15707 (2006).

10. J. I. Hussain, S. Kumar, A. A. Hashmi, Z. Khan, Silver Nanoparticles: Preparation, Characterization, and Kinetics. *Adv Mater Lett*. **2**, 188–194 (2011).

11. S. Das, K. Bandyopadhyay, M. Ghosh, Effect of Stabilizer Concentration on the Size of Silver Nanoparticles Synthesized Through Chemical Route. *Inorg Chem Commun*. **123**, (2021).

12. Z. Zaheer, M. Malik, F. M. Al-Nowaiser, Z. Khan, Preparation of silver nanoparticles using tryptophan and its formation mechanism. *Colloids Surf B Biointerfaces*. **81**, 587–592 (2010).

13. T. Maruyama, Y. Fujimoto, T. Maekawa, Synthesis of gold nanoparticles using various amino acids. *J Colloid Interface Sci*. **447**, 254–257 (2015).

14. L. C. Courrol, R. A. de Matos, Synthesis of Gold Nanoparticles Using Amino Acids by Light Irradiation. *Catalytic Application of Nano-Gold Catalysts,* **83** (2016).

15. R. A. de Matos, L. C. Courrol, Biocompatible silver nanoparticles prepared with amino acids and a green method. *Amino Acids*. **49**, 379–388 (2017).

16. M. Nidya, M. Umadevi, P. Sankar, R. Philip, B. J. M. Rajkumar, l-Phenylalanine functionalized silver nanoparticles: Photocatalytic and nonlinear optical applications. *Opt Mater (Amst)*. **42**, 152–159 (2015).

17. H. E. Lee, H. Y. Ahn, J. Mun, Y. Y. Lee, M. Kim, N. H. Cho, K. Chang, W. S. Kim, J. Rho, K. T. Nam, Amino-acid- A nd peptide-directed synthesis of chiral plasmonic gold nanoparticles. *Nature*. **556**, 360–364 (2018).

18. S. Perni, V. Hakala, P. Prokopovich, Biogenic synthesis of antimicrobial silver nanoparticles capped with l-cysteine. *Colloids Surf A Physicochem Eng Asp*. **460**, 219–224 (2014).

19. N. Cathcart, V. Kitaev, Symmetry Breaking by Surface Blocking: Synthesis of Bimorphic Silver Nanoparticles, Nanoscale Fishes and Apples. *Scientific Reports* **6**, 1–10 (2016).

20. S. E. Lohse, N. Burrows, L. Scarabelli, L. M. Liz-Marzán, C. J. Murphy, Anisotropic noble metal nanocrystal growth: The role of halides. *Chemistry of Materials*. **26**, 34–43 (2014).

21. S. Taheri, A. Cavallaro, S. N. Christo, L. E. Smith, P. Majewski, M. Barton, J. D. Hayball, K. Vasilev, Substrate independent silver nanoparticle based antibacterial coatings. *Biomaterials*. **35**, 4601–4609 (2014).

22. C. Battocchio, C. Meneghini, I. Fratoddi, I. Venditti, M. V. Russo, G. Aquilanti, C. Maurizio, F. Bondino, R. Matassa, M. Rossi, S. Mobilio, G. Polzonetti, Silver nanoparticles stabilized with thiols: A close look at the local chemistry and chemical structure. *Journal of Physical Chemistry C*. **116**, 19571–19578 (2012).

23. D. Paramelle, A. Sadovoy, S. Gorelik, P. Free, J. Hobley, D. G. Fernig, A rapid method to estimate the concentration of citrate capped silver nanoparticles from UV-visible light spectra. *Analyst*. **139**, 4855–4861 (2014).

24. D. H. Lee, J. R. Granja, J. A. Martinez, K. Severin, M. R. Ghadiri, A Self-Replicating Peptide. *Nature*. **382**, 525–528 (1996).

25. X. Li, J. Chmielewski, Peptide Self-Replication Enhanced by a Proline Kink. *J Am Chem Soc*. **125**, 11820–11821 (2003).

26. V. K. Lamer, R. H. Dinegar, Theory, Production and Mechanism of Formation of Monodispersed Hydrosols. *J Am Chem Soc*. **72**, 4847–4854 (1950).

Chapter 4 Coupled Self-Replication and Self-Assembly of Inorganic Nanoparticles

This chapter was partially adapted from a publication currently in submission: McGlothin, Connor and Kotov, Nicholas. "Coupled Self-Replication and Self-Assembly of Inorganic Nanoparticles" *Science* (2023)

4.1 Introduction

Being a part of the quest for understanding the origin of life, self-replication processes for a variety of organic molecules and colloids have received a lot of attention. These studies were predominantly focused on organic compounds exemplified by nucleic acids[1–3], peptides[4–6], and surfactants[7,8], proceeding either via chemical templating[1–6,8] or molecular division[7]. These studies posed exciting fundamental questions related to thermodynamically open systems and complex soft matter. However, the technological consequences of these findings are not apparent, in part because the molecules and particles involved in them tend to be complex and environmentally sensitive. Looking for practical self-replicating systems, inorganic nanoparticles (NPs) stand out by their structural simplicity and environmental robustness. From the fundamental perspective, NPs open the path to minimalistic self-replicating system that can be completely abiotic. Their technological significance is associated with the optical, catalytic, and electrical properties, related, for instance to plasmonic states, absent in organic particles and molecules. These properties also open a possibility of exploring open soft matter systems where self-replication and self-assembly

are coupled, which can, in turn, also contribute to their practicality due to energy efficiency of the self-assembly phenomena.

Mirroring some organic systems, self-replication of NPs via chemical templating has been modeled computationally,[9–13] however the pathway to its experimental realization and mechanism identification is not obvious. Similarly, self-replication by molecular division is expected to require much higher (>10x) activation energy than in organic systems even for the smallest of NPs, which also makes it experimentally problematic. Coupling these thermodynamically demanding processes with self-assembly creates an additional set of chemical challenges. Instead of these pathways, we took advantage of non-classical nucleation specific to NPs and a variety of inorganic nanostructures. This process enabled us to combine autocatalytic reduction of metals with heterogeneous agglomerations of nanoclusters at the interface of a 'parent' particle. The newly formed particle can, in turn, produce its own 'daughter' particles. Besides the familiar chain reactions in uranium, such self-replicating systems should result in the characteristic non-linear sigmoidal, or S-shaped, kinetic curves typical for some artificial and biological systems such as autocatalytic surfactants[14–16] and yeast colonies[17–19], respectively. Importantly, non-classical nucleation can also lead to uniquely complex geometries and hierarchical assemblies,[20–22] which is not possible for classical nucleation phenomena[23] or even autocatalytic growth of particles.[24] While being a theoretically attractive possibility, the realization of such system is non-trivial because surface ligands responsible for NP stability typically represented by organic surfactants[22,25], impede electron transport at the interface[26] making either self-replication or self-assembly impossible.

4.2 Methods

4.2.1 Self-Replication Synthesis

Silver NPs (AgNPs) were synthesized through a photoinduced reaction with an 8 W 365 nm ultraviolet (UV) portable lamp (Analytik Jena). For most experiments, 3 mM citrate and 0.1 mM $AgNO_3$ were mixed in a 50 mL volume of water. 0.1 M NaOH was added dropwise to the solution while stirring until the solution reached a pH of 10.3. The concentration of the silver precursor was chosen so that the final concentration of plasmonic AgNPs does not saturate the UV-Vis spectrometer throughout the entire synthesis. The solution was placed in an ice bath and dark environment to maintain a constant temperature of 3-5^{o}C throughout the synthesis while eliminating any thermodynamic effects caused by heating from the light source and to eliminate ambient light effects, respectively. During the reaction, the solution is illuminated with the UV lamp for up to 3 hours while constantly agitated with a stir bar. Aliquots of the solution were taken at various time points during the synthesis and characterised immediately under ultraviolet-visible (UV-Vis) spectroscopy to ensure no precipitated of silver oxide (Ag_2O) occurred. For experiments with the 8 W lamp, light intensity at the solution was 1.3 mW/cm^2. For the higher intensity light experiments, a 100 W 365 nm high intensity portable UV lamp (Analytik Jena) was used and the distance between the solution and light was adjusted for the other two light intensities used in this study (8 and 17.2 mW/cm^2).

4.2.2 Measurements of Nanoparticle Concentration Over Time

For preliminary screening, an Agilent 8453 UV-Vis spectrometer was used to analyse the extinction spectra of the AgNP solution at various times through the synthesis. 530µL aliquots of sample were taken from the solution at varying time points (e.g., every 10, 15, or 30 min) and deposited into a micro spectrophotometer cell (Starna Cells) for analysis. The plasmonic peak of

the AgNPs measured from 400 to 420 nm during the synthesis, with a Gaussian distribution roughly between 325 nm and 500 nm, was further used for the analysis.

The concentration of NPs was measured using a Malvern Nanosight NS300 and NP tracking analysis (NTA). For NTA, a 405 nm laser module was used to track the number of NPs. The 405 nm laser is within the absorbance range of the AgNPs and as a result, will lead to visually observable new AgNP nucleation when viewing the solution under the laser module. To counteract the unintended nucleation, 0.1 mM NaCl was mixed in the aliquot of sample to prevent further formation of AgNPs during analysis. Any unreacted Ag ions in the solution also reacted with NaCl and precipitated as AgCl.[42] The solution was centrifuged at 2,500 rpm for 10 minutes in an Eppendorf 5417R to separate out the larger AgCl particles from the sample. UV-Vis spectroscopy was used to ensure that the AgNPs remained stable in the solution with NaCl. It was discovered that the spectra does not change, which indicates that the AgNPs remained stable in the solution with NaCl. NTA was ran 5 times to get an accurate concentration and error.

4.2.3 TEM Imaging of Silver Nanoparticles

TEM imaging was performed on a Thermo Fisher Talos F200X G2 scanning transmission electron microscope (S/TEM) with a 200 kV accelerating voltage. TEM samples were prepared by drop casting 4μL of solution on a 400 mesh copper grid with an ultrathin carbon film on lacey carbon support film (Ted Pella, Cat.# 01824) after centrifuging the solution at 12,500 rpm for 30 minutes to remove unreacted Ag ions and residual citrate and washed with ultrapure water. The TEM sample was allowed to air dry over night before being imaged.

4.2.4 Dark-Field Microscopy for Observing Formation of NP Assemblies

Dark-field microscopy was performed using an Olympus IX81 inverted microscope equipped with an Olympus U-DCW dark-field oil-immersion objective (NA 1.2-1.4). The

scattered light was captured through a 60x dry objective (NA 0.9, Olympus) and imaged through an EMCCD camera (Andor IXon Ultra). The solution was imaged between a glass slide and a cover slip with cover slip spacers to allow a small gap to fill up with the unreacted self-replicating solution. The solution was sealed using bee wax to ensure no evaporation leading to false Brownian motion and unwanted flow under imaging. The 8W 365nm UV light was illuminated on the sample during the imaging to allow synthesis of the AgNPs while imaging.

4.2.5 Layer-by-Layer Functionalized TEM Grids for Moment-in-Time Experiment

To capture AgNP assembles as they are assembled in the solution during the synthesis, TEM grids were functionalized with PDDA and PSS. Layer-by-layer deposition was performed first with PDDA where the TEM grid was submerged in a 1 wt% aqueous solution of PDDA for 10 minutes. The TEM grid was removed and washed 3 times with water to remove any residual PDDA solution. The grid is air dried and then submerged in a 1 wt% aquoues solution of PSS for 10 minutes. The grid was again washed 3 times with water and allowed to air dry. This process was repeated to create 3 bilayers to ensure a uniform coating. One more layer of PDDA was applied to leave the surface positively charged to attract the negatively charged AgNPs. The functionalized TEM grid was dipped in the reaction solution at the inflection point of the synthesis (60 min), where there should me the maximum rate of self-replication and the most AgNP assemblies, and immediately removed to prevent any additional nucleation on the grid. The TEM grid was the washed with water 3 times to remove any residual reaction solution and leave only the moment-in-time capture of the assemblies. The grid was air dried, and the assemblies were then imaged in under TEM.

4.2.6 Cryo-TEM for Moment-in-Time Experiment

Cryo-TEM was performed on a Thermo Fisher Talos F200X G2 scanning transmission electron microscope (S/TEM) with a 200 kV accelerating voltage. An aliquot of the reaction solution was taken at the inflection point (60 min) of the synthesis where the most self-replication is occurring. The solution was immediately drop-casted on a TEM grid and blotted using filter paper to create a thin enough liquid layer for viewing under TEM. The grid was then instantly vitrified by submerging it in liquid ethane followed by submerging the grid in liquid nitrogen. The frozen TEM grid was setup in a Gatan Elsa cryo-transfer holder that is specialized for cryo-TEM and imaged.

4.2.7 In Situ Liquid TEM for Observance of Nanoparticle Replication

In situ TEM was performed on a Thermo Fisher Talos F200X G2 scanning transmission electron microscope (S/TEM) with a 200 kV accelerating voltage. A viewing cell (Hummingbird Scientific) consisting of two silicon chips with transparent silicon nitride windows separated by a 100 nm spacer were used. The viewing cell chips were plasma cleaned to create a hydrophilic surface for better flow and dispersion of the solution in the holder. A liquid cell TEM holder (Hummingbird Scientific) was assembled with the silicon chips and placed in a pumping station (Hummingbird Scientific) to ensure that the holder maintains its integrity under vacuum before being placed in the TEM. The self-replicating solution was pumped through the holder, and the liquid cell holder was placed in the TEM equipment and aligned to view the sample. Electron dose rate is kept at or below 130 e^-/Ås to allow for self-replication without other species forming. To view the nuclei forming at the interface of parent NPs, the electron dose rate was increased above 200 e^-/Ås to destabilize the nuclei to view them.

4.2.8 Kinetic Model

The kinetic model is a modification of the Finke-Watzky model which is a two-step simplified model of NP nucleation and autocatalytic growth shown below[24]:

$$A \overset{k_1}{\rightarrow} B \tag{4.1}$$

$$A + B \overset{k_2}{\rightarrow} 2B \tag{4.2}$$

Here, A is the precursor which in this case is Ag^+ ions and B is the AgNPs. The first equation is the reduction of siler ions to silver NPs. The second equation is the autocatalytic growth of the silver NPs. Our kinetic model follows this mechanism but is first modified to include only autocatalytic growth on the surface of the AgNPs. Our model also incorporates a third equation, which is the self-replicating equation where the fully grown AgNPs induce the nucleation of silver nuclei at a rate faster than the first equation. Full explanation of kinetic model can be seen in **SI 9.**

4.3 Results and Discussion

4.3.1 Self-Replication Experimental Kinetics

After a methodical screening (**Figure 3.1**), we implemented an experimental model based on silver nanoparticles (AgNPs) carrying citrate surface ligands at a critical pH. While being common, we found that its minimalism is critical for the self-replication process and essential for its technological relevance. The use of citrate also enables heterogeneous nucleation to be faster than homogeneous nucleation from the precursor in solution.[27] Under 365nm UV light with an intensity of 1.3mW/cm^2, the solution of 0.1 mM silver nitrate ($AgNO_3$) and 3 mM sodium citrate dihydrate (citrate) at pH of 10.3 displayed nearly ideal S-shaped curves observed by ultraviolet-visible (UV-Vis) spectroscopy, which is indicative of self-replication **(Figure 4.1B)**. The

extinction peak around 400-420 nm, which is characteristic of spherical AgNPs, was observed to exponentially increase in intensity (**Figure 4.1A, Figure A.1A**).

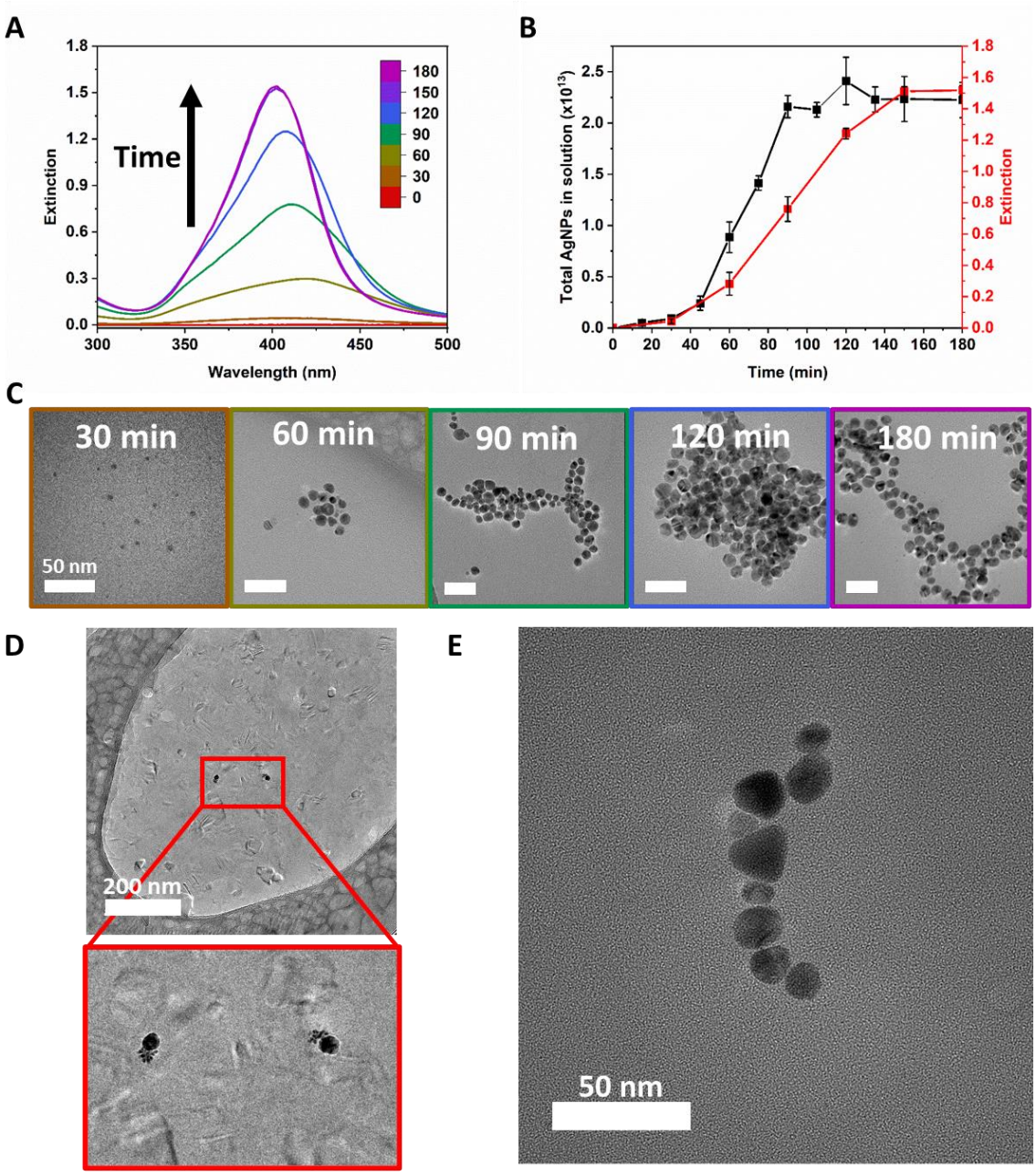

Figure 4.1. Characterisation of self-replicating system via UV-Vis spectroscopy and TEM. (A) Extinction spectrum of AgNP solution at 30 min intervals **(B)** extinction intensity at the max wavelength (red) compared to the total actual concentration of AgNP measured with NTA (black) **(C)** TEM images of AgNPs at 30 min intervals of the synthesis. Border color matches time points for **A**. Scale bars are 50 nm **(D)** Cryo-TEM image, and a zoom in view of the particles (red box), at 60 min synthesis of the nucleation of silver nuclei at the interface of a parent AgNP **(E)** layer-by-layer deposition of PSS and PDDA on a TEM grid for moment-in-time capture of the chain-like assembly of the self-replicating AgNPs

It is important to note that this system is sensitive to pH (**Figure A.2**). In solutions with pH below 10.3, the kinetics curve in concentration loses the characteristic non-linearity while pH levels beyond 10.3 leads to visual precipitation of silver oxide (Ag_2O) microparticles. Since optical effects reflect not only the total number of NPs, but also their size that can change concurrently with the nucleation,[28,29] electron microscopy was used to evaluate how the NP size and shape changes throughout the illumination process (**Figure 4.1C**). While maintaining an approximately spherical shape throughout the synthesis,[30,31] the average diameter of the NPs increases quickly to 6.6 nm ± 2.7 nm at 30 min to 16.1 nm ± 2.2 nm at 60 min of illumination (**Figure A.3**). At this point up to completion at 3 hours, the growth rate significantly decreases where over the next 2 hours the average diameter reaches 18.2 nm ± 2.1 nm. This rapid increase in diameter is consistent with autocatalytic NP surface growth after they nucleate.[24,29] Indeed, NPs display fastest growth when smaller below 5 nm and the growth rate gradually decreases as the particle becomes larger due to increased thermodynamic stability and ligand coverage.[25] As the NPs are increasing in size on average throughout the synthesis, one would expect to see effects on the extinction intensity of the solution as larger particles will scatter more light and will also lead to shifts to higher max extinction wavelengths.[31] Interestingly, analysing the max wavelength (**Figure A.1B**) at each point in time of the illumination shows that the plasmonic peak shifts to a lower wavelength, or blue-shifts, which is in contradiction to what one would expect for plasmonic NPs increasing in size. The blue shift can be attributed to the change in charge density around the AgNPs (**Figure A.4**).[32] As a result, extinction is not perfectly correlated to concentration of NPs, but is still good for preliminary screening of self-replicating capabilities.

The concentration of NPs was directly measured using NP tracking analysis (NTA, **Figure 4.1B**), where the S-shape curve is maintained with only slight deviation from the extinction results.

The incubation period is still during the first 30 minutes, but the number of NPs becomes roughly constant around 90 minutes of illumination. When examining the zeta-potential of the solution, it was found that the distribution of surface charge is larger than that of silver NPs purchased from Sigma-Aldrich with a known size of 20nm (**Figure A.5**). From these results, it is hypothesized that the interface of the NPs is acting as a nucleation site for new nuclei and therefore acting as a catalyst for its own formation. The nuclei forming at the interface is dynamically assembled with the previous parent NPs as it grows, leading to transient self-assembled structures where NPs are organized into chains. Dark-field microscopy enables one to view in real-time the formation of the NP chains (**Figure A.6**). Tracking the number of silver NPs in the field of view of the microscopy also shows an incubation period followed by a rapid increase in NP count further supporting the kinetics seen prior.

4.3.2 Moment-in-Time Imaging

Two techniques were utilized to capture moment-in-time snapshots of the NP self-replication and self-assembly, where the key results from these snapshots were to capture the initial self-replication as well as the interaction between particles. (**1**) Cryo-TEM images taken at the inflection point of the sigmoidal curve at 60 minutes. We observed the formation of 1-2 nm nuclei form near the surface of larger 10-12 nm NPs **(Figure 4.1D).** The nuclei will nucleate a new particle providing a vivid evidence of autocatalytic NP growth and multiplication. The cessation of the growth and formation of a new nucleus is likely to occur due to the accumulation of charge on the NP surface. (**2**) PSS/PDDA functionalized TEM grids were dipped in the solution at the 60 minute inflection point to capture various lengths of chain-like assemblies of AgNPs on the grid in real time (**Figure 4.1E, A.7)**. NPs are 12-16 nm in diameter, which is in line with what we observed in **Figure 4.1C, D**. The distance between the NPs is 0.5-1 nm (**Figure A.8**) conducive

with the distance characteristic of the ejection of hot electrons that can reduce the Ag^+ ions around the parent particle.

4.3.3 In Situ Imaging

Albeit under illumination with electron beam rather than by UV light, liquid-state TEM (**Figure 4.2**) presents a vivid picture of continuous self-replication of NPs producing continuous chains. The NPs grow rapidly until they reach 13.6nm ± 3.5nm in diameter at which point the growth slows down and another NP nucleates at the interface of the previous particle, which matches the growth mechanism inferred from (**Figure 4.1E, Figure A.8**). We note that there are two additional processes taking place: (1) NPs that nucleate outside of the focus area can diffuse away from the point of their origin and attach to the growing chain and (2) NPs can be attracted to the windows of the TEM cell. Increasing the electron dosage above 200 e^-/Ås leads to instability of the nuclei at the interface of NPs (**Figure A.9**), which also allows us to pinpoint the minimal size of the nuclei that nucleate at the interface to be roughly 0.5 nm in diameter. Running a control when the sigmoidal curve and self-replication are not observed (**Figure A.10**), i.e., for the linear kinetic regime of a non-replicating synthesis (**Figure A.2, black curve**), we only observed the nucleation and slow growth of NPs in the bulk without any formation of nuclei near the surface of the parent NPs.

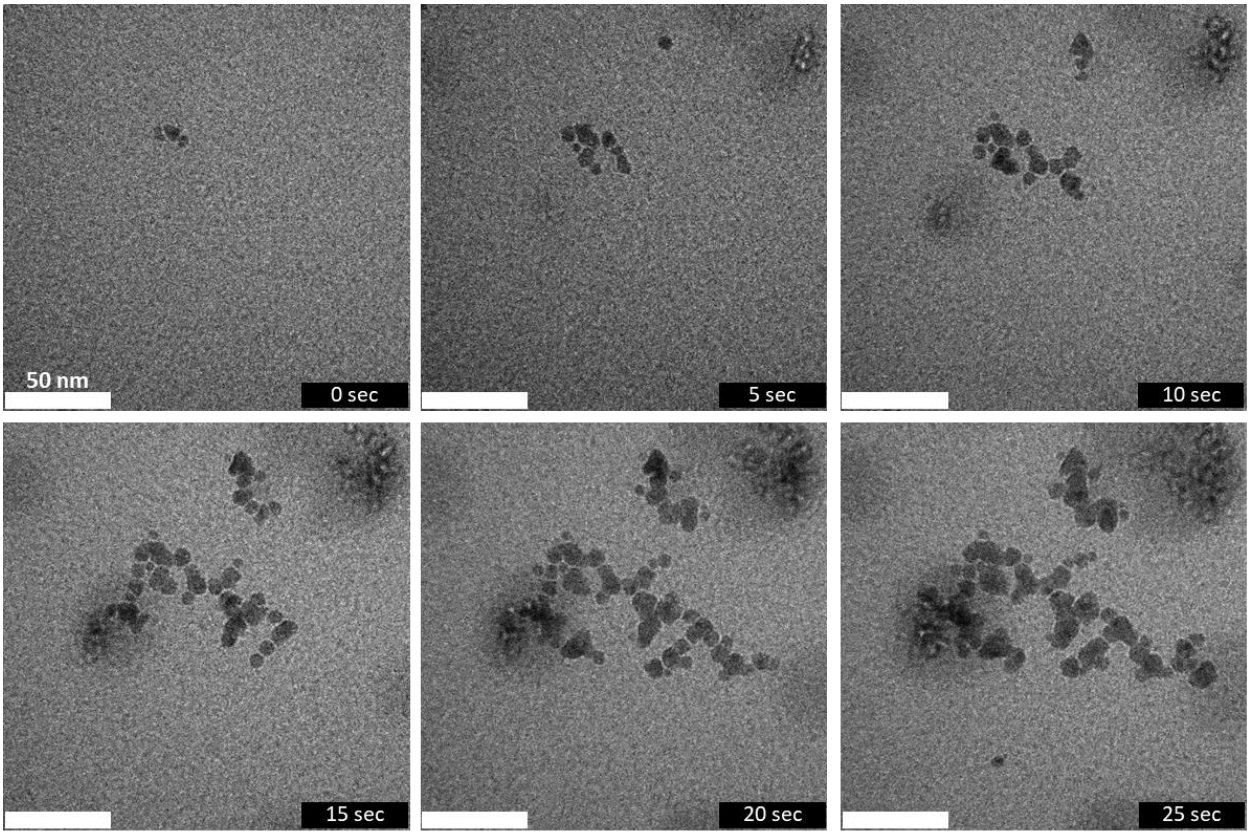

Figure 4.2. Liquid TEM at 5 sec intervals of silver NP self-replication into chain-like assemblies. Silver nuclei form at the interface of previously nucleated NPs in the chain. Scale bars are 50 nm.

4.3.4 Kinetic Model Results

A kinetic model was developed to describe self-replication based off the mechanism of continuous nucleation and autocatalytic growth. The classical Finke-Watzky[24] model for autocatalytic reactions shows a poor overall fit to the NP concentration over time (**Figure A.11**). Our model included an additional equation for heterogeneous nucleation/agglomeration at the interface of another NP. Furthermore, we also explicitly include the catalytic role of NP surfaces where the formation of daughter particles occurs arriving to Equations **1-3** (see definitions and additional derivations in **A.12):**

$$Ag^{+} \overset{k_1}{\rightarrow} Ag^{0} \tag{4.3}$$

$$Ag^{+} + Ag^{0}_{surf} \overset{k_2}{\rightarrow} Ag^{0} + Ag^{0}_{surf} \tag{4.4}$$

$$Ag^{+} + N \overset{k_3}{\rightarrow} Ag^{0} + N \quad (4.5)$$

Fitting the experimental data to the differential equations corresponding to these chemical equations, we found that the kinetic constants seen in **Table 1** for light intensity of 1.3 mW/cm^2 (**Figure 4.3A, B, Figure A.12A, B**). The observed constants are comparable to those seen in literature for the nucleation, growth, and agglomeration of transition-metal nanoclusters[33–35] with k_1, k_2, and k_3 estimated to be 1x10^{-3} – 1x10^{-9}, 1 – 1x10^{4}, 1 – 1x10^{5}, respectively.

Table 4.1. Rate constants k_1, k_2, and k_3 for varying light intensities.

Light Intensity	k_1 (min^{-1})	k_2 ([Ag^0_{surf}]$^{-1}$min^{-1})	k_3 ([NP]$^{-1}$min^{-1})
1.3 mW/cm^2	7.2x10^{-8}	2.93x10^{-7}	5.85x10^{-7}
8 mW/cm^2	8280	11800	21200
17.2 mW/cm^2	22800	28500	49400

To further substantiate this kinetic model involving the steps of autocatalytic growth and agglomeration, the light intensity of the UV light was increased from 1.3 mW/cm^2 used **Figure 4.1** to 8 mW/cm^2 and 17.2 mW/cm^2. The kinetic model was fitted to the new experimental concentration and diameter curves (**Figure 4.3C-F, Figure A.12C-F**) juxtaposed with corresponding TEM images in **Figure A.13, A.14**. All three rate constants (k_1, k_2, and k_3) saw an increase with a higher light intensity (**Table 1**). It was found that the change in light intensity follows a pseudo-linear trend for each rate constant versus light intensity (**Figure A.15**), which is typical for the photoinduced reactions.[36–38]

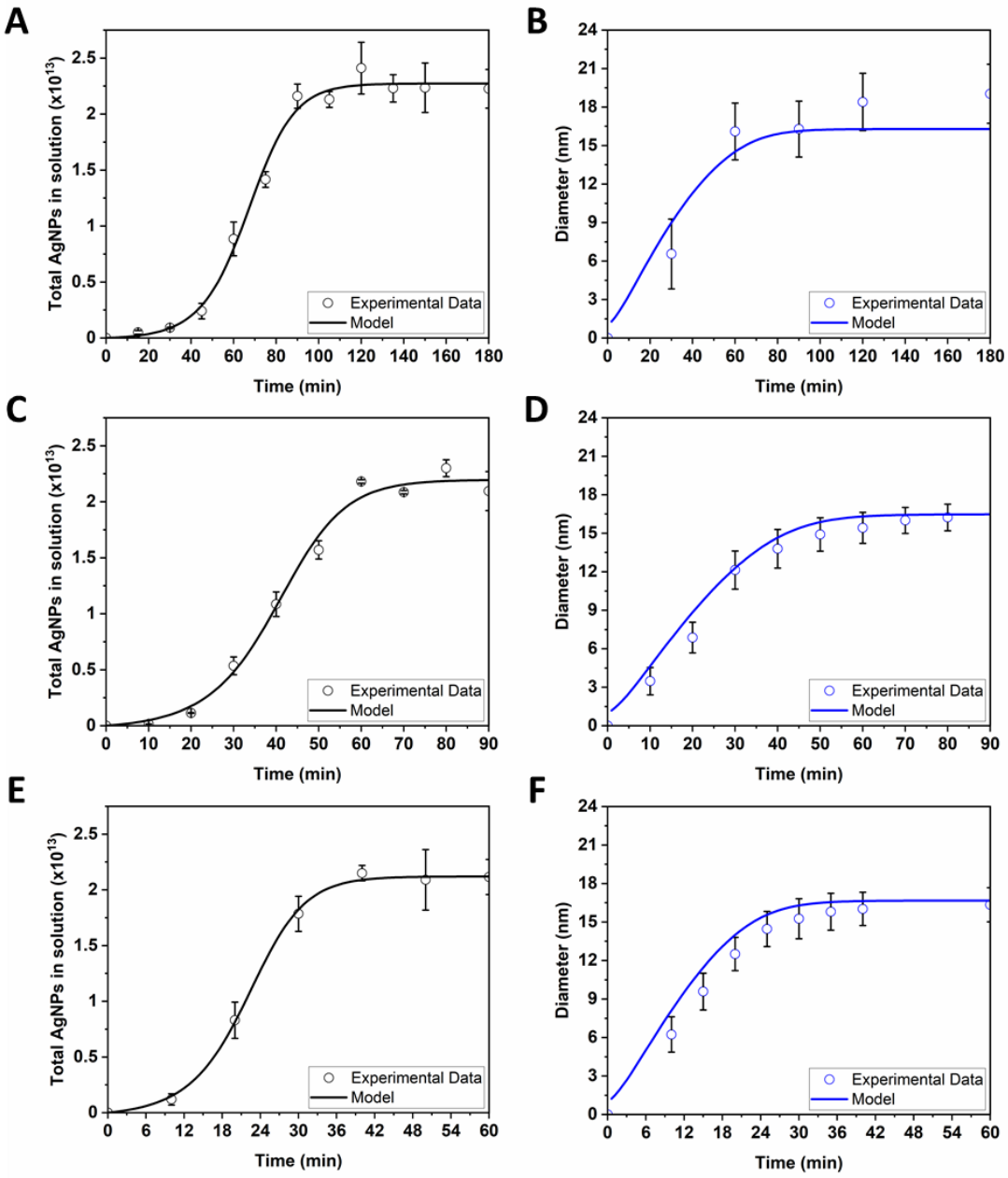

Figure 4.3. Computational modeling of self-replicating system. (A) Self-replicating model (line) fitted (R^2 = 0.993) to 1.3 mW/cm^2 light intensity experimental NP concentration data (hollow circles) **(B)** model (line) fitted (R^2 = 0.895) to 1.3 mW/cm^2 light intensity experimental NP diameter data (hollow circles) **(C)** model (line) fitted (R^2 = 0.991) to 8 mW/cm^2 light intensity experimental NP concentration data (hollow circles) **(D)** model (line) fitted (R^2 = 0.969) to 8 mW/cm^2 light intensity experimental NP diameter data (hollow circles) **(E)** model (line) fitted (R^2 = 0.998) to 17.2 mW/cm^2 light intensity experimental NP concentration data (hollow circles) **(F)** model (line) fitted (R^2 = 0.937) to 17.2 mW/cm^2 light intensity experimental NP diameter data (hollow circles)

4.4 Conclusions

This study documents a coupled self-replicating and self-assembly of NPs confirmed using ex-situ and in-situ characterisation methods. It was further supported by a kinetic model that follows a three-step self-replicating process to show how the kinetics impact the nucleation and growth. Our findings provide insight into a never before realized form of non-classical inorganic nucleation and expands the range of what self-replication can encompass, and hopefully spark the question of how inorganic materials could provide insight into the origin of life.[41] The realization of nucleation coupled with self-assembly of daughter particles without agglomeration or coalescence, as seen previously in literature[26], opens another avenue for NP interactions that can lead to more unique material design and synthesis. This will have various applications in catalysis, optics, sensing, and electrochemistry. Their excellent optical, electrical, catalytic, sensing, and antibacterial properties of silver give this unique thin film structure numerous uses in areas such as surface-enhanced Raman spectroscopy (SERS), optical senses, and photovoltaics.

4.5 References

1. von Kiedrowski, G. A Self-Replicating Hexadeoxynucleotide. *Angewandte Chemie International Edition in English* **1986**, *25* (10), 932–935.

2. Paul, N.; Joyce, G. F. A Self-Replicating Ligase Ribozyme. *Proc Natl Acad Sci U S A* **2002**, *99* (20), 12733–12740.

3. Olea, C.; Horning, D. P.; Joyce, G. F. Ligand-Dependent Exponential Amplification of a Self-Replicating L-RNA Enzyme. *J Am Chem Soc* **2012**, *134* (19), 8050–8053.

4. Lee, D. H.; Granja, J. R.; Martinez, J. A.; Severin, K.; Ghadiri, M. R. A Self-Replicating Peptide. *Nature* **1996**, *382* (6591), 525–528.

5. Li, X.; Chmielewski, J. Peptide Self-Replication Enhanced by a Proline Kink. *J Am Chem Soc* **2003**, *125* (39), 11820–11821.

6. Ikeda, K.; Nakano, M. Self-Reproduction of Nanoparticles Through Synergistic Self-Assembly. *Langmuir* **2015**, *31* (1), 17–21.

7. Taylor, J. W.; Eghtesadi, S. A.; Points, L. J.; Liu, T.; Cronin, L. Autonomous Model Protocell Division Driven by Molecular Replication. *Nat Commun* **2017**, *8* (1).

8. van Nies, P.; Westerlaken, I.; Blanken, D.; Salas, M.; Mencía, M.; Danelon, C. Self-Replication of DNA by Its Encoded Proteins in Liposome-Based Synthetic Cells. *Nat Commun* **2018**, *9* (1), 1–12.

9. Zhang, R.; Walker, D. A.; Grzybowski, B. A.; Olvera de la Cruz, M. Accelerated Self-Replication under Non-Equilibrium, Periodic Energy Delivery. *Angewandte Chemie* **2014**, *126* (1), 177–181.

10. Zhang, R.; Dempster, J. M.; Olvera De La Cruz, M. Self-Replication in Colloids with Asymmetric Interactions. *Soft Matter* **2014**, *10* (9), 1315–1319.

11. Dempster, J. M.; Zhang, R.; Olvera De La Cruz, M. Self-Replication with Magnetic Dipolar Colloids. *Phys Rev E Stat Nonlin Soft Matter Phys* **2015**, *92* (4), 1–12.

12. Zeravcic, Z.; Brenner, M. P. Self-Replicating Colloidal Clusters. *Proc Natl Acad Sci U S A* **2014**, *111* (5), 1748–1753.

13. Tanaka, H.; Zeravcic, Z.; Brenner, M. P. Mutation at Expanding Front of Self-Replicating Colloidal Clusters. *Phys Rev Lett* **2016**, *117* (23), 1–6.

14. Kahana, A.; Lancet, D. Self-Reproducing Catalytic Micelles as Nanoscopic Protocell Precursors. *Nature Reviews Chemistry* **2021**, *5* (12), 870–878.

15. Wick, R.; Walde, P.; Luisi, P. L. Light Microscopic Investigations of the Autocatalytic Self-Reproduction of Giant Vesicles. *J Am Chem Soc* **1995**, *117* (4), 1435–1436.

16. Bissette, A. J.; Odell, B.; Fletcher, S. P. Physical Autocatalysis Driven by a Bond-Forming Thiol–Ene Reaction. *Nature Communications* **2014**, *5* (1), 1–8.

17. Ahmadian, M.; Tyson, J. J.; Peccoud, J.; Cao, Y. A Hybrid Stochastic Model of the Budding Yeast Cell Cycle. *npj Systems Biology and Applications* **2020**, *6* (1), 1–10.

18. Olivares-Marin, I. K.; González-Hernández, J. C.; Regalado-Gonzalez, C.; Madrigal-Perez, L. A. Saccharomyces Cerevisiae Exponential Growth Kinetics in Batch Culture to Analyze Respiratory and Fermentative Metabolism. *J Vis Exp* **2018**, *2018* (139), 58192.

19. Laomettachit, T.; Kraikivski, P.; Tyson, J. J. A Continuous-Time Stochastic Boolean Model Provides a Quantitative Description of the Budding Yeast Cell Cycle. *Scientific Reports* **2022**, *12* (1), 1–12.

20. Lee, J.; Yang, J.; Kwon, S. G.; Hyeon, T. Nonclassical Nucleation and Growth of Inorganic Nanoparticles. *Nature Reviews Materials*. **2016**, 1 (8) 1–16.

21. Tang, R.; Jin, B.; Jin, B.; Liu, Z. Recent Experimental Explorations of Non-Classical Nucleation. *CrystEngComm* **2020**, *22* (24), 4057–4073.

22. Wu, K. J.; Tse, E. C. M.; Shang, C.; Guo, Z. Nucleation and Growth in Solution Synthesis of Nanostructures – From Fundamentals to Advanced Applications. *Prog Mater Sci* **2022**, *123*, 100821.

23. Lamer, V. K.; Dinegar, R. H. Theory, Production and Mechanism of Formation of Monodispersed Hydrosols. *J Am Chem Soc* **1950**, *72* (11), 4847–4854.

24. Watzky, M. A.; Finke, R. G. Transition Metal Nanocluster Formation Kinetic and Mechanistic Studies. A New Mechanism When Hydrogen Is the Reductant: Slow, Continuous Nucleation and Fast Autocatalytic Surface Growth. *J Am Chem Soc* **1997**, *119* (43), 10382–10400.

25. Mozaffari, S.; Li, W.; Dixit, M.; Seifert, S.; Lee, B.; Kovarik, L.; Mpourmpakis, G.; Karim, A. M. The Role of Nanoparticle Size and Ligand Coverage in Size Focusing of Colloidal Metal Nanoparticles. *Nanoscale Adv* **2019**, *1* (10), 4052–4066.

26. Cheng, Y.; Tao, J.; Zhu, G.; Soltis, J. A.; Legg, B. A.; Nakouzi, E.; de Yoreo, J. J.; Sushko, M. L.; Liu, J. Near Surface Nucleation and Particle Mediated Growth of Colloidal Au Nanocrystals. *Nanoscale* **2018**, *10* (25), 11907–11912.

27. Zhou, J.; Yang, Y.; Yang, Y.; Kim, D. S.; Yuan, A.; Tian, X.; Ophus, C.; Sun, F.; Schmid, A. K.; Nathanson, M.; Heinz, H.; An, Q.; Zeng, H.; Ercius, P.; Miao, J. Observing Crystal Nucleation in Four Dimensions Using Atomic Electron Tomography. *Nature* **2019**, *570* (7762), 500–503.

28. Wen, T.; Zhang, X.; Zhang, D.; Li, Y.; Zhang, H.; Zhong, Z. The Interplay between Monomer Formation, Nucleation and Growth during Colloidal Nanoparticle Synthesis. *Journal of Materials Science* **2021**, 56 (28), 15718-15732

29. Harada, M.; Kizaki, S. Formation Mechanism of Gold Nanoparticles Synthesized by Photoreduction in Aqueous Ethanol Solutions of Polymers Using in Situ Quick Scanning X-Ray Absorption Fine Structure and Small-Angle X-Ray Scattering. *Cryst Growth Des* **2016**, *16* (3), 1200–1212.

30. Wan, Y.; Guo, Z.; Jiang, X.; Fang, K.; Lu, X.; Zhang, Y.; Gu, N. Quasi-Spherical Silver Nanoparticles: Aqueous Synthesis and Size Control by the Seed-Mediated Lee–Meisel Method. *J Colloid Interface Sci* **2013**, *394* (1), 263–268.

31. Bastús, N. G.; Merkoçi, F.; Piella, J.; Puntes, V. Synthesis of Highly Monodisperse Citrate-Stabilized Silver Nanoparticles of up to 200 Nm: Kinetic Control and Catalytic Properties. *Chemistry of Materials* **2014**, *26* (9), 2836–2846.

32. Ershov, V.; Tarasova, N.; Ershov, B. Evolution of Electronic State and Properties of Silver Nanoparticles during Their Formation in Aqueous Solution. *Int J Mol Sci* **2021**, *22* (19).

33. Finney, E. E.; Finke, R. G. The Four-Step, Double-Autocatalytic Mechanism for Transition-Metal Nanocluster Nucleation, Growth, and Then Agglomeration: Metal, Ligand, Concentration, Temperature, and Solvent Dependency Studies. *Chemistry of Materials* **2008**, *20* (5), 1956–1970.

34. Besson, C.; Finney, E. E.; Finke, R. G. A Mechanism for Transition-Metal Nanoparticle Self-Assembly. *J Am Chem Soc* **2005**, *127* (22), 8179–8184.

35. Besson, C.; Finney, E. E.; Finke, R. G. Nanocluster Nucleation, Growth, and Then Agglomeration Kinetic and Mechanistic Studies: A More General, Four-Step Mechanism Involving Double Autocatalysis. *Chemistry of Materials* **2005**, *17* (20), 4925–4938.

36. Chiou, C. H.; Wu, C. Y.; Juang, R. S. Influence of Operating Parameters on Photocatalytic Degradation of Phenol in UV/TiO2 Process. *Chemical Engineering Journal* **2008**, *139* (2), 322–329.

37. You-Ji, L.; Wei, C. Photocatalytic Degradation of Rhodamine B Using Nanocrystalline TiO 2 – Zeolite Surface Composite Catalysts: Effects of Photocatalytic Condition on Degradation Efficiency. *Catal Sci Technol* **2011**, *1* (5), 802–809.

38. Chizhik, S.; Sidelnikov, A.; Zakharov, B.; Naumov, P.; Boldyreva, E. Quantification of Photoinduced Bending of Dynamic Molecular Crystals: From Macroscopic Strain to Kinetic Constants and Activation Energies. *Chem Sci* **2018**, *9* (8), 2319–2335.

39. Montjoy, D. G.; Hou, H.; Bahng, J. H.; Eskafi, A.; Jiang, R.; Kotov, N. A. Photocatalytic Hedgehog Particles for High Ionic Strength Environments. *ACS Nano* **2021**, *15* (3), 4226–4234.

40. Erdmanis, M.; Sievilä, P.; Shah, A.; Chekurov, N.; Ovchinnikov, V.; Tittonen, I. Focused Ion Beam Lithography for Fabrication of Suspended Nanostructures on Highly Corrugated Surfaces. *Nanotechnology* **2014**, *25* (33), 335302.

41. Adamski, P.; Eleveld, M.; Sood, A.; Kun, Á.; Szilágyi, A.; Czárán, T.; Szathmáry, E.; Otto, S. From Self-Replication to Replicator Systems En Route to de Novo Life. *Nature Reviews Chemistry* **2020**, 4 (8) 386–403.

42. Ingle, A.; Rai, M.; Gade, A.; Bawaskar, M. Fusarium Solani: A Novel Biological Agent for the Extracellular Synthesis of Silver Nanoparticles. *Journal of Nanoparticle Research* **2009**, *11* (8), 2079–2085.

43. Schaefers, S.; Rast, L.; Stanishevsky, A. Electroless Silver Plating on Spin-Coated Silver Nanoparticle Seed Layers. *Mater Lett* **2006**, *60* (5), 706–709.

Chapter 5 Exploration into Bioinspired Manufacturing Applications

Section 5.3 was partially adapted from a publication currently in submission: McGlothin, Connor and Kotov, Nicholas. "Coupled Self-Replication and Self-Assembly of Inorganic Nanoparticles" *Science* (2023)

Section 5.4.1 was partially adapted from a publication currently in submission: Kim, JY.; McGlothin, C.; Cha, M.; Pfaffenberger, Z. J.; Turali-Emre, E.S.; Choi, W.; Biteen, J. S.; Kotov, N.A. "Direct Printing of Helical Metal Arrays by Circularly Polarized Light" *Nature Synthesis* (2023)

5.1 Introduction

Nature contains a multitude of complex systems that have not been able to be efficiently replicated synthetically. Being able to mimic these complex systems with bioinspired materials can open a plethora of new applications and technological advances. Inorganic materials with their unique properties, such as optical, catalytic, and electrical characteristics, are better materials industrially than their biological counterparts. [1,2]

Chiral inorganic nanomaterials are common biomimetic systems with many applications. For plasmonic nanoparticles, the combination of the plasmonic effect coupled with chirality opens a wide range of applications in sensing, catalysis, and photonics.[3–6] Chirality in plasmonic nanoparticles can arise from either the asymmetry geometry of either individual particles or assembly of particles when no chiral ligands are present. Specifically, developing complex chiral plasmonic nanoparticles with just circularly polarized light (CPL) to transfer chirality directly from

photon to matter is a fundamentally interesting system and has been growing in popularity in the last decade.

Another unique biomimetic material is chiral plasmonic metasurfaces, with their high sensitivity to changes in their dielectric environment, make them promising materials for biosensing, catalysis, photonics, and information technologies.[4,5,7] One drawback with chiral metasurfaces is the time and money it requires to make. The most common method of manufacturing metasurfaces is nanolithography, which requires multiple lift-off and mask-alignment steps. In a typical process, a photoresist layer is deposited on a glass, quartz or sapphire surface. It is subsequently patterned through a two-photon process to create latent images for various chiral structures. After subsequent etching, the helical voids are created. These voids in the photoresist are then loaded with gold by electroplating. To make electroplating possible, a conductive layer - most typically indium tin oxide (ITO), is required. To produce the final chiral plasmonic metasurfaces, the photoresist is removed via plasma etching, which takes on the order of 10 to 20 hours.[7–10] Being able to find a method to make these metamaterials on the order of minutes would be an incredible feat for industrial scale-up.

Self-replication is one another of those complex biological systems that has not been able to be utilized for applications outside of organic materials. We seek to use our first ever self-replicating inorganic nanoparticle system to create unique structures and assemblies both on surfaces and in solution. There are two major questions that we want to answer in this chapter: 1) can we grow static self-replicating structures on substrates (**Section 5.3**), and 2) can we utilize circularly polarized light (CPL) to induce chirality into a self-replicating system (**Section 5.4**).

5.2 Methods

5.2.1 Growing Self-Replicating Silver Networks on a Substrate

Layer-by-layer deposition of poly(diallyldimethylammonium chloride) (PDDA) and poly(sodium 4-sytrenesulfonate) (PSS) were performed on silicon monoxide (SiO) transmission electron microscopy (TEM) grids and glass coverslips following the method described in **Chapter 2**. The substrates are washed with water to remove any excess polymer and dried at room temperature. The substrates are then supported on the surface of the solution at the inflection point of the synthesis (60 min) to allow only growth on the submerged side. This is done to avoid any attenuation through the solution as more NPs form if the substrate is completely submerged. The substrate is then removed from the surface of the solution after 30 min when formation of new NPs significantly decreases. The substrate is washed with water and allowed to air dry before being characterized.

ZnO/Fe_2O_3 HPs were synthesized by Dr. Elizabeth Wilson using a method developed previously in our lab. [11,12] The HPs were dispersed in the self-replicating AgNP solution at the inflection point of the synthesis (60min) and stirred for 30 min while still under illumination. The solution was centrifuged at 4000 rpm for 20 min to separate the HPs from the smaller AgNPs. The HPs were redispersed in water and then drop cast on a silicon wafer for imaging.

5.2.2 Electroless Silver Deposition on Self-Replicated Networks

Electroless Deposition was used to grow the self-replicated silver network into a thin film. The deposition solution is based off a Tollen's reagent, which consists of two solutions. [13] The first solution consists of 20mM $AgNO_3$, 8.8 mL isopropanol, 1.2 mL acetic acid, and 40 mL 25% ammonia solution. The second solution consist of 0.5 mL hydrazine and 49.5 mL isopropanol. 7.5 mL of each solution is added to 15 mL of water while stirring to create the Tollen's reagent. Due

to the short shelf life of the reagent, it must be prepared fresh each day it is used. The desired substrate is submerged in the deposition solution for 5 to 40 min depending on the desired amount of silver to be deposited. The substrate is then removed from the solution and washed 3 times in water. The substrate is air dried before any characterisation.

A four-point probe (Signatone SP4) powered by a source meter (Keithley Model 2470) is used to measure the sheet resistance of our silver thin films. A current of 1 mA was applied and the voltage was measured. The sheet resistance was calculated using Equation **6**:

$$R_S = \frac{\pi}{\ln(2)} \frac{\Delta V}{I} = 4.53236 \frac{\Delta V}{I} \quad 5.1$$

Where R_S is the sheet resistance in Ω/□, ΔV is the change in voltage (mV) measured between the two inner probes, and I is the current (mA) applied between the outer probes.

5.2.3 SEM Imaging of Silver Thin Films

Scanning electron microscopy (SEM) images were taken using a Thermo Fisher Helios 650 Nanolab at 3 kV accelerating voltage and 0.1 nA beam current. Samples that were prepared with electroless silver deposition seen above were placed in the SEM equipment for viewing.

5.2.4 Chiral Nanoparticle Synthesis via Circularly Polarized Light

A diode-pumped continuous wave laser (CrystaLaser) at a wavelength of 405 nm was used for the synthesis of both chiral Ag and Ag/Cu nanoparticles. The laser is passed through a linear polarizer and quarter-wave plate at 45° to produce CPL. The quarter-wave plate is rotated 90° relative to the previous angle to change the handedness of light. The CPL is also passed through a concave and convex lens to broaden the beam to a diameter of 1 cm to illuminate the entire solution. Aqueous 3 mM citrate solutions with varying concentrations of $AgNO_3$ and copper nitrate ($Cu(NO_3)_2$) are placed beneath the laser in a thin 5 mL vial to allow full illumination of the

solution. Solutions are left under illumination for varying times up to 18 hrs depending on which system is being tested.

To synthesize silver helicoids on surfaces, the desired substrate (either glass, ITO/glass, polydimethylsiloxane (PDMS), or silicon) was submerged in a solution of silver precursor (AgNO3, 2.5 mM) and citrate (12.5 mM), while the height from substrate to surface of the solution was fixed at 3 cm. Three diode-pumped continuous wave lasers (CrystaLaser) at three different wavelengths, 405, 532, and 660 nm, were used for the synthesis the chiral silver helicoids on surfaces. The laser emissions were broadened into spots with a diameter of 1-2 cm using a combination of Plano-concave and -convex lenses. The lasers were modulated with a linear polarizer and a quarter-wave plate to emit either left- or right-circularly polarized light (L-CPL and R-CPL, respectively). The lasers were directed perpendicular to the substrate with varying power density for different times up to 30 minutes depending on purpose of experiments. The patterned substrates were washed three times with water before optical or imaging analysis.

5.2.5 Scanning Transmission Electron Microscopy of Silver Helicoids

Scanning transmission electron microscopy (STEM) samples were prepared on polydimethylsiloxane (PDMS) substrates and transferred to a TEM grid by stamping technique. Simultaneous imaging with three different detectors were performed with FEI Helios Nanolab at 29 kV accelerating voltage.

5.2.6 Circular Dichroism and g-factor

CD spectroscopy was performed for all colloidal system using a Jasco J-815 CD spectrometer with a detector range from 200-800 nm. The CD spectra were measured with the scanning parameters: high sensitivity, 100 nm/min scanning speed, 1 nm data pitch, 5 nm bandwidth, and 1 s digital integration time. For the silver chiral helical metasurfaces, either a Jasco

J-815 or J-1700 CD spectrometer equipped with one PMT detector in the 200-800 nm range and two InGaAs near infrared (NIR) detectors for the 800-1600 nm and 1600-2500 nm range. The CD spectra were measured with the scanning parameters: 500 nm/min scanning speed, 1 nm data pitch, 5 nm bandwidth, and 0.25 s digital integration time.

Another characteristic of chiral materials that can be derived from CD spectroscopy is the anisotropy (g) factor. The g-factor is a dimensionless unit used to compare the chiroptical activity between different materials regardless of the concentration. It can be calculated using **Equation 2.9**.

5.3 Growth of Static Self-Replicated Structures

The realization of coupled self-replication and self-assembly for abiotic NPs opens the possibility of a minimalistic system with some biological functions. Since organization of NPs into chains utilizes thermal energy, this process is energy efficient. We realized self-replication conditions in the vicinity of surfaces functionalized with three PDDA/PSS bilayers. The initially formed NPs are attracted to the positive charge of the substrate's surface coated with PDDA to create nucleation centers for subsequent chain growth. Illumination of this surface with UV light results in the neuron-like NP networks on the substrate (**Figure 5.1A, B**). The separate islands of the NP networks have apparent similarity with the colony growth observed for bacteria (**Figure 5.1A**).[14] After the deposition of the NP networks, continuous conduction can be obtained via electroless metal deposition, that requires prior deposition of silver particles.

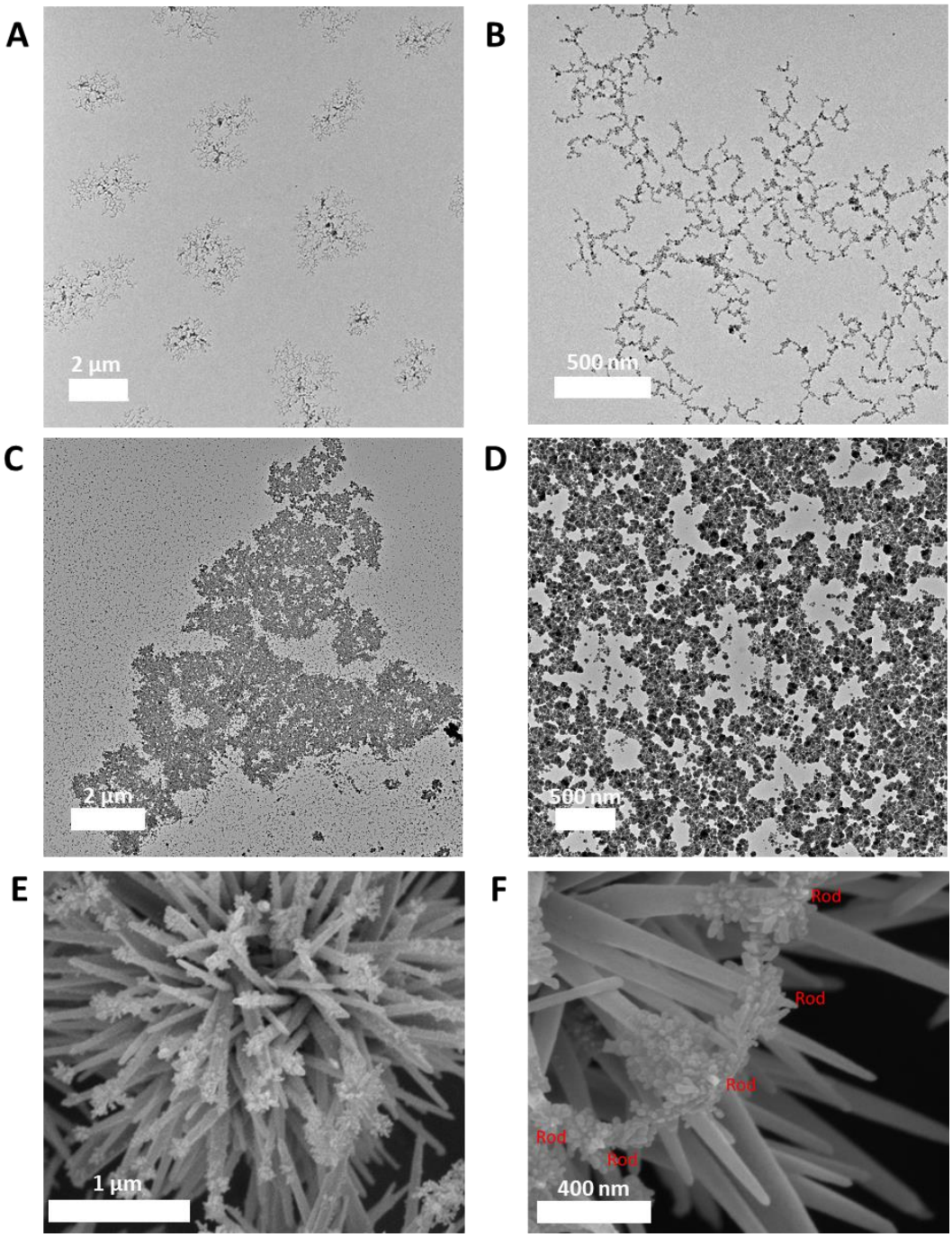

Figure 5.1. Growth of NPs on substrates and electroless silver deposition. (A-B) TEM images of the growth of dispersed self-replicating NP networks on a PSS/PDDA functionalised SiO TEM grid **(C-D)** TEM images of a short 5 min electroless silver deposition on the AgNP networks supported on a PSS/PDDA functionalised SiO TEM grid. **(E)** SEM image of AgNPs self-replicated on ZnO/Fe_2O_3 HPs. **(F)** SEM image of self-replicated AgNPs forming bridges between the ZnO rods.

A control was performed by trying to deposit silver on a PDDA/PSS functionalized glass slide before growing AgNPs on it, and no silver deposition was observed. So, no additional silver

will be grown straight on the substrate or the PDDA/PSS layer. The silver is deposited at a faster rate where there is a higher concentration of AgNPs, which happens to be at each of the networks when soaked in the deposition solution for only 5 minutes (**Figure 5.1C, D).** When soaked for a prolonged period up to 40 minutes, all the islands become connected and create a thin film of silver across the surface of the substrate (**Figure A.16**). Sheet resistance readings were able to be obtained for as low as 60 Ω/sq using a four-point probe.

Self-replication was also performed on highly corrugated surfaces as well. AgNPs were grown on hedgehog particles (HPs) made of iron oxide (Fe_2O_3) cores and zinc oxide (ZnO) spikes.[3] The photocatalytic properties of the ZnO spikes under UV light allowed initial attachment of AgNPs to the tips of the spikes (**Figure 5.1E, Figure A.17**). Silver nuclei form at the interface of the attached AgNPs to allow growth radially outward. As the NPs self-replicate to extend the chain further, they can eventually bridge the gap between to ZnO spikes (**Figure 5.1F**). These suspended bridges of AgNPs on highly corrugated surfaces could have numerous applications in microfluidics, photonic, and sensing. [15]

5.4 Potential Self-Replicating Chiral Materials

As the self-replicating AgNPs self-assemble during the synthesis, we wanted to try and induce some asymmetry into the chains. No chiral molecules are used in the synthesis, so the only way to induce chirality is through CPL. To get a better understanding of how CPL directly transfers chirality from photon to matter, we explored the growth of silver helicoids on substrates using CPL (**Section 3.8.1**). The growth of the silver helicoids was additionally evaluated computationally to confirm how the nucleate and where the chirality of the material comes from. I then took that knowledge from **Section 3.8.1** and incorporated it into the self-replicating system (**Section 3.8.2**).

5.4.1 Chiral Silver Helicoid Metasurfaces

Here, we report the first-ever direct printing of pure metallic nanostructures with 3D chirality on various substrates using light-guided chiral assemblies. Silver helical assemblies were synthesized as described in **Section 5.2.4** (**Figure 5.2A**). For the 532 nm laser with a photon flux of 3.07×10^{21} photons·sec^{-1}·m^{-2}, the silver helicoids were able to be produced on glass slides within 30 minutes. L-CPL and R-CPL were separately used to illuminate the solution to lead to right- and left-handed helicoids, which are denoted here as Δ- and Λ-helicoids, respectively (**Figure 5.2D-F**). When viewed in ambient light, the sample displayed angle-dependent reflective color, which is typical for metasurfaces (**Figure 5.2B, C**). To confirm that the helicoids are chiral and that they are indeed enantiomers of each other, CD spectroscopy was used. The Δ- and Λ-helicoids both displayed strong chiroptical activity with perfectly mirrored peaks at 350, 430, 545, and 780 nm (**Figure 5.2G**).

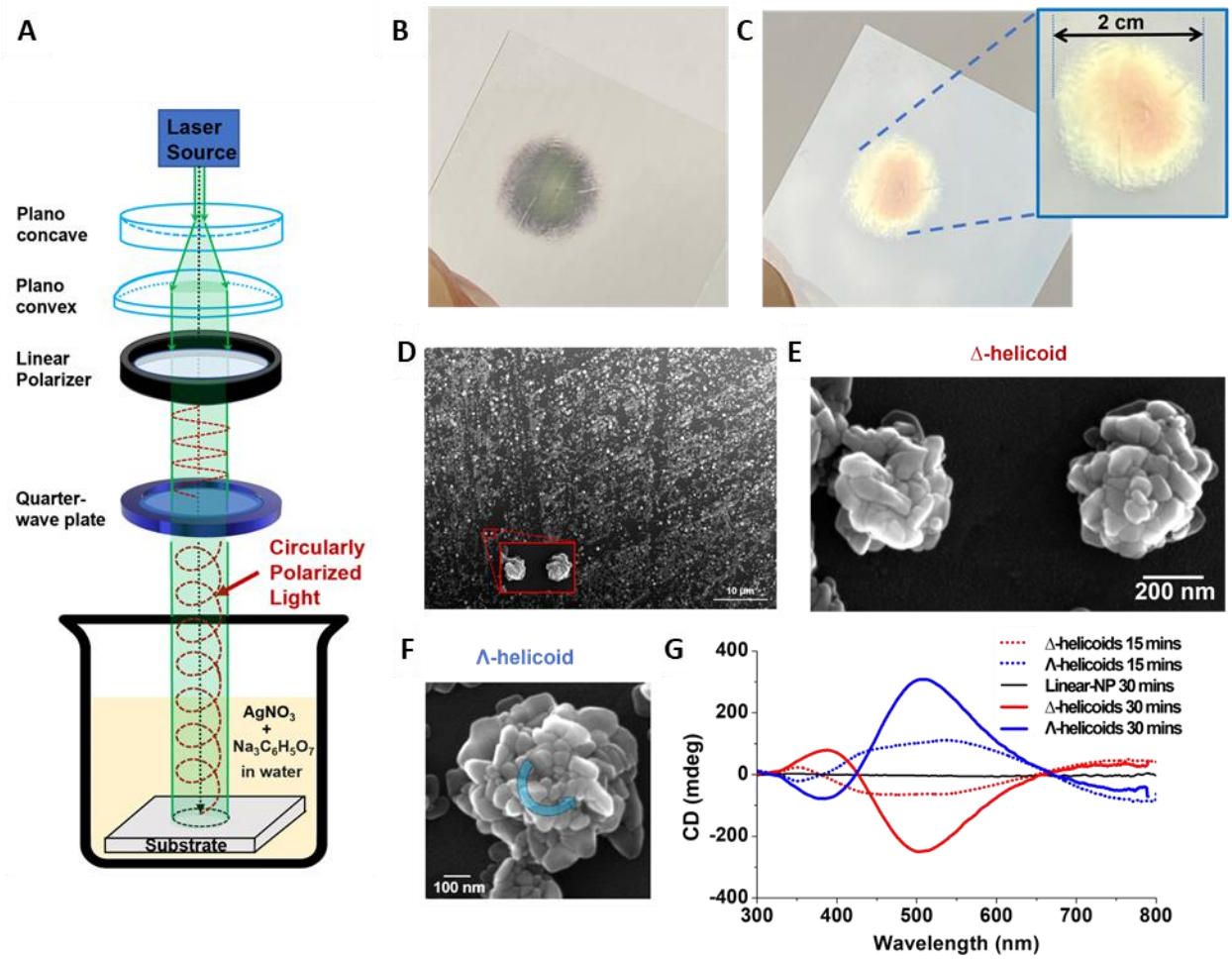

Figure 5.2. Formation of nanostructured silver helicoids with out-of-plane substrate alignment driven by the circularly polarized light (CPL). (a) Schematic description of experimental set up for CPL driven synthesis of silver helicoids **(b, c)** Photograph of silver helicoids deposited on glass substrate in (a) transmissive and (b) reflective angle, respectively. **(d, e)** Scanning electron microscope (SEM) image of Δ-helicoids formed on ITO/glass by *L*-CPL at (d) low magnification and (e) a partial high-resolution image for the red boxed area of (d). **(f)** SEM images of Λ-helicoid. **(g)** CD spectra of Δ- or Λ-helicoids formed on glass substrates after 15- and 30-min exposure to *L*-CPL and *R*-CPL, respectively. Δ-helicoids grow under *L*-CPL and Λ-helicoids grow under *R*-CPL.

To evaluate how these helicoids form, intermittent stages of the growth of the helicoids were imaged in SEM (**Figure 5.3A**). Early stages of the growth (below 5 min) show the formation of single AgNPs (15-20 nm in diameter) on the surface. After 5 min, asymmetric dimers are observed and after 10 min we started to observe assemblies of multiple NPs. STEM imaging of the assemblies at 10 min shows that they form from 5 – 7 NPs in a twisted horseshoe like shape (**Figure 5.3B**). Continuing past 10 min shows that more of the horseshoe like assemblies stack

vertically on top of each other until with are left with the silver helicoids at 30 min reaction time. As more segments stack on each other, we see a red shift in the chiroptical bands (**Figure 5.3C**). After 10 min exposure to CPL we observe the emergence of additional bands at 545 nm and 780 nm.

To better understand how the photon-to-matter chirality transfer induces the formation of these stacking horseshoe segments, a computational model was built using the rendered structure of a single helicoid to evaluate its chiroptical response to the incident CPL. The computational model and its results were developed by Dr. Ji-Young Kim and the model parameters can be seen in **Appendix B**. The computational model is described in this thesis to better convey the experimental results that I contributed too. Renderings of the silver helicoids at each time point during the growth under L-CPL were created (**Figure 5.3D**). Initial modeling of the dimers on a substrate and subsequent calculation of the electromagnetic field with exposure to L-CPL or R-CPL show that there are 'hot-spots' in specific locations (**Figure 5.3E**). These hot-spots differ depending on which polarization of the incident light, and they serve as the attachment points for subsequent site-selective deposition of NPs. The newly added NPs at the hot-spots will dynamically alter the position of the successive hot-spot, and they will always be displaced around the rotational axis of the growing helicoid due to the helicity of the CPL (**Figure 5.3F**). Continuing this computational particle growth, we observed the twisted horseshoe shaped assemblies (**V1** and **V2** in **Figure 5.3D**) that match the experimental results in **Figure 5.3A**. Once the assemblies are formed, we assumed that they begin to stack into vertical multilayers to form the silver helicoids, **V3** and upward in **Figure 5.3D**. Modeling the extinction coefficient (**Figure 5.3G**) from structure **V1** to **V2** show the emergence of two resonance modes at 400 nm and 525 nm similar to that observed for the experimental results at 10 min in **Figure 5.3C**. Stacking two assemblies (**V3**)

show the appearance of two additional peaks at 545 nm and 610 nm (starred in **Figure 5.3G**), which occurs due to inter-layer coupling. This is in agreement with the experimental results and supports why the bands also red-shift with the stacking.

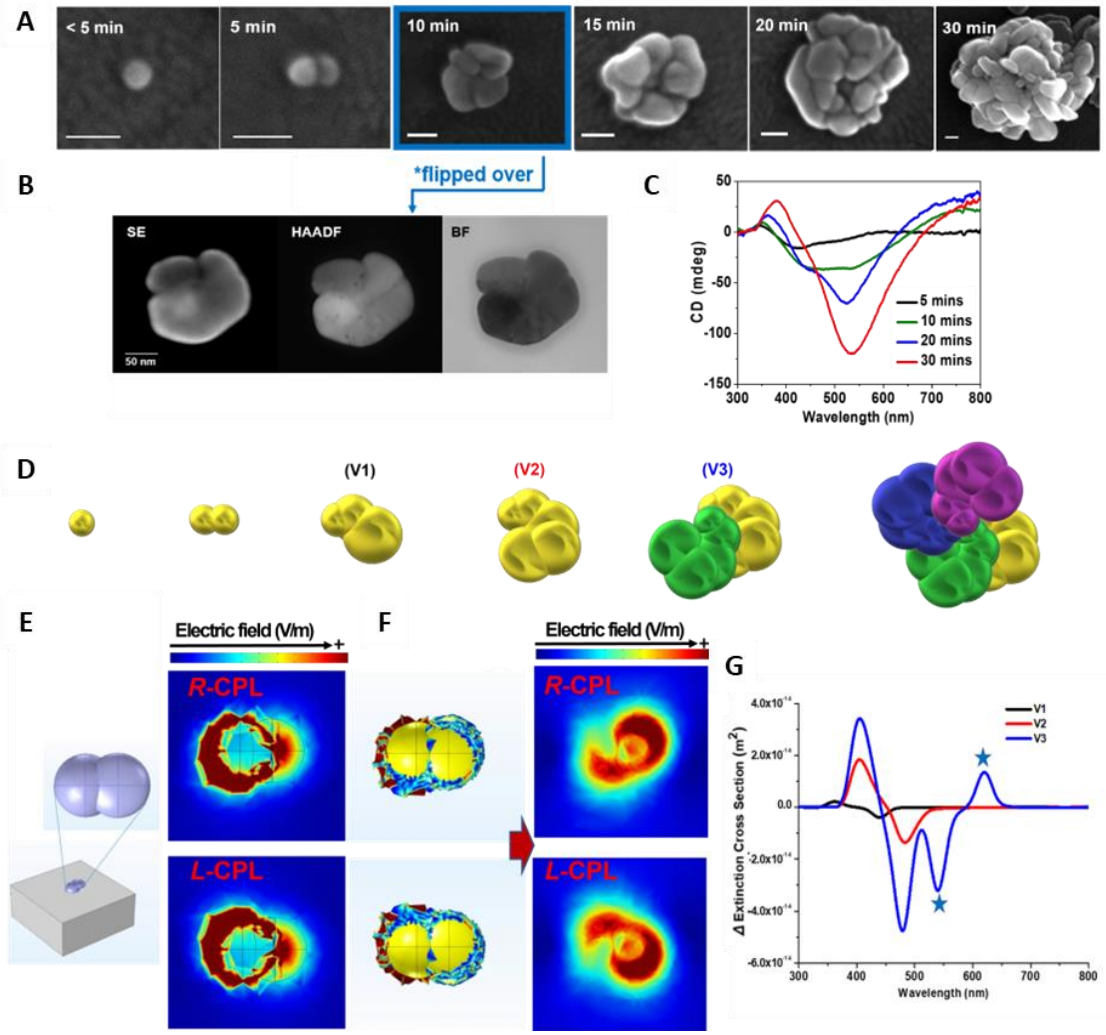

Figure 5.3. Growth transition of Δ-helicoids. (a-c) Experimental observation of different growth stages. (a) SEM images of Δ-helicoids at different illumination times of *L*-CPL. The scale bars are 50 nm. (b) STEM images of Δ-helicoid at 10 min growth stage. Secondary electron (SE), high-angle annular dark-field (HAADF), and bright field (BF) detectors are used simultaneously to see the rotational structure. (c) CD spectra of silver helicoids in different growth stages. (**d-g**) Computational analysis of different growth stages. **(**d**)** 3D computational models built based on electromagnetic simulation of dynamic 'hot spots' under illumination with *L*-CPL for silver deposition and assembly. (e) Dimer model on substrate (left) and asymmetric cross sectional electric field distribution on the dimer under *R*-CPL (top) and *L*-CPL (bottom), respectively. (f) The asymmetric nanostructure model at the next preceding growth stage (left) predicted from the electric field volume plot in (e) and the subsequent cross sectional electric field distribution on it**.** (g) Calculated differential extinction cross section of *L*-CPL to *R*-CPL (Δ Extinction cross section) spectra of the three different models (**V1-3**).

The tunability of the chiroptical response of the helicoids was observed by illumination with different wavelengths of CPL for the synthesis. A 405 nm, 532 nm, and 660 nm laser were used to grow the silver helicoids, and it was observed that the chiroptical bands in their CD spectra showed shifts closer to their wavelength (**Figure 5.4A**). When imaged under SEM, the size of the helicoids was noted to increase with an increase in wavelength. The ability to adjust the handedness, wavelength, and power density of the CPL on-the-fly give this system the possibility to print varying patterns of chiral helicoids onto any surface. To show how versatile of a print system this could be, we printed 24 different grid spots with 1 mm diameter by two-step exposure of different combinations of light source handedness, *L*-CPL or *R*-CPL, and wavelength, 405, 532, or 660 nm (**Figure 5.4C**). The resulting CD spectra showed that their chiroptical spectra can be modulated in the range of the full visible spectrum (**Figure 5.4D, E**).

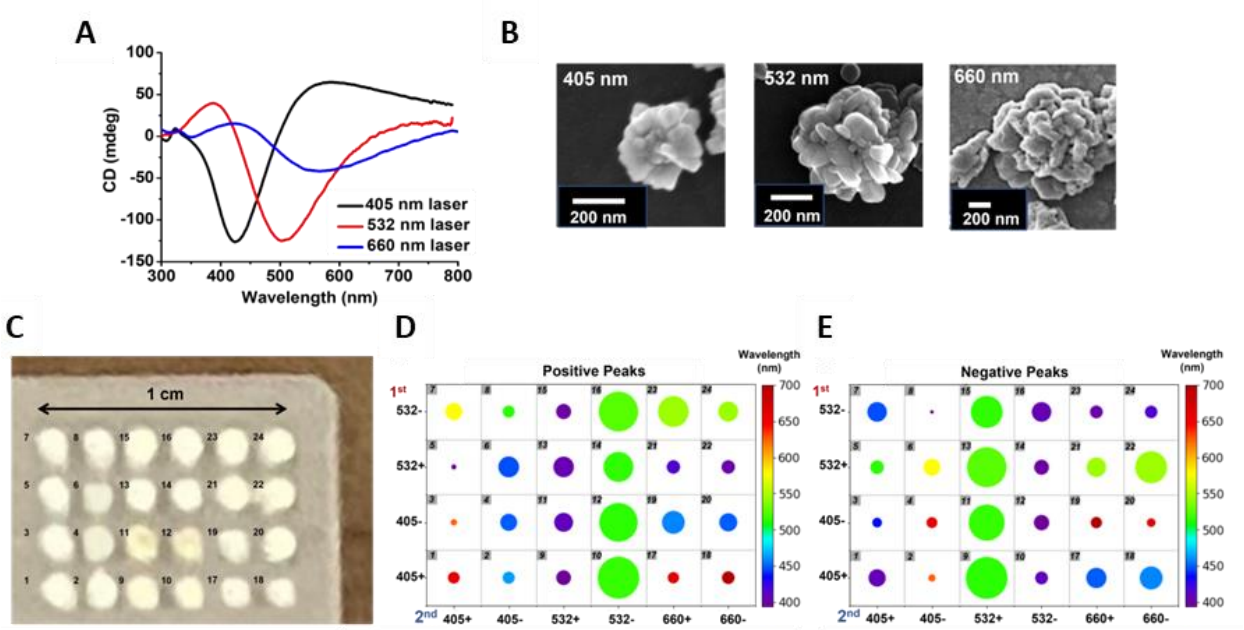

Figure 5.4. Helicoids formed with varying wavelengths of CPL. Experimental **(A)** CD spectra and **(B)** SEM images of Δ-helicoids manufactured under three different wavelengths **(C)** Photograph of miniatured grid patterned library demo with various bi-layered structures manufactured under 24 different combinations of ellipticity and wavelengths of light source. **(D,E)** The color and intensity map of positive (**D**) and negative (**E**) CD peaks of the bi-layered library samples showed in **C** (Legend: *wavelength of CPL* used to manufacture for 1st layer and 2nd layer; + and - corresponds to *L*-CPL and *R*-CPL, respectively; The diameter of bubble plot is proportional to intensity.

To show application of this CPL-induced formation of chiral nanostructures, we developed a direct printing system to rapidly print metasurface patterns. Using a motorized stage that was set up by Dr. Ji-Young Kim to move the laser across the substrate as it is emitting light, we were able to create any pattern on the surface of any substrate (**Figure 5.5A**). A pattern of discrete small dots was initially tested where the beam is parked for 30 seconds before movement to another area on the substrate (**Figure 5.5B**). The beam was focused to a narrower spot size of 0.36 mm (photon flux of 9.48 $x10^{21}$ photons$\cdot sec^{-1} \cdot m^{-2}$) to induce growth of the silver helicoids at a faster rate. Taking it a step further, we demonstrated continuous printing during the movement of the stage (stage moving speed of 1.1 mm/sec) by fabricating two rows of letter patterns with *R*-CPL and *L*-CPL for the first and second row, respectively (**Figure 5.5C**). The strong chiroptical band at 500 nm in the CD spectra from these two rows have opposite signs (**Figure 5.5D**). This fast and simplistic form of chiral printing has not been seen to this date and has the potential for applications, such as polarization encryption and chiral sensing among other areas.

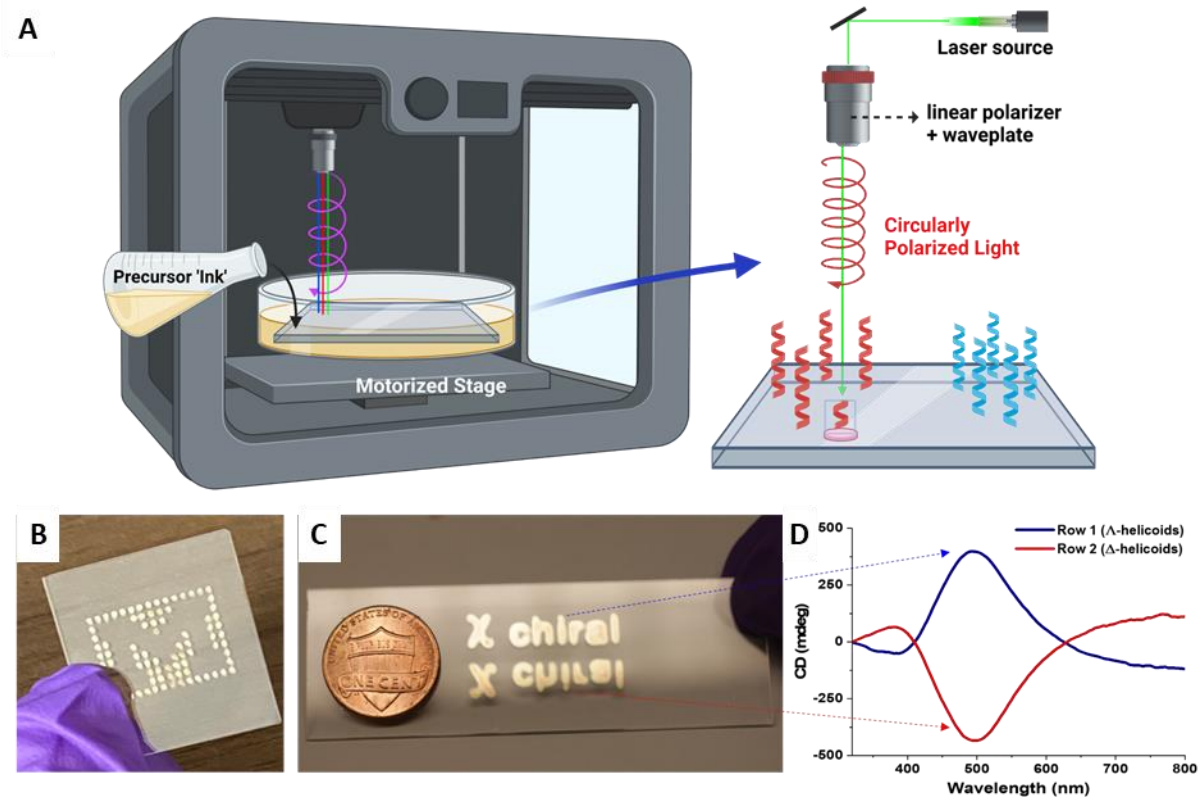

Figure 5.5. Direct printing of chiral metasurfaces. (a) Schematic description of chiral metastructure printing system with motorized stage. **(b)** The photograph of grid pattern on glass substrate. (**c**) The photograph of continuous writing structures formed by *R*-CPL (upper row) and *L*-CPL (lower row) 532 nm laser and their **(d)** CD spectra.

To conclude, we were able to show that the chirality of an incident photon can be successfully transferred to a nanostructure as it is assembled. The fact that we could print a chiral pattern on any surface at ambient conditions on the order of minutes makes this one of the most robust chiral printing systems to date. These metasurfaces can have uses in photonics, optoelectronics, encryption, and electromechanical devices. The knowledge obtained from working on this project will be applied to self-replicating AgNPs in the next section.

5.4.2 Circularly Polarized Light Induced Chirality in Solution

In 2019, members from our lab discovered that CPL could induce asymmetry into the assembly of gold nuclei in solution to create chiral gold nanoparticles.[16] This led us to the belief, along with the capabilities of growing silver chiral structures on surfaces, that CPL illumination

could lead to unique chiral assemblies when paired with the self-replication of AgNPs. Chiral particles were able to be synthesized at self-replicating condition,0.1 mM $AgNO_3$ and 3 mM citrate at pH 10.3, with the addition of a second metallic precursor. Copper nitrate ($Cu(NO_3)_2$) when added at a critical concentration was able to produce chiral bimetallic Ag/Cu NPs. 2.75 mM $Cu(NO_3)_2$ is added to the silver solution and illuminated under either R-CPL or L-CPL for 30 minutes. The solution turns a yellowish color which is indicative out AgNP formation. Analysis with CD spectroscopy gives a set of bands at 360 nm, 400 nm, and 460 nm, where the 400 nm peak has the highest intensity (**Fig 5.4**), which aligns with the plasmonic peak of AgNPs. Alternating from R-CPL to L-CPL gives perfectly mirrored peak in CD, which is evidence that the CPL is the main source of chirality in this system. Running the reaction with linearly polarized light leads to no chiroptical activity further supporting this claim.

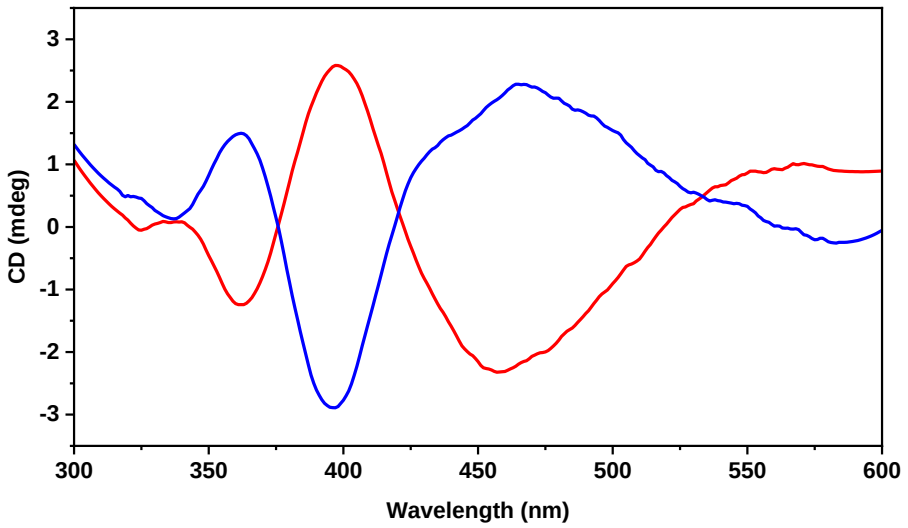

Figure 5.6. Chiroptical activity of Ag/Cu nanoparticles. CD spectra from 300 nm to 600 nm for 0.1 mM $AgNO_3$, 2.75 mM $Cu(NO_3)_2$, 3 mM citrate at ph 10.3 for R-CPL (blue) and L-CPL (red).

Interestingly, when the concentration of $Cu(NO_3)_2$ changes by a magnitude of 0.25 mM, the CD intensity drops by roughly half, and when the concentration is changed by 0.75 mM we see little to no chiroptical activity (**Figure 5.5A**). To explore what is causing this critical

concentration at which chirality is strongest in this system, TEM images were taken at 2 mM, 2.75 mM, and 3.5 mM $Cu(NO_3)_2$ (**Figure 5.5B-D**). At both extremes we see plain NPs with some irregular shape, but at 2.75 mM we observe small 3 – 5 nm NPs surrounding the particle. X-ray spectroscopy was also used on these particles to evaluate whether this is a bimetallic NP or only one of the constituents (**Figure 5.6**). It was determined that the particle is a majority silver with a small fraction of copper. The small NPs are therefore believed to play a part in the chiroptical activity of these particles. It has been proven before that the arrangement of smaller particle around a larger one can have a significant impact on its chirality. [17] Whether the smaller NPs are self-replicating on the larger one is still unknown.

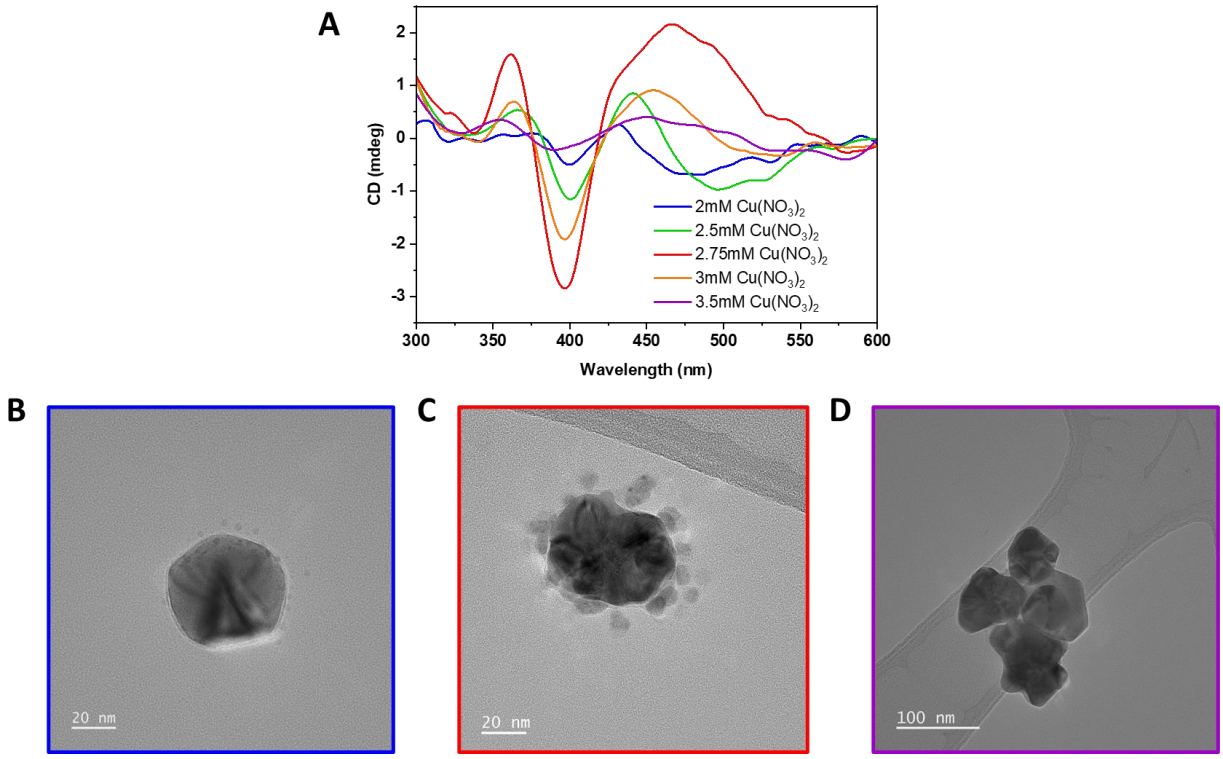

Figure 5.7. R-CPL illumination at different $Cu(NO_3)_2$ concentrations. (A) CD spectra after 30 min illumination. **(B-D)** TEM images of Ag/Cu NPs at 2 mM (**B**), 2.75 mM (**C**), and 3.5 mM (**D**) $Cu(NO_3)_2$ concentrations. Border color correlates to the respective CD spectrum in (A).

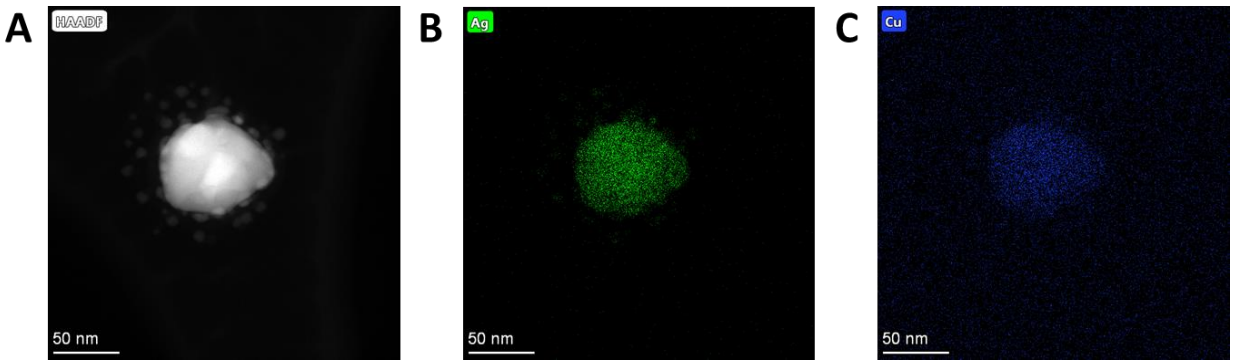

Figure 5.8. EDS elemental mapping of NPs at 2.75 mM $Cu(NO_3)_2$. (A) HAADF STEM image of NP. **(B)** Elemental mapping of silver. **(C)** Elemental mapping of copper.

In conclusion, we were able to apply the self-replicating system to a surface to create neuron-like networks that could be further expanded with electroless deposition to create a thin film for further applications. Additionally, we were able to grow these self-replicating particles on highly corrugated ZnO/Fe_2O_3 HPs, where they favor growing on the tips of the spikes. Interestingly, the AgNPs were able to replicate radially to the point that could create nanobridges connecting to spikes. Bridging to point on a corrugated surface has numerous potential applications. Chirality was also tried to be introduced into the self-replicating system. Silver was first attempted to be grown on a substrate using CPL to induce chirality as the silver nucleates and grows. It was found that the CPL leads to silver helicoids that are highly tunable based off the wavelength and intensity of the light. Knowledge from this system was applied to the self-replicating system, where it was found that Chirality can be induced at self-replicating conditions when Cu ions are introduced into the solution. But there is a critical concentration at which you obtain maximum chirality, and any changes in concentration from there leads to reduction in chiroptical activity until there is none. It was discovered that small 3 – 5 nm NPs surround the larger particles, which it is hypothesized that the specific arrangement of the smaller NPs is what

lead to the chiral signal in CD. Finding where the chirality comes from will be in the future works section of **Chapter 6**.

5.5 References

1. N. A. Kotov, Inorganic Nanoparticles as Protein Mimics. *Science.* **330**, 188–189 (2010).

2. S. Li, J. Liu, N. S. Ramesar, H. Heinz, L. Xu, C. Xu, N. A. Kotov, Single- and Multi-Component Chiral Supraparticles as Modular Enantioselective Catalysts. *Nat Commun*. **10**, 1–10 (2019).

3. A. Kuzyk, R. Schreiber, Z. Fan, G. Pardatscher, E. M. Roller, A. Högele, F. C. Simmel, A. O. Govorov, T. Liedl, DNA-Based Self-Assembly of Chiral Plasmonic Nanostructures with Tailored Optical Response. *Nature.* **483**, 311–314 (2012).

4. J. Cai, W. Zhang, L. Xu, C. Hao, W. Ma, M. Sun, X. Wu, X. Qin, F. M. Colombari, A. F. de Moura, J. Xu, M. C. Silva, E. B. Carneiro-Neto, W. R. Gomes, R. A. L. Vallée, E. C. Pereira, X. Liu, C. Xu, R. Klajn, N. A. Kotov, H. Kuang, Polarization-Sensitive Optoionic Membranes from Chiral Plasmonic Nanoparticles. *Nat Nanotechnol*. **17**, 408–416 (2022).

5. Z. Wang, F. Cheng, T. Winsor, Y. Liu, Optical Chiral Metamaterials: a Review of the Fundamentals, Fabrication Methods and Applications. *Nanotechnology*. **27**, 412001 (2016).

6. K. Sawai, R. Tatumi, T. Nakahodo, H. Fujihara, Asymmetric Suzuki–Miyaura Coupling Reactions Catalyzed by Chiral Palladium Nanoparticles at Room Temperature. *Angewandte Chemie*. **120**, 7023–7025 (2008).

7. Y. Guan, Z. Wang, B. Ai, C. Chen, W. Zhang, Y. Wang, G. Zhang, Chiral plasmonic metamaterials with tunable chirality. *ACS Appl Mater Interfaces*. **12**, 2021 (2020).

8. B. Frank, X. Yin, M. Schäferling, J. Zhao, S. M. Hein, P. v. Braun, H. Giessen, Large-area 3D chiral plasmonic structures. *ACS Nano*. **7**, 6321–6329 (2013).

9. J. K. Gansel, M. Latzel, A. Frölich, J. Kaschke, M. Thiel, M. Wegener, Tapered gold-helix metamaterials as improved circular polarizers. *Appl Phys Lett*. **100**, 101109 (2012).

10. J. Kaschke, M. Wegener, Gold triple-helix mid-infrared metamaterial by STED-inspired laser lithography. *Opt Lett*. **40**, 3986 (2015).

11. D. G. Montjoy, H. Hou, J. H. Bahng, A. Eskafi, R. Jiang, N. A. Kotov, Photocatalytic Hedgehog Particles for High Ionic Strength Environments. *ACS Nano*. **15**, 4226–4234 (2021).

12. E. A. K. Wilson, Design and Application of Surface Corrugated Microparticles for Photocatalysis in Nonpolar Media, Thesis (2022). doi:10.7302/6159.

13. S. Schaefers, L. Rast, A. Stanishevsky, Electroless Silver Plating on Spin-Coated Silver Nanoparticle Seed Layers. *Mater Lett*. **60**, 706–709 (2006).

14. H. Wang, H. Ceylan Koydemir, Y. Qiu, B. Bai, Y. Zhang, Y. Jin, S. Tok, E. C. Yilmaz, E. Gumustekin, Y. Rivenson, A. Ozcan, Early detection and classification of live bacteria using time-lapse coherent imaging and deep learning. *Light: Science & Applications*. **9**, 1–17 (2020).

15. M. Erdmanis, P. Sievilä, A. Shah, N. Chekurov, V. Ovchinnikov, I. Tittonen, Focused ion beam lithography for fabrication of suspended nanostructures on highly corrugated surfaces. *Nanotechnology*. **25**, 335302 (2014).

16. J. Y. Kim, J. Yeom, G. Zhao, H. Calcaterra, J. Munn, P. Zhang, N. Kotov, Assembly of Gold Nanoparticles into Chiral Superstructures Driven by Circularly Polarized Light. *J Am Chem Soc*. **141**, 11739–11744 (2019).

17. A. Qu, M. Sun, J.-Y. Kim, L. Xu, C. Hao, W. Ma, X. Wu, X. Liu, H. Kuang, N. A. Kotov, C. Xu, Stimulation of neural stem cell differentiation by circularly polarized light transduced by chiral nanoassemblies. *Nature Biomedical Engineering*. **5**, 103–113 (2020).

Chapter 6 Conclusions, Future Recommended Works, and Outlook

6.1 Summary and Overall Conclusions

In this dissertation, the overall goal was to develop the first self-replicating system for inorganic nanoparticles. Over 100 systems were tested and evaluated for any indication of self-replicating capabilities. In the end, this was accomplished with silver nanoparticles (AgNPs) under the illumination of UV light with citrate and a critical pH of 10.3. The work on this system provided insight into a new form of non-classical nucleation never realized for inorganic synthesis and expands the range of what self-replication can encompass. The combination of self-replication and self-assembly without agglomeration or coalescence, as seen previously in literature [1], opened another avenue for NP interactions that can lead to more unique material design and synthesis. These self-replicating nanoparticles were grown on substrates to create neuron-like networks of AgNPs a few microns in size. Electroless deposition was used to further connect and expand the networks to create a thin film of NPs, which will have numerous applications in catalysis, optics, sensing, and electrochemistry. The use of silver with its excellent optical, electrical, catalytic, sensing, and antibacterial properties gives rise to even more application in areas such as surface-enhanced Raman spectroscopy (SERS), optical sensors, and photovoltaics. This self-replicating system was also used with circularly polarized light (CPL) to try and develop unique chiral structures from the assemblies formed. Silver nitrate with citrate alone was first evaluated for growth on surfaces using circularly polarized light (CPL). Chiral silver helicoids were found to

grow vertically on the surface. The chiroptical properties of the helicoids could be fine-tuned by change the wavelength, intensity, and handedness to expand the entire visible spectrum. Although the original self-replicating system did not show any form of chirality under CPL, the introduction of a second metallic salt induced chirality in the particles at a critical concentration. Copper nitrate ($Cu(NO_3)_2$) was incorporated into the self-replicating system where it was discovered that chiral bimetallic Ag/Cu NPs could be formed. It is believed that the chirality stems from the orientation of the smaller NPs on the larger ones. These chiral materials have the potential for a variety of applications from chiral sensing to chiral catalysis due to their strong optical and catalytic properties.

In **Chapter 3**, we developed a high-throughput screening system consisting of three steps to evaluate over 100 inorganic systems for indications of self-replication. The first step was to visually observe any precipitation or color change in the absence of light for 24 hours. As we desired light to be the energy source to induce self-replication, it is paramount that no particles form without it. This was the simplest step and helped narrow down the number of potential candidates significantly. The second step was to evaluate the concentration of AgNPs over time where we looked for a sigmoidal, or S-shape curve, that is a characteristic trait of autocatalytic systems and hence that of self-replication. This was done using UV-Vis spectroscopy as the intensity of the plasmonic peak is roughly correlated to the concentration of NPs, though not perfectly. UV-Vis spectroscopy is extremely quick to run versus other more accurate techniques, so it allows quicker analysis of the systems. The third and final step is to analyze the NPs under transmission electron microscopy (TEM) to evaluate their shape and size over time. This is to help account for the faults of only using UV-Vis as the extinction spectra is also impacted by the size and shape of plasmonic nanoparticles. Not all systems could be shown here, but various examples

of systems that did not pass each step were provided for clarity. In the end, it was found that citrate as both the reducing agent as well as the stabilizer at a pH of 10.3 was found to be the only system that passed each step in the screening system.

In **Chapter 4**, the potential self-replicating system of silver nitrate ($AgNO_3$) with citrate at a critical pH of 10.3 was further explored. Using a variety of ex-situ and in-situ characterization techniques, it was found that the AgNPs are indeed self-replicating. With a combination of self-replication and self-assembly, 'parent' AgNPs were shown to induce nucleation of new 'daughter' AgNPs at their interface in a chain-like fashion. Unlike other heterogeneous nucleation seen in literature, where the particles agglomerate or coalesce, this self-replication led to individual AgNPs that eventually separate into their own entities.

In **Chapter 5**, we explored various applications for these self-replicating AgNPs. The AgNPs were grown on a substrate where it was found that they propagate across the surface in a neuron-like fashion as they self-replicate. As the individual networks do not connect, electroless deposition was performed to connect all the networks to create a thin film of AgNPs. The self-replicating AgNPs were also ran under CPL to explore whether we could induce asymmetry in the structure of the assemblies that form. Although no chirality was found in the self-replicating system under CPL, we discovered that the introduction of coper nitrate ($Cu(No_3)_2$) lead to unique bimetallic Ag/Cu NPs that showed chirality. It is believed that the chirality comes from the orientation of the smaller NPs on the larger on, as this has been seen in literature to induce chirality. Further analysis must be done to fully determine where the chirality truly comes from, whether it is indeed the orientation of the smaller particles or if it is the geometrical structure of the larger particles.

6.2 Future Directions

The work in this dissertation established the first self-replicating inorganic system. As a result, there are a large variety of pathways that one can go from these findings. These future works are broken down into two categories: **Section 6.2.1** will provide insight into other inorganic systems that could also have self-replicating capabilities. **Section 6.2.2** will explore future applications that inorganic self-replication can be used for.

6.2.1 Additional Inorganic Self-Replicating Systems

The self-replication of silver nanoparticles is just the tip of the iceberg for inorganic systems. If one system can show self-replicating characteristics, then there must be other systems out there. It is recommended that other plasmonic nanoparticles be explored for self-replication. Copper should be the next metal to explore as the most common precursor used is copper nitrate ($Cu(NO_3)_2$) , and copper ions are known to complex with halides to create photosensitive complexes in solution similar to silver. Spherical copper nanoparticles have a plasmonic peak around 500 to 600 nm [2], so UV light will probably not work in the same manner as that for silver. It is suggested that copper be evaluated in the same manner as that for silver, but with a different wavelength of light for the energy source. Another promising plasmonic metal would be gold as it is the most widely researched of all plasmonic nanoparticles. The common gold precursor comes in the form of chloroauric acid ($HAuCl_4$), which is not similar to that of silver or copper. As a result, it is expected that a whole different system will be expected for gold, so the high-throughput screening system from **Chapter 3** will have to be utilized here. There are numerous other plasmonic metals, such as Al, Mg, and Pt, that can also be explored [3], but it is recommended to start with copper and gold in that order. As we have seen in **Chapter 5**, bimetallic nanoparticles

are also able to be formed under light illumination. This would be the next step as bimetallic metals would have properties of both materials, giving more applications.

Self-replication of spherical silver nanoparticles is probably not the only shape that can self-replicate. Many bacteria in the world that replicate are rod-like shaped. [4,5] Silver nanorods can be synthesized quite easily.[6] Plasmonic nanorods are unique due to their bimodal plasmonic optical response from the longitudinal and transverse plasmon modes. This would be another pathway to further expand this work.

6.2.2 Further Applications for Inorganic Self-Replicating System

Self-replication on surfaces has only been shown to be possible in this dissertation and no applications have tested out with the material other than showing that the thin films can hold a current. The substrates should be tested for various applications like catalysis, sensing, and photovoltaics. The self-replicating nanoparticles in theory can be grown on any substrate with enough fine tuning of the surface. It is recommended that the surfaces be tested for electrocatalytic capabilities, especially if they can be grown on glass carbon, which is commonly used in electrochemical cells. Additionally, the unique optical properties of the replicated structure can be used for sensing capabilities and even surface-enhanced Raman spectroscopy (SERS).

The chiral particles that were synthesized with silver and copper have been hypothesized where the chirality comes from based off literature [7], but it has never been thoroughly explored. It is recommended that topographical reconstructions of the particles be created and computationally analyzed to evaluate where the chirality comes from, whether it is arrangement of particles or the geometrical structure of the particles. Understand the fundamentally can help to fine tune the structures as well as give better understand to hopefully apply this method to other bimetallic materials.

6.3 References

1. Y. Cheng, J. Tao, G. Zhu, J. A. Soltis, B. A. Legg, E. Nakouzi, J. J. de Yoreo, M. L. Sushko, J. Liu, Near surface nucleation and particle mediated growth of colloidal Au nanocrystals. *Nanoscale*. **10**, 11907–11912 (2018).

2. L. V. Q. Garrido, J. M. Gonçalves, J. C. Rocha, E. L. Bastos, H. E. Toma, V. M. Zamarion, Intriguing Plasmonic and Fluorescence Duality in Copper Nanoparticles. *Plasmonics*. **15**, 1213–1219 (2020).

3. A. N. Koya, X. Zhu, N. Ohannesian, A. A. Yanik, A. Alabastri, R. P. Zaccaria, R. Krahne, W.-C. Shih, D. Garoli, Nanoporous Metals: From Plasmonic Properties to Applications in Enhanced Spectroscopy and Photocatalysis. *ACS Nano*. **15**, (2021).

4. L. K. Harris, J. A. Theriot, Relative rates of surface and volume synthesis set bacterial cell size. *Cell*. **165**, 1479–1492 (2016).

5. I. Soifer, L. Robert, A. Amir, Single-cell analysis of growth in budding yeast and bacteria reveals a common size regulation strategy. *Current Biology*. **26**, 356–361 (2016).

6. S. Mukherji, S. Bharti, G. Shukla, S. Mukherji, Synthesis and characterization of size- And shape-controlled silver nanoparticles. *Physical Sciences Reviews*. **4**, (2019).

7. A. Qu, M. Sun, J.-Y. Kim, L. Xu, C. Hao, W. Ma, X. Wu, X. Liu, H. Kuang, N. A. Kotov, C. Xu, Stimulation of neural stem cell differentiation by circularly polarized light transduced by chiral nanoassemblies. *Nature Biomedical Engineering.* **5**, 103–113 (2020).

Appendices

Appendix A Self-Replicating System Additional Information

This Appendix contains additional graphs and notes for **Chapter 4** and **Chapter 5, Section 5.3** from the publication currently in submission: McGlothin, Connor and Kotov, Nicholas. "Coupled Self-Replication and Self-Assembly of Inorganic Nanoparticles" Science (2023)

Full UV-Vis spectrum and additional observations

The solution of 0.1 mM silver nitrate ($AgNO_3$) and 3 mM sodium citrate dihydrate (citrate) at a critical pH of 10.3 was illuminated under 365nm UV light with an intensity of 1.3mW/cm^2 to induce nucleation and self-replication of the AgNPs. The concentration of the silver precursor was chosen so that the final concentration of plasmonic AgNPs does not saturate the UV-Vis spectrometer throughout the entire synthesis. The UV-Vis spectrum was obtained for wavelengths from 190 to 1100 nm. Only two peaks were observed (**Figure A.1A**). The peak around 400 to 420 nm is the plasmonic peak of the spherical AgNPs, while the peak at 200 nm is from the citrate in the solution. The max wavelength was observed to shift slightly to a higher wavelength, but then steadily blue-shift down to 403 at 180 min (**Figure A.1B**).

The kinetic curve of the extinction intensity over time displayed three distinct feature:[1] (1) a slow initial homogeneous nucleation over the first 30 min, (2) an increase in nucleation rate as the initial NPs begin to self-replicate, and (3) a decrease in the rate of nucleation at 150 min upon depletion of the silver precursor.

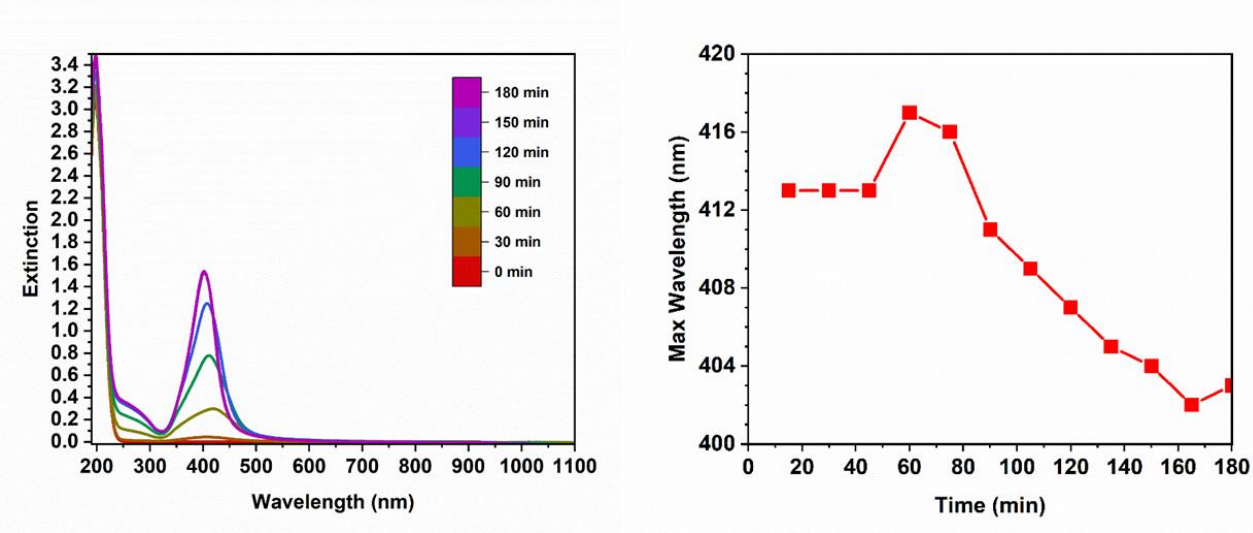

Figure A.1. UV-Vis spectroscopy of self-replicating silver nanoparticles. (A) Full extinction spectrum obtained from UV-Vis spectroscopy for every 30 min during the synthesis. **(B)** Max wavelength of extinction spectra plotted over time.

Effects of pH on system

When trying to find the critical point for self-replication, various pH levels were tested. The extinction intensity at max wavelength was measured at 30 min intervals up to 180 min, where pH 10.3 goes to completion (**Figure A.2**). At pH 10.3, there is an incubation period up to 30 min where homogeneous nucleation of AgNPs is occuring slowly followed by a rapid increase in extinction intensity up to 150 min as heterogeneous self-replication is occuring leading to an s-shape curve in extinction over time. At pH 9.5, it is observed that there is a similar incubation period as that of pH 10.3, but it is followed by a constant linear increase in extinction intensity after 30 min. A similar trend to pH 9.5 can be seen for pH 8.3, but at an even slower rate of nucleation. It should be noted that pH 8.3 is without any addition of NaOH to the solution. As a result, pH levels below 10.3 do not show an s-shape curve that is a preliminary indicator of self-replication for the system. It is thought that pH 8.3 and 9.5 follow a continuous homogeneous nucleation mechanism

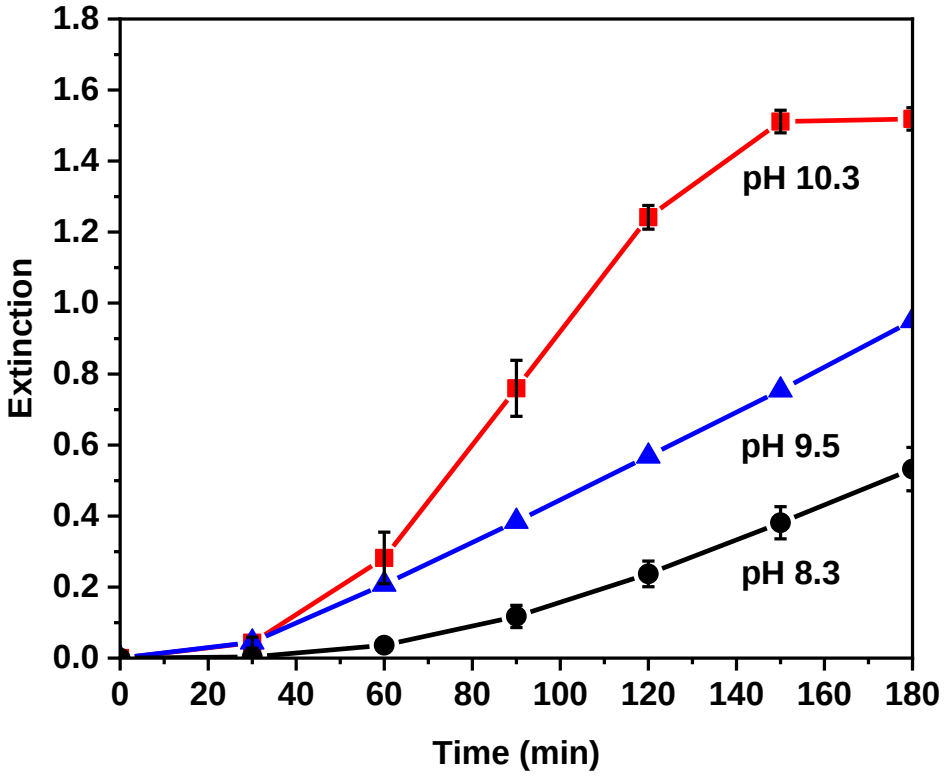

Figure A.2. Extinction intensity at max wavelength of UV-Vis spectrums for pH levels 8.3 (black), 9.5 (blue), and 10.3 (red). Each system was analysed at 30 min time intervals up to 180 min.

Average AgNP Diameter Over Time

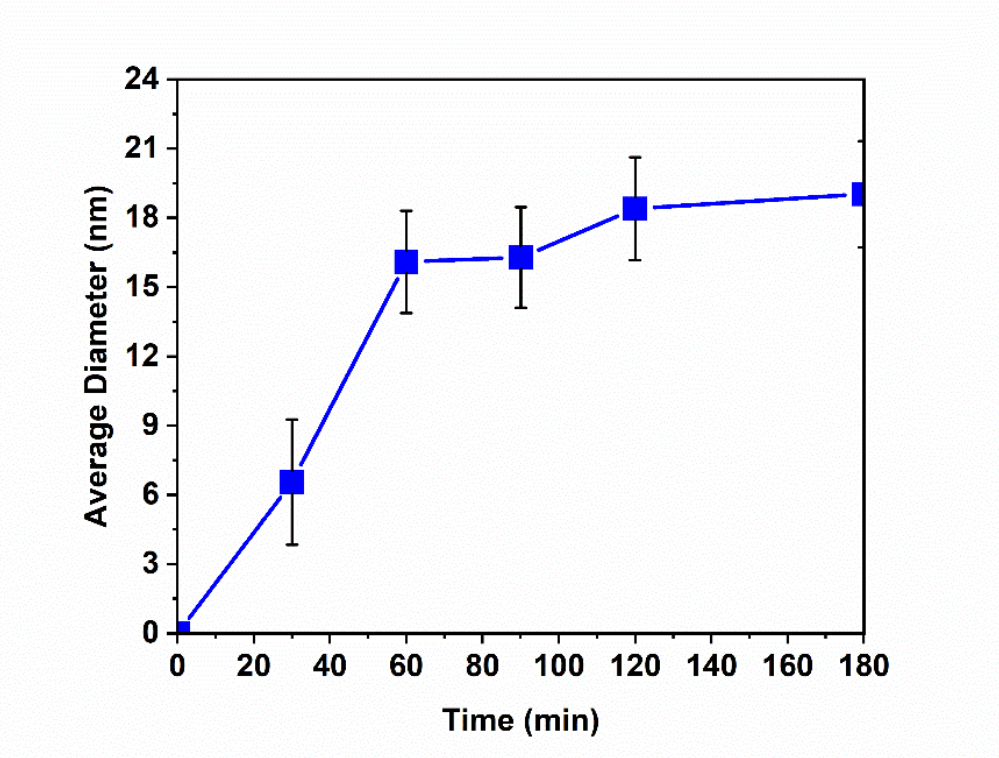

Figure A.3. Plot of AgNP average diameter over time. Average diameters were measured for over 100 NPs at each time point. Scale bars for TEM images are 50 nm

Blue-shift in extinction peak over time

To account for the blue-shift in max wavelength over the course of the synthesis, a post synthesis technique was used. The solution of AgNPs after 180 min of synthesis were analysed using UV-Vis spectroscopy where the max wavelength is 405 nm (**Figure A.4A**). 0.1 mM $AgNO_3$ is added to the post-synthesis solution and the extinction spectrum is measured. No shift in the max wavelength is observed. The solution is then exposed under UV light for 10 min to "reactivate" the self-replicating AgNPs. The extinction spectrum is seen to red-shift to 411 nm as the silver ions start to reduce to silver atoms in the electron double-layer of the AgNPs leading to a lower electron density of the AgNPs. This decrease in electron density is what leads to the red-shift in wavelength.[2] To further confirm that the electron density changes are what is leading to

the max wavelength shifts, the “reactivated” solution of AgNPs is centrifuged at 12,500 rpm for 20 min to remove any excess silver ions in solution and the solution is redispersed in a 3 mM citrate solution to maintain similar conditions to the 180 min post-synthesis solution. Max wavelength of the redispersed solution remained at 411 nm. Finally, the redispersed solution is exposed to UV light for 15 min to react any residual silver ions within the electron double-layer of the AgNPs. As one would expect, the max wavelength shifts back to 405 nm, similar to that of the post-synthesis solution. This is due to an increase in the electron density of the AgNPs as there is no more silver ions to reduce in the electron double-layer. TEM images of the AgNPs at the start end end of this technique were taken to show that there is no size changes throughout the process that could have lead to any wavelength shifts (**Figure A.4B**).

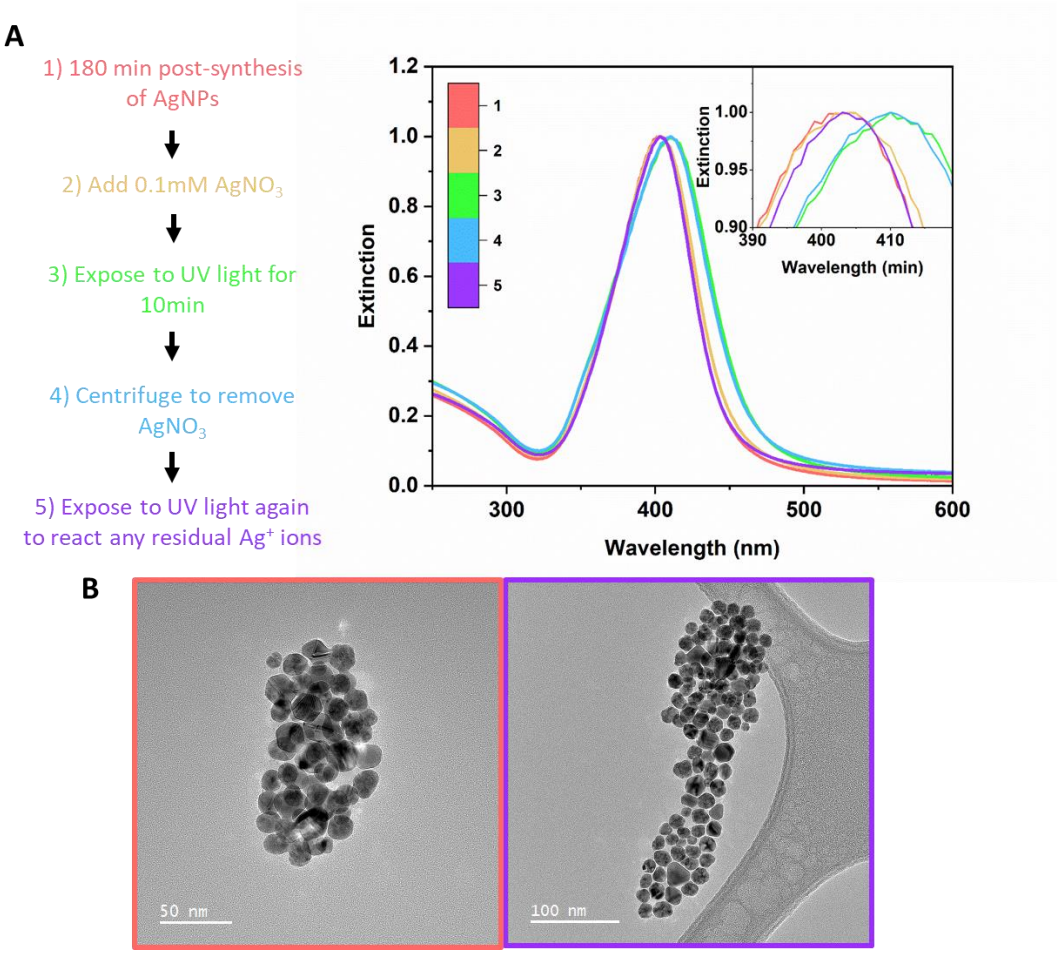

Figure A.4. Blue-shift in extinction peak over time. (**A**) Shift in max wavelength of extinction due to electron density of AgNPs changing during the synthesis. All extinction spectra are normalized to 1 to show a clearer comparision of the wavelength shift. (**B**) TEM images of AgNPs at the start (1) and end (5) of the post-synthesis analysis. Border color matches between each TEM image and the extinction spectrum.

Zeta-potential

The zeta-potential of the solution post-synthesis was analyzed using a Malvern Zetasizer Nano ZSP. The distribution was shown to be fairly large as seen in **Figure A.5A**. The average zeta potential was found to be -31.7±32.0 mV. To check whether this is a common surface charge for AgNPs of our size, which is roughly 14-18 nm, 20 nm citrate-stabilized AgNPs were purchased from Sigma-Aldrich (0.02 mg/mL in aqueous citrate buffer, Cat.# 730793). The zeta-potential distribution of these monodisperse 20 nm AgNPs was shown to be more narrow and had an average

potential of -38.8±12.1 mV (**Figure A.5B**). This difference in distribution, but fairly similar average potential, indicates that there are more complex structures at play in our system which is further analyzed in the main text.

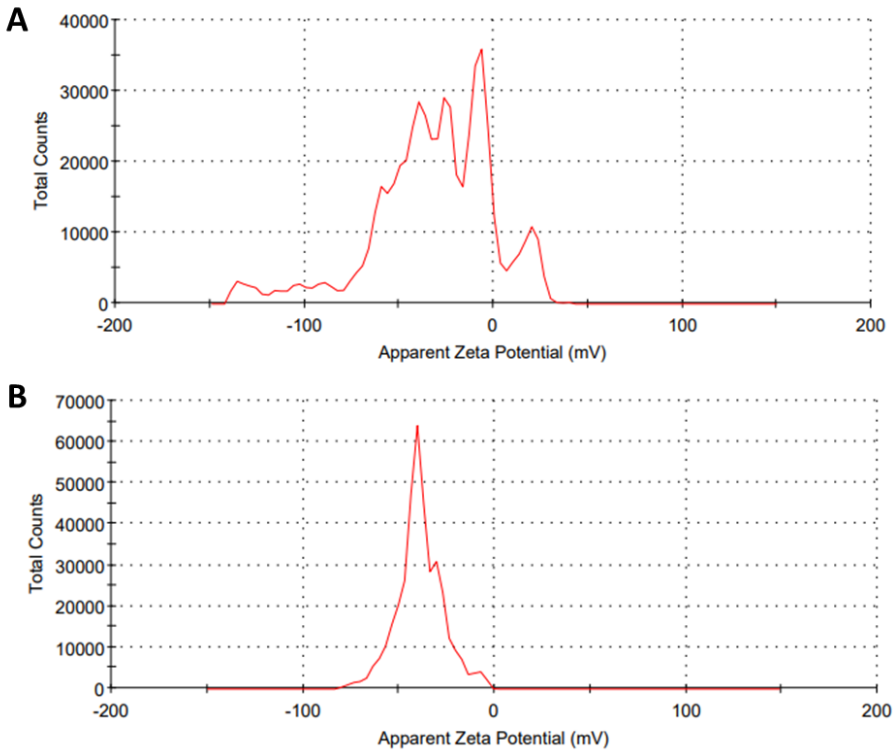

Figure A.5. Zeta-potential of silver nanoparticles. (**A**) Zeta-potential (mV) distribution of post-synthesis self-replicating AgNPs. (**B**) Zeta-potential disctribution of purchased monodisperse 20 nm AgNPs

Dark-field microscopy

Dark-field microscopy was used as a preliminary method to view the synthesis of the AgNPs in real time (**Figure A.6A**). It is seen that particle nucleation starts off slow until 45 sec into the synthesis where nucleation starts to rapidly increase. The short incubation period and faster nucleation is due to the higher intensity light and thinner solution that is being observed. Some particles can be seen at time 0 as the light source is needed to focus the microscope before the synthesis begins, which is unavoidable. The light leads to premature nucleation, but analysing the count of AgNPs overtime (**Figure A.6B**), one can see that the premature nucleation does not reach

the end of the incubation period and as a result does not effect the overall conclusions from this experiment. It can also be seen from the count of AgNPs within the viewing area that we once again see an s-shape curve over time until the viewing screen reaches saturation. Another important discovery from this microscopy is that upon zooming in on the synthesis at multiple points we observed chain-like assemblies of the AgNPs (**Figure A.6C**). These potential assemblies can be a major contribution in confirming that the AgNPs are self-replicating.

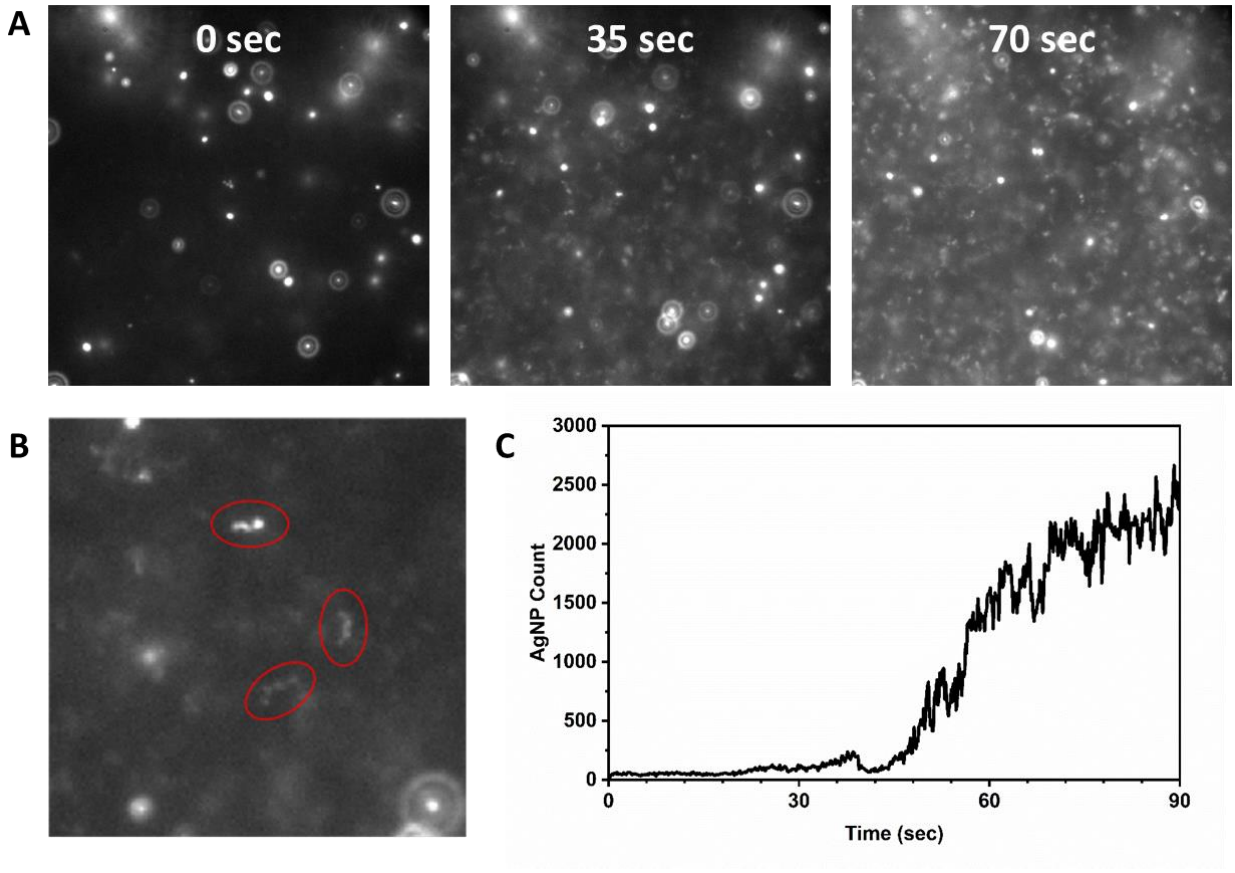

Figure A.6. In-situ viewing of self-replicating AgNP formation via dark field microscopy. (**A**) Dark field microscopy stillshots at 25 sec intervals during the synthesis. (**B**) Close up of chain like formations, circled in red in, during the synthesis. (**C**) Tracking of the number of AgNPs/chain assemblies over time.

Moment-in-time capture of chain-like assemblies

TEM grids were functionalized with a layer-by-layer deposition of PSS and PDDA. The purpose of this method was to prevent any drying effects on the TEM grid and capture the

interaction between NPs as they continue to self-replicate. The positive charge of the final PDDA layer allows the attraction of the negatively charged NPs to its surface when it is submerged in the illuminated solution. Various chain-lengths of AgNPs as they are self-replicating can be seen when captured on the PSS/PDDA functionalized TEM grids at the 60 min point of the synthesis. It was observed that there is a mixture of dimers all the way up to chains of 9 AgNPs (**Figure A.7**). This can be attributed to a plethora of reasons from AgNPs that are still forming from homogeneous nucleation and AgNPs that are not at the critical size for self-replication to chains also breaking apart as they become longer.

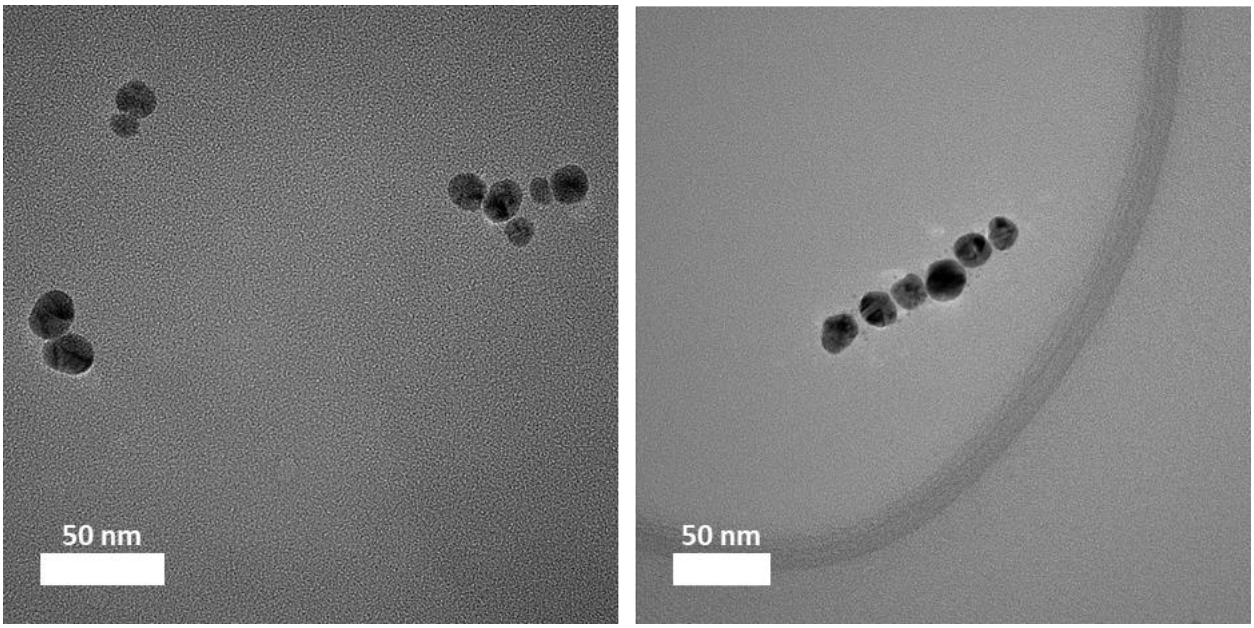

Figure A.7. Additional TEM images of NPs of various chain lengths on PSS/PDDA functionalized TEM grids.

Distance Between Particles in Chains

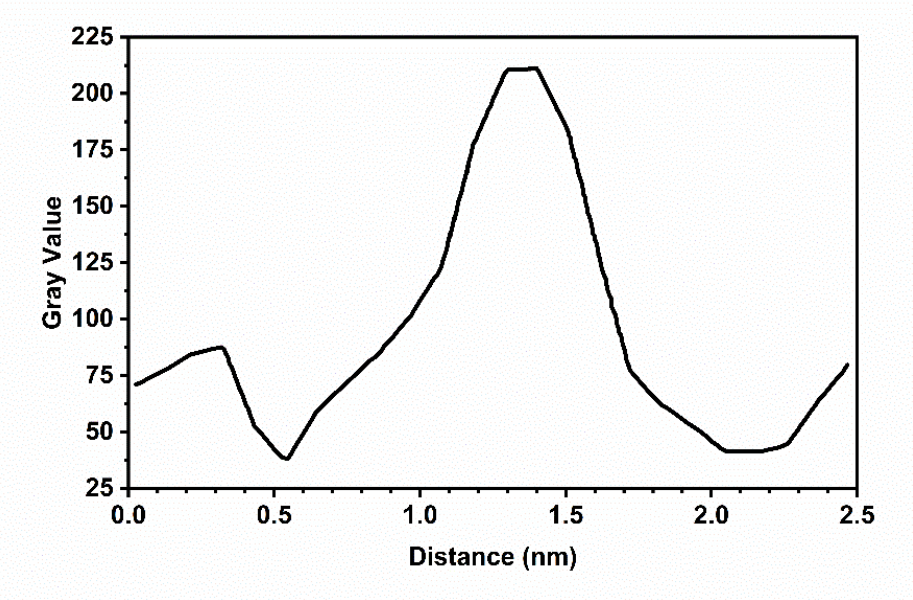

Figure A.8. Gray value over the distance between two AgNPs in one of the assemblies in Figure 4.1E.

Measuring Size of Nuclei at Interface

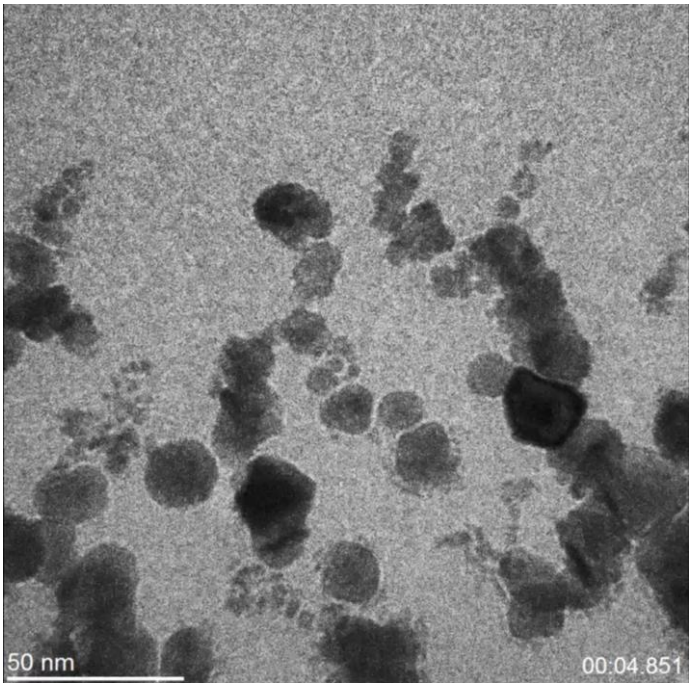

Figure A.9. Liquid TEM viewing of silver nuclei formation at interface of other nanoparticles. Still-shot of self-replicating AgNPs under Liquid TEM when electron dosage is 200 e^-/Ås leading to instability of the nuclei at the interface of NPs.

Liquid TEM at non self-replicating conditions control experiment

To confirm that the AgNPs are indeed self-replicating, the pH was not adjusted with NaOH (pH 8.3) to observe the nucleation at conditions where self-replication was not seen under UV-Vis spectroscopy. Liquid TEM was used to observe this control experiment (**Figure A.10**). Electron dose rate was kept at 130 e^-/Ås to maintain the same TEM conditions used for the self-replication system at pH 10.3. AgNPs were seen to slowly nucleate on the surface of the Liquid TEM windows, but no self-replication or chain-like assemblies were observed showing that the mechanism at pH 8.3 is different.

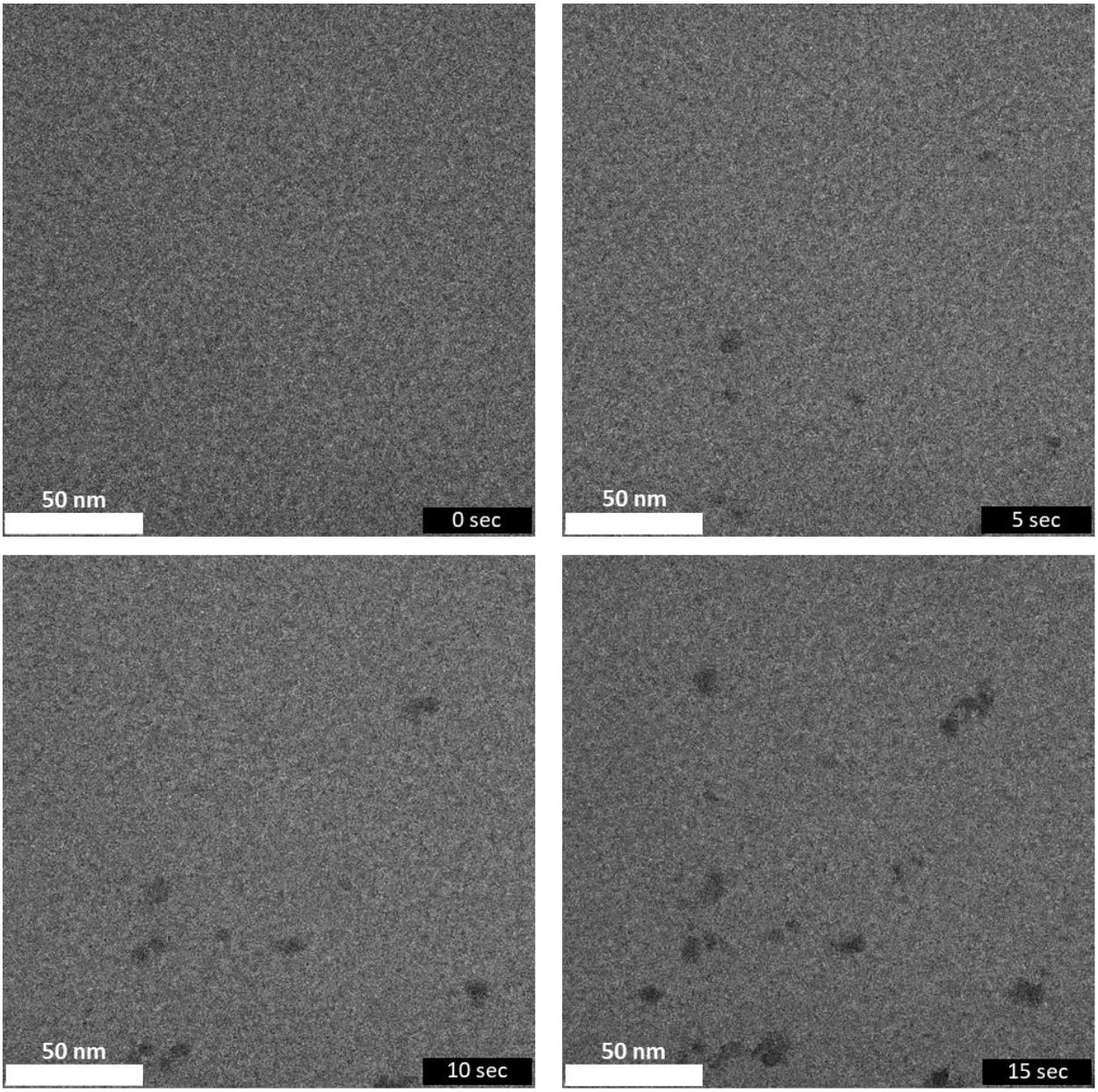

Figure A.10. Liquid-phase TEM control experiment with no NaOH to show how nucleation and growth occurs when not under self-replicating conditions.

Fitting of Fink-Watzky mechanism to self-replicating system

Trying to fit our experimental data to the two-step continuous nucleation and autocatalytic growth Finke-Watzky model (**Equation 4.1,4.2**) shows that this model does not accurately describe our results (**Figure A.11**). The rate contants k_1 and k_2 values are 2.01×10^{-6} and 3.25×10^{-20}, respectively. As the Finke-Watzky mechanism only accounts for continuous nucleation, it will

not be able to account for an increase in nucleation rate over time and therefore cannot correctly portray an s-shape curve in concentration of NPs over time.

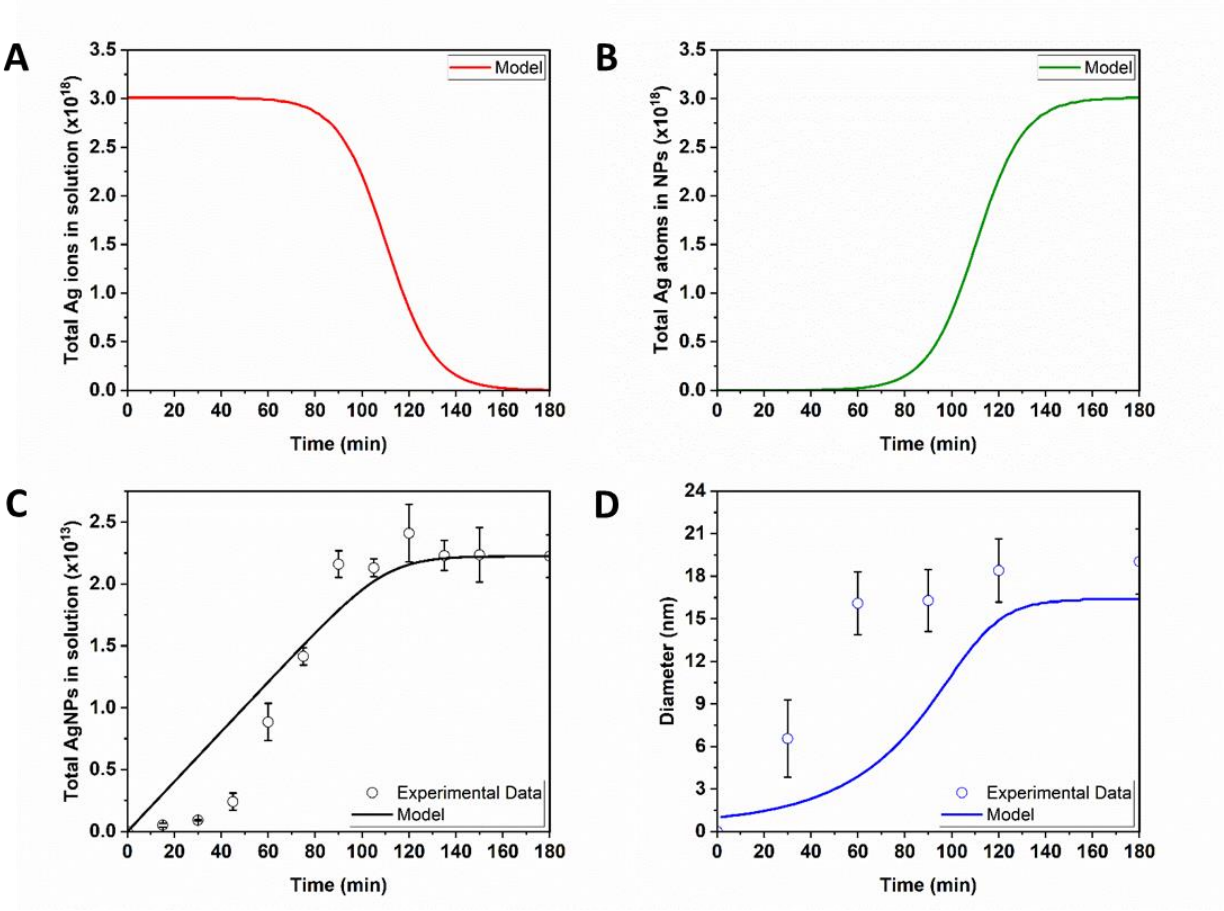

Figure A.11. Fitting experimental data to Finke-Watzky model. (A) Theoretical concentration of Ag^+ ions in the solution over the course of the synthesis the from the Finke-Watzky model **(B)** Theoretical total number of Ag^0 atoms in all AgNPs over the course of the synthesis from the Finke-Watzky model **(C)** fit of the Finke-Watzky model (line) to the experimental AgNP concentration (hollow circles) over time **(D)** fit of the Finke-Watzky model (line) to the experimental average AgNP diameter (hollow circles) over time.

Additional notes and figures on self-replicating kinetic model

Due to the poor overal fit of the Finke-Watzky model to the NP concentration over time, it was determined that our system does not follow only continuous nucleation and instead a different mechanism. The kinetic model developed in this work is a modification of the two-step Finke-Watzky method and the chemical equation can be seen in the main body of the article (**Equation 4.1 and 4.2**). In these equations, Ag^+ is the silver ions from the precursor $AgNO_3$, Ag^0 are reduced

silver ions that are part of a formed AgNP nuclei, Ag^0_{surf} are the silver ions on the surface of the AgNPs, and N are the AgNPs that are capable of self-replication. The differential equations that arise from these chemical equations are:

$$\frac{dAg^+}{dt} = -k_1 Ag^+(t) - k_2 Ag^+(t) Ag^0_{surf}(t) - k_3 Ag^+(t) N(t) \tag{A.1}$$

$$\frac{dAg^0}{dt} = k_1 Ag^+(t) + k_2 Ag^+(t) Ag^0_{surf}(t) + k_3 Ag^+(t) N(t) \tag{A.2}$$

$$\frac{dN}{dt} = \frac{k_1 Ag^+(t) + k_3 Ag^+(t) N(t)}{m} \tag{A.3}$$

Here, Ag^+ is the silver ions from the precursor $AgNO_3$, Ag^0 are reduced silver ions that are part of a formed AgNP nuclei, Ag^0_{surf} are the silver ions on the surface of the AgNPs, N are the AgNPs that are capable of self-replication, m is the smallest stable silver nuclei from thermodynamic theory (~30 atoms), and t is time. For calculation of average diameter and total bulk/surface atoms in all AgNPs over the course of the reaction, these equations are used:

$$D = \sqrt[3]{\frac{6(Silver\ Atoms\ in\ AgNPs)M_w}{\pi(Number\ of\ AgNPs)\rho N_A}} \tag{A.3}$$

$$D_{bulk} = D - 4R_{Ag} \tag{A.4}$$

$$Ag^0_{bulk} = \frac{\pi D^3_{bulk} \rho N_A}{6M_w} N(t) \tag{A.5}$$

$$Ag^0_{surf} = Ag^0_{tot} - Ag^0_{bulk} \tag{A.6}$$

Where D is the average diameter of the AgNPs, M_w is the molecular weight of silver (107.868 g/mol), ρ is the density of silver (10.49 g/cm^3), N_A is avogadro's number, D_{bulk} is the diameter of a AgNP beneath the surface atoms, R_{Ag} is the radius of a silver atom (0.165 nm), and Ag^0_{bulk} is the total atoms in an AgNP minus the surface atoms. Experimental results were fitted to this model using Matlab and its lsqcurvefit function. Fitting of the model to experimental AgNP

concentration and average diameter for each light intensity (1.3, 8, and 17.2 mW/cm^2) can be seen in the main text (**Figure 4.3**). The rate constants differ significantly from their biological counterparts, such as the budding yeast[3–5], which is expected due to the differing size scale of the particles (nanometer) and cells (micrometer). Additional results from the model for each light intensity can be seen in **Figure A.12** for each other variable (Ag^+, Ag^0, Ag^0_{bulk}, and Ag^0_{surf}) in the 3 chemical equations (**Equations 4.3-4.5**). The total silver ions in solution over the course of the synthesis for each light intensity follows a reversed s-shape curve where silver ion reduction starts off slow and rapidly increases in reduction rate until the ions are completely depleted (**Figure A.12A,C,E**). The opposite can be seen for Ag^0, Ag^0_{bulk}, and Ag^0_{surf} where they all follow an s-shape curve over time for each light intensity (**Figure A.12B,D,F**). It is important to note that the surface atoms take up a greater fraction of the total atoms in the AgNPs at earlier synthesis times when the NPs are smaller. The percentage of total surface atoms in the AgNPs significantly decreases as the synthesis continues due to the AgNPs rapidly growing in size.

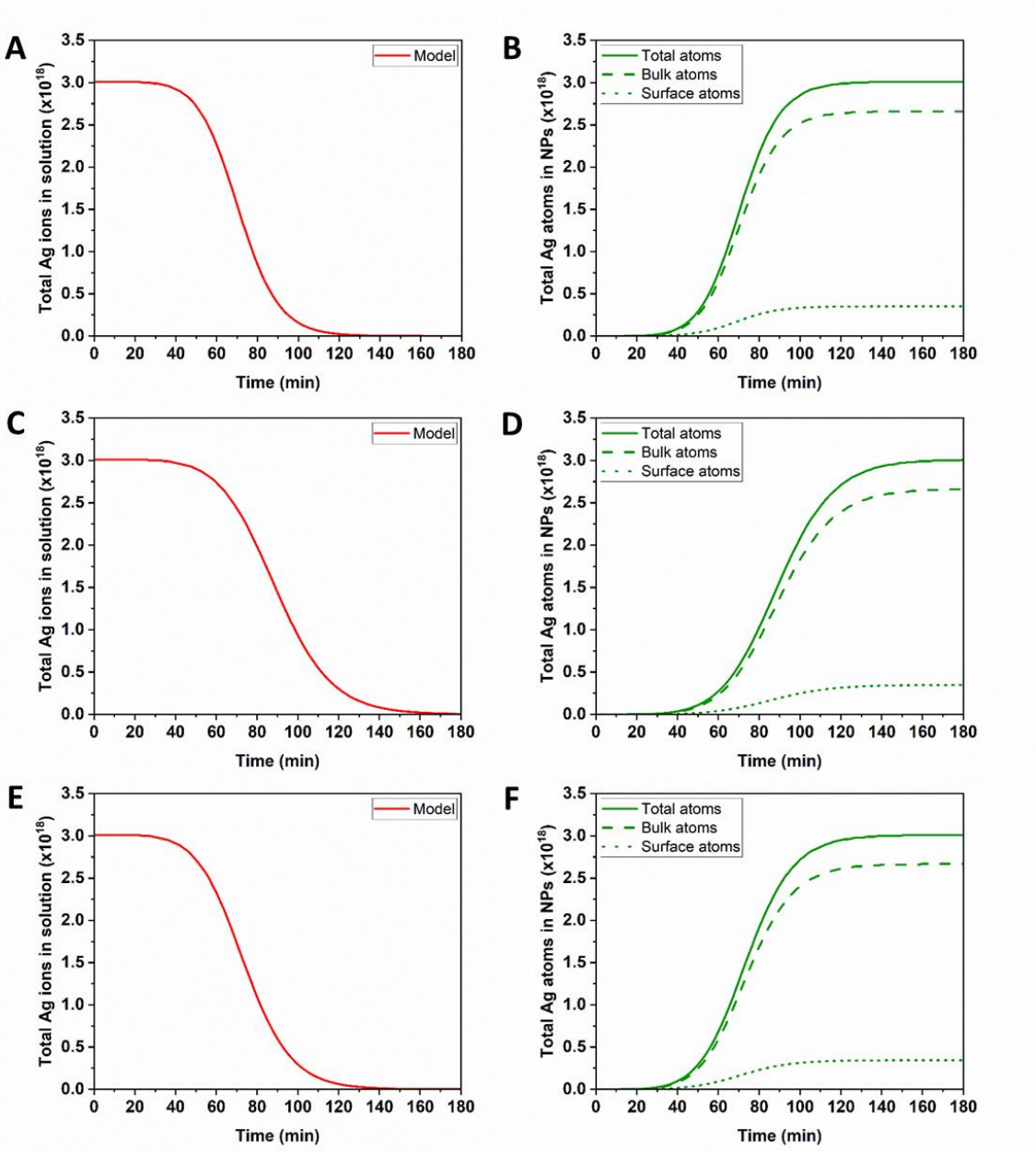

Figure A.12. Theoretical silver ion/atom changes over time from kinetic model. (A,B) Model calculations for synthesis at 1.3 mW/cm^2 light intensity for **(A)** total unreacted silver ions in solution and **(B)** total reacted silver atoms in all AgNPs (solid line) along with atoms encompassing the bulk (dashed line) and surface (dotted line) of the AgNPs **(C,D)** Model calculations for synthesis at 8 mW/cm^2 light intensity for **(C)** total unreacted silver ions in solution and **(D)** total reacted silver atoms in all AgNPs (solid line) along with atoms encompassing the bulk (dashed line) and surface (dotted line) of the AgNPs **(E,F)** Model calculations for synthesis at 17.2 mW/cm^2 light intensity for **(E)** total unreacted silver ions in solution and **(F)** total reacted silver atoms in all AgNPs (solid line) along with atoms encompassing the bulk (dashed line) and surface (dotted line) of the AgNPs.

Additional 8 mW/cm^2 light intensity results

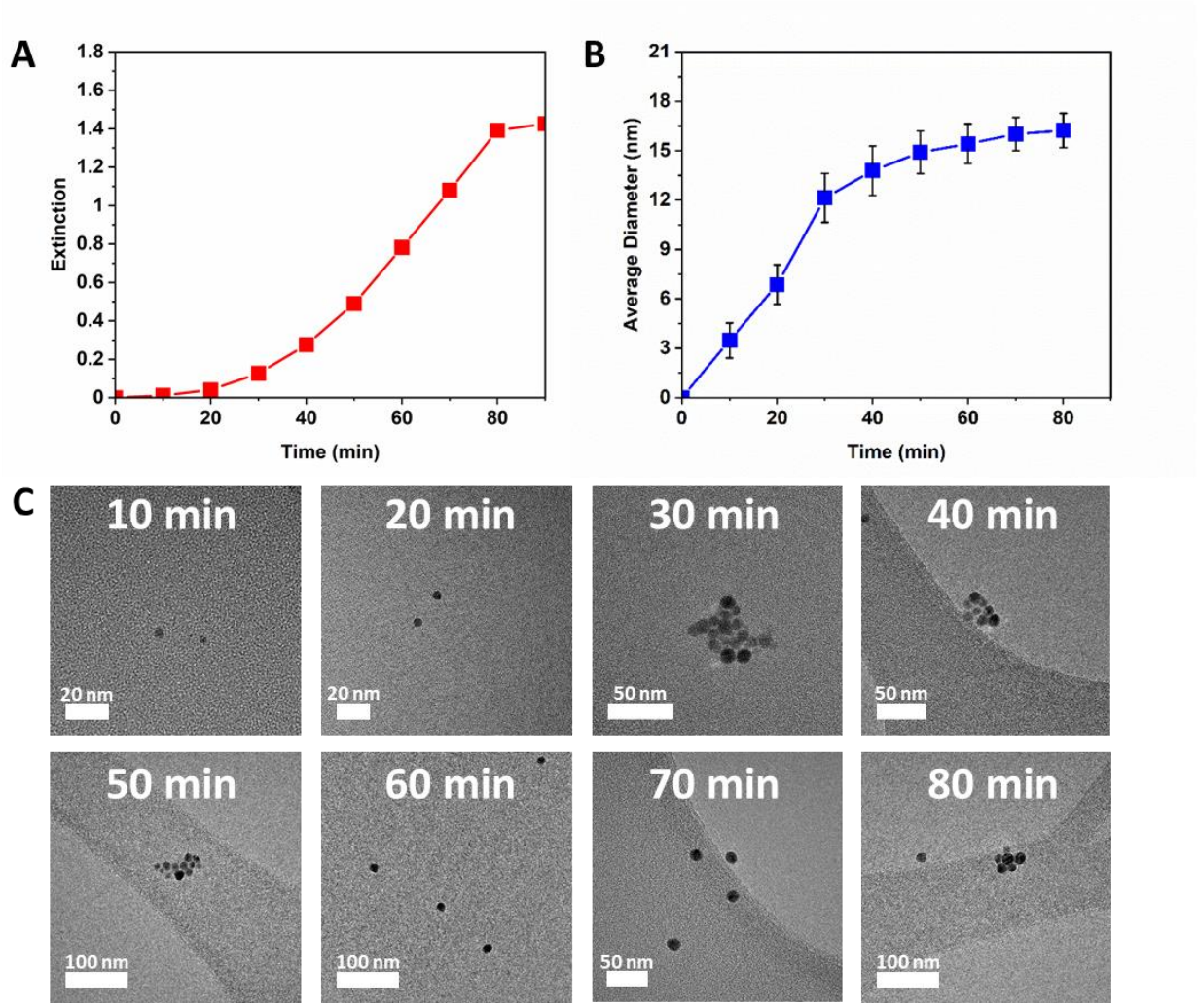

Figure A.13. Additional 8 mW/cm^2 light intensity results. (A) Extinction intensity over time at max wavelength from UV-Vis spectroscopy **(B)** Average diameter measured over 100 AgNPs at 10 min intervals **(C)** Sample TEM images of AgNPs at each time point.

Additional 8 mW/cm^2 light intensity results

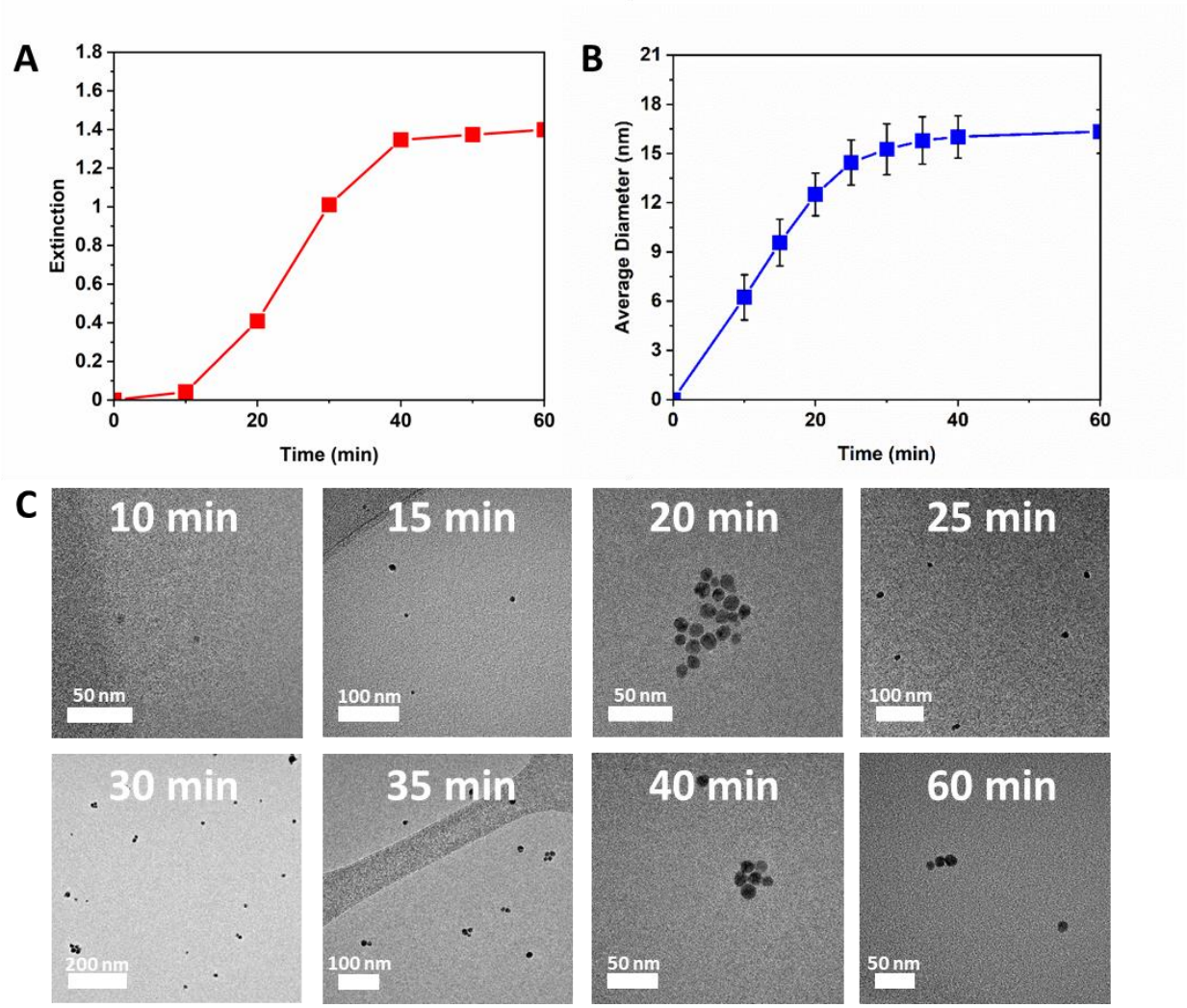

Figure A.14. Additional 17.2 mW/cm^2 light intensity results. (A) Extinction intensity over time at max wavelength from UV-Vis spectroscopy **(B)** Average diameter measured over 100 AgNPs at various time intervals up to 60 min **(C)** Sample TEM images of AgNPs at each time point.

Rate constnt vs Light Intensity

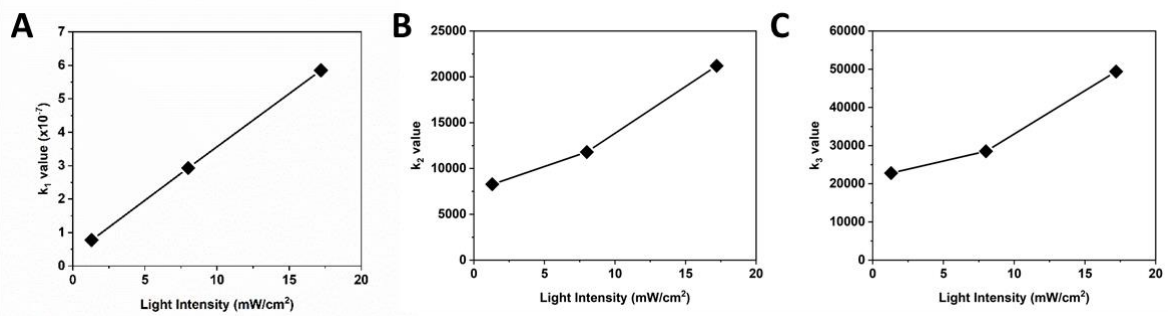

Figure A.15. Self-replicating model rate constants vs light intensity. (A) Rate constant k_1 **(B)** Rate constant k_2 **(C)** Rate constant k_3.

Extended Electroless Deposition

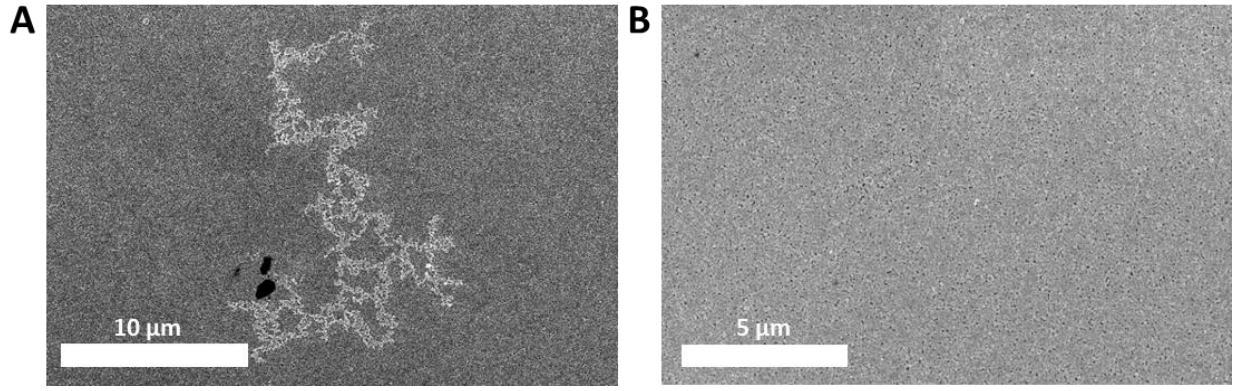

Figure A.16. Extended electroless silver deposition (A) SEM image of a 40 min electroless silver deposition on the AgNP networks supported on a PSS/PDDA functionalised glass slide. Lighter area is the self-replicating AgNP network and darker area is silver from the deposition. **(B)** SEM image of the growth of the 40 min electroless silver deposition roughly 50-100 µm away from the AgNP network.

Additional Hedgehog Particle Images

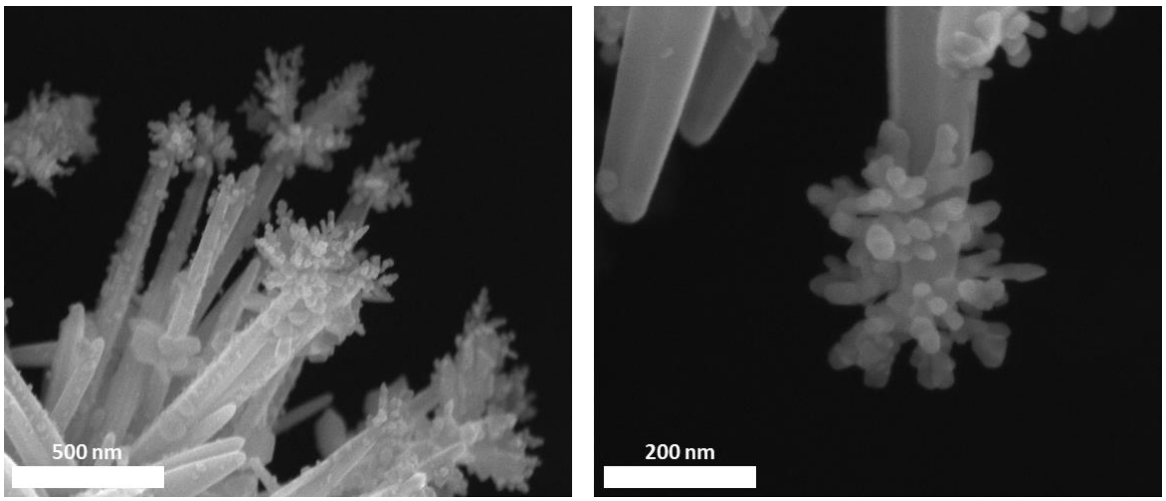

Figure A.17. Additional SEM images of self-replicating AgNPs on ZnO/Fe_2O_3 hedgehog particles

References

1. Horváth, A. K. Law of Mass Action Type Chemical Mechanisms for Modeling Autocatalysis and Hypercycles: Their Role in the Evolutionary Race. *ChemPhysChem* **2020**, *21* (15), 1703–1710.

2. Ershov, V.; Tarasova, N.; Ershov, B. Evolution of Electronic State and Properties of Silver Nanoparticles during Their Formation in Aqueous Solution. *Int J Mol Sci* **2021**, *22* (19).

3. Laomettachit, T.; Kraikivski, P.; Tyson, J. J. A Continuous-Time Stochastic Boolean Model Provides a Quantitative Description of the Budding Yeast Cell Cycle. *Scientific Reports 2022* **2022**, *12* (1), 1–12.

4. Olivares-Marin, I. K.; González-Hernández, J. C.; Regalado-Gonzalez, C.; Madrigal-Perez, L. A. Saccharomyces Cerevisiae Exponential Growth Kinetics in Batch Culture to Analyze Respiratory and Fermentative Metabolism. *J Vis Exp* **2018**, *2018* (139), 58192.

5. Ahmadian, M.; Tyson, J. J.; Peccoud, J.; Cao, Y. A Hybrid Stochastic Model of the Budding Yeast Cell Cycle. *npj Systems Biology and Applications* **2020**, *6* (1), 1–10.

Appendix B Direct Printing of Helical Metal Arrays by Circularly Polarized Light

This Appendix contains additional notes for **Chapter 5.4.1** from the publication currently in submission: Kim, JY.; McGlothin, C.; Cha, M.; Pfaffenberger, Z. J.; Turali-Emre, E.S.; Choi, W.; Biteen, J. S.; Kotov, N.A. "Direct Printing of Helical Metal Arrays by Circularly Polarized Light" *Nature Synthesis* (2023).

It should be noted that this model was developed by Dr. Ji-Young Kim and I do not take credit for the computational results from it. It is used with permission in this thesis from our paper for the sole purpose to help explain the experimental results that I contributed too.

Modeling Silver Helicoid Assemblies Via Finite Element Analysis Simulations

To understand the photon-induced growth mechanism of silver helicoid assemblies, adequate models representing 6 different growth stages of *L*-helicoids synthesized under the 532 nm laser were predicted by sequential electromagnetic simulations. Based on the electron microscopic observations (**Figure 5.3A**), geometric parameters of nanoparticles (NPs) in the dimer model were firstly determined. Hemisphere (diameter = 20 nm) on substrate were constructed on a substrate (refractive index = 1.52) while the flattened ellipsoid (short axis length = 10 nm) was attached in parallel with each other 20 nm apart (**Figure 5.3D**). The dimer 3D model was imported into COMSOL Multiphysics 5.5 software package (the radio frequency module) to calculate electromagnetic field under two different CPL exposures by solving the frequency domain form

of Maxwell's equations with finite element analysis (FEA). The substrate material was considered as glass with refractive index of 1.53. The maximum mesh size of finite element analysis is set to $\lambda/4n$, where λ is the wavelength of incident light and n is the real part of the material refractive index, and perfect matched layer is used to minimize the scattering from the outer boundary. The substrate surface was placed in the ***x*-*y***-plane while CPL is propagated along the z-axis with port power of 8.1×10^{-5} W. The periodic condition generates infinite substrate space before introducing the silver model structures.

The asymmetric growth on the initial dimer was predicted by asymmetric electric field formation as shown in **Figure 5.3E**. The volumetric plot with high electric field (above 6.0×10^{6} V/m) was collected as a STL. 3D file and set as a new 3D model with material of silver for the sequential modeling. The next generation of electric field shows even more intensified asymmetry in the electric field under CPL (**Figure 5.3F**) as the high electric field region moves in rotatory trajectory. The models with different growth stage were then built by tracking these high electric field areas. For example, the trimer model structure (**V1** in **Figure 5.3D**) was built by adding bigger NPs at corresponding high electric field region as shown in **Figure 5.3F** under *L*-CPL, matching this iterative process of particle growth observed in electron microscopy images.

Calculation of Circular Dichroism of Silver Helicoids by Electromagnetic Simulation

To examine underlying physics in chiroptical activities of the structure, the different nanostructure stages were constructed in the electromagnetic simulation. The evolution of the calculated difference in extinction cross section under *L*- and *R*-CPL were compared with the experimentally obtained CD spectra to check the polarity of the CD peaks and their spectral placement.

The chiroptical activities from important growth stages of helicoid (**V1-3** in **Figure 5.3D)**, predicted by sequential electromagnetic simulations as described in Supplementary Note 3, were evaluated through FEA computation. The model computes the scattering and absorption cross-sections under *L*- and *R*-CPL.

The total scattering cross-section (σ_{sc}) is defined as

$$\sigma_{sc} = \frac{I}{I_0} \iint (n \bullet S_{sc}) dS \tag{B.1}$$

Here, n is the normal vector pointing outwards from the local surface, S_{sc} is the scattered intensity (Poynting) vector, and I_0 is the incident intensity. The integral is taken over the closed surface of the meta-atom. The absorption cross section (σ_{abs}) is expressed as

$$\sigma_{abs} = \frac{I}{I_0} \iiint Q dV \tag{B.2}$$

where Q is the power loss density in the structure and the integral is taken over its volume.

The total extinction cross section (σ_{ext}) is simply the sum of the scattering and absorption:

$$\sigma_{ext} = \sigma_{sc} + \sigma_{abs}$$

$$\sigma_{ext} = \sigma_{sc} + \sigma_{abs} \tag{B.3}$$

The chiroptical response of the single meta-atom can be characterized as $\sigma_{ext,R-\mathrm{CPL}} - \sigma_{ext,L-\mathrm{CPL}}$. From the **V2** to **V3**, we could see emergence of additional chiroptical bands as star marked in **Figure 5.3G**.